Study of a Brominated Triphenylamine Derivative on Metal and Semiconducting Surfaces

By

Davide Marchese

A thesis submitted in partial fulfillment of the requirements
for the degree Master of Science

Department of Physics, Lakehead University

Abstract

Room-temperature STM experiments were conducted for tribromotrioxoazatriangulene, (TBTANGO), on three surfaces: Si(111)-$\sqrt{3}$x$\sqrt{3}$-R30^{o}-B, Ag(111), and Au(111) on mica. We found for the silicon samples there was a trade-off between attaining sufficient boron to passivate surface while remaining contamination free. STM imaging shows TBTANGO fragments were decomposed by surface dangling bonds. Of the procedures tested to prepare an atomically clean but passive surface, flashing near 1200^{o}C, followed by annealing for 100 minutes at 930^{o}C was the best.

The (111) face of silver was explored at room-temperature and elevated-temperature as a molecular substrate. Both instances showed that TBTANGO forms two-dimensional organometallic structures. At room-temperature, short oligomers were formed. With the silver crystal at 240^{o}C, large organometallic SAMNs were formed. The molecules formed a honeycomb organometallic network with trapped bromine atoms within many of the pores. The honeycomb cell of TBTANGO on hot silver is commensurate with the underlying substrate within error. The cell is $s_1 = 19.8$ Å, $s_2 = 19.8$ Å, $\theta = 60.3^{o}$. The pore-to-pore separation distance calculated by gas phase density functional theory was ~22.1 Å. The deposition of TBTANGO on hot silver also supported a close-packed phase believed to be an organometallic SA with 3 metal-carbon links.

Thin films of Au(111) terminated facets supported the self-assembly of TBTANGO at a substrate temperature of 180^{o}C. The unit cell was measured to be $s_1 = 10.5$ Å, $s_2 = 10.5$ Å, $\theta = 59.2^{o}$. Theoretical calculations for the self-assembled cell are $s_1 = 13.3$ Å, $s_2 = 13.3$ Å, $\theta = 60^{o}$. The discrepancy between the measured is attributed to STM drift.

There are known knowns; there are things we know we know. We also know there are known unknowns; that is to say we know there are some things we do not know. But there are also unknown unknowns – the ones we don't know we don't know.

...it is the latter category that tend to be the difficult ones

- Donald H. Rumsfeld

Table of Contents

1. Introduction

Two-dimensional materials with at least one dimension on the scale of nanometers are known as nanomaterials (Reithmaier et al., 2009). Nanomaterial research is active with possible applications across various industries. Areas of application include biotechnology (Naseri, 2015), semiconductors (Gutzler et al., 2012), lithography (Hughes, Menumerov & Neretina, 2017), medicine (Nie et al., 2007; Li et al., 2016) and even agriculture (Baruah & Dutta, 2007; Zhong et al., 2006). Some examples are the use of porphyrin molecules in optical sensors (Ishihara et al., 2014), iron oxide based nanostructures to filter various pollutants from water (Zhong et al., 2006) or composite nanomaterials for use in stabilizing high power electrochemical capacitors (Rajendran et al., 2015). Nanostructured materials are widely used in optoelectronics (Kamanina, 2010; Djurišić, Ng & Chen, 2010).

As research and engineering advance, nanomaterials are becoming more commonplace in everyday life. Nanostructured materials show unique properties as a consequence of their high surface area to volume ratio, nanoscale confinement and quantum effects (Reithmaier et al., 2009). Previously unrealized possibilities will continue to arise and lead to new applications in electronics, biotechnology and medicine just to name a few.

The two general approaches to synthesizing nanomaterials are the so-called "top-down" and "bottom-up" techniques. The top-down approach starts with a sample of large dimensions and involves the precise removal of unwanted material. It requires sophisticated techniques such as electron-beam writing or extreme ultraviolet lithography (Barth, Costantini, & Kern, 2010). Conversely, in the bottom-up approach, Nature guides the assembly of atomic and/or molecular constituents into organized nanostructures (Barth, Costantini, & Kern, 2010). Self-assembly (SA) is a commonly used conduit for bottom-up fabrication where

molecular constituents spontaneously assimilate to a nanostructure or molecular network (Whitesides, Mathias & Seto, 1991; Philp & Stoddart, 1996).

One area of research where the application of nanostructured materials is already being tested is in electronics. Two-dimensional structures have shown promise in modulating electric and charge carrying properties of different materials (Dmitriev et al., 2003). Nanostructures have gained much attention when combined with metal or semiconducting surfaces (Bartels, 2010; El Garah et al., 2013). On-surface non-covalent structures may be used as active layers in organic-inorganic electronic devices (Green et al., 2007; Barth, Costantini, & Kern, 2010). In addition, beyond non-covalent SA structures, covalently bonded 2-D polymers, (2DPs), offer impressive charge carrier mobility with robust physical and chemical characteristics (Perepichka & Rosei, 2009). Two dimensional polymers may lead to future improvements in silicon-based switching devices (Gutzler et al, 2012).

We chose to study the tribromotrioxoazatriangulene molecule, (TBTANGO), and the formation of 2-D nanostructures on several surfaces. TBTANGO is a triphenylamine derivative. Triphenylamine is a well-known hole-transport molecule used in optoelectronic devices (Agarwala & Kabra, 2017). This suggests TBTANGO is a strong candidate to form nanostructures in future molecular electronics or as 2DPs (Galeotti et al., 2020). The specific surfaces we chose to investigate are Ag(111), Au(111) and Si-$\sqrt{3}$x$\sqrt{3}$-R30°-B. The study utilized several surface analytical techniques including scanning tunnelling microscopy (STM), Auger electron spectroscopy (AES) and low energy electron diffraction (LEED). The goal of the study was to investigate the nature of the nanostructures formed on the different surfaces.

The remainder of the thesis is organized as follows: Chapter 2 reviews the literature concerning molecular deposition and self-assembly. Examples of various self-assembled

systems are given. The mediating forces of these systems – van der Waals, hydrogen bonding and halogen-halogen interactions are compared. Halogen-halogen interactions are of particular interest to this work so are covered in additional detail. The effect of the substrate on self-assembly is also reviewed.

Chapter 3 reviews the theory necessary for understanding the remainder of the document. The necessary notations, Miller indices and Wood's notation, are reviewed. The crystal structure of the three substrates used in this thesis – boron doped silicon, silver, and gold crystals are covered. Both gold and the silicon-boron substrates undergo surface reconstructions which are detailed. The *a priori* engineering choices of TBTANGO and the nature of the mica substrate are briefly discussed. The theory of the on-surface Ullmann reaction is partially covered as it is relevant to our experimental result.

Equipment and experimental methods are discussed in Chapter 4. In the first part of this chapter, the operational principle of all pumps and procedures needed to reach ultra-high vacuum are explained. In the subsequent section, other ultra-high vacuum equipment such as the residual gas analyzer, the molecular evaporator, ion sputter gun and pyrometer are acknowledged. The second part of Chapter 4 covers the major surface science techniques used to evaluate the sample surface such as low-energy electron diffraction (LEED), Auger electron spectroscopy (AES) and scanning tunnelling microscopy (STM). The principle of operation for these techniques are given in depth. Sample data for our surface analytical techniques is provided to facilitate the reader's interpretation of the data. Chapter 4 closes with the computational details of the density-functional theory calculations performed in this thesis.

Results can be found in Chapter 5. This chapter is broadly categorized by each surface studied with each broad category being further organized as follows: i) the specific parameters

for the preparation of the surface, ii) the outcome, iii) the result of the molecular deposition. Self-assembly is supported on the gold and silver surfaces. The silicon-boron surface did not support self-assembly as it could not be prepared to a sufficient quality. Chapter 6 summaries the thesis. A brief summary of the thesis is given and questions for the future are proposed.

2. Background

This chapter gives a brief review of key or pioneering studies which help to frame our experiments in the context of the literature. The general effects of deposition are first covered before self-assembly is explored. The self-assembly sub-chapter is further divided by the types of intermolecular forces which mediate self-assembled structures on surfaces. One of these mechanisms, halogen-halogen interactions is given additional consideration as it is especially important to this work. The chapter closes with the effects of the substrate on the molecular overlayer.

2.1 General Deposition Kinetics & Thermodynamics

Diffusion is a measure of how far an absorbed species will travel in a given period of time (Barth, Costantini & Kern, 2010). Diffusion can occur through various means such as edge diffusion, surface diffusion and interlayer diffusion. Each type of diffusion is associated with its own energy barrier. According to Tan & Zhang, (2019), the energy required for the various types of diffusion to occur increases in the order: edge $<$ surface $<$ interlayer. Moreover, step edges typically are favourable adsorption sites compared to the substrate surface (Tan & Zhang, 2019). When molecular units are deposited on a surface, they either diffuse on the surface or are bound in place. Mobile entities have the possibility to merge with other adsorbates or surface structures to form an aggregate structure. This process is named nucleation (Tan & Zhang, 2019).

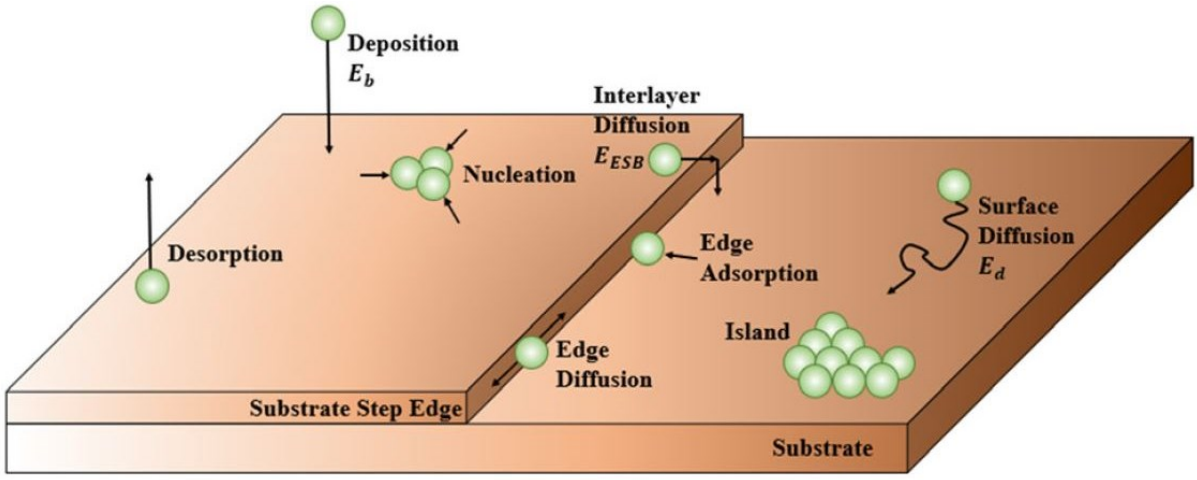

Fig 2.1: The basic processes of organic molecular assembly on a substrate surface are schematically illustrated. Desorption, depositon, and the various types of diffusion are shown. (Tan & Zhang, 2019)[1]

The structure that ensues from molecular deposition is dependent on the surface diffusivity of the adsorbed species and the deposition rate. A high mobility and low deposition rate favours a thermodynamically stable state, whereas a higher deposition rate and low mobility leads to a kinetically limited state (Barth, Costantini & Kern, 2010; Gutzler, Cardenas, & Rosei, 2011). In order to achieve SA structures with the highest degree of order and lowest defect density, an approach with a low deposition rate and high mobility is preferred.

A high diffusivity occurs for molecules that weakly interact with the substrate while a low deposition rate allows for weakly bonded molecules to traverse the surface and properly orient themselves before merging with growing aggregates. Therefore, each molecule has enough time to settle in an energetic minimum. The structure that is formed is a thermodynamic global minimum. In the opposite scenario, a high deposition rate and low diffusivity, favours kinetically limited metastable states (Barth, Costantini & Kern, 2010;

[1] Republished with permission of IOP Publishing Ltd, from Tailoring the growth and electronic structures of organic molecular thin films, Journal of Physics: Condensed Matter, 31(50), 503001, copyright 2019, permission conveyed through Copyright Clearance Center, Inc

Gutzler, Cardenas, & Rosei, 2011). Two major parameters affecting the mobility of adsorbates on surfaces is the substrate identity and temperature (Weckesser, Barth & Kern, 1999).

Several reviews of research covering these deposition phenomena are available (Gutzler, Cardenas, & Rosei, 2011; Barth, 2007; Kühnle, 2009). One particular example of kinetic versus thermodynamic states was described by Marie et al. (2010). The molecule hexakis(*n*-dodecyl)-peri-hexabenzocoronene (HBC-C_{12}) self-assembles at room temperature on highly ordered pyrolytic graphite from n-tetradecane solution. The observed phase is kinetically limited as this phase spontaneously converts to the first of the annealed phases after about one hour at room temperature (Marie et al., 2010). No other phases are accessible at room temperature and must be annealed to be achieved.

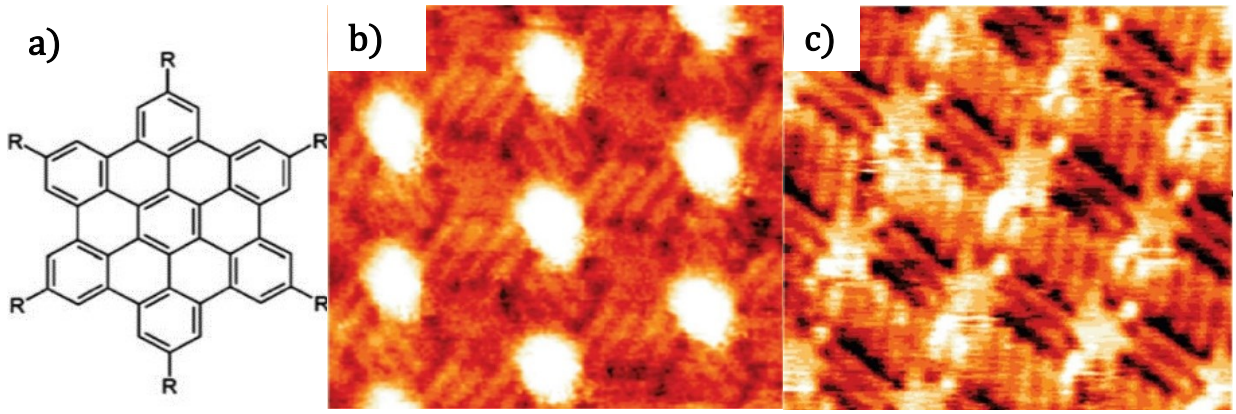

Fig. 2.2: a) The chemical structure of hexakis(*n*-dodecyl)-peri-hexabenzocoronene. b) and c) STM topographs showing tetradecane can be seen co-absorbed between HBC-C_{12} molecules. b) STM image of the meta-stable room temperature SA phase. (U_{bias} = -0.20 V, $I_{tunnelling}$ = 20 pA; 10nm x 9 nm) c) STM image of the phase in b) after an extended time at room tempearature (U_{bias} = -0.27 V, $I_{tunnelling}$ = 50 pA; 10nm x 9 nm) (Marie et al., 2010)[2]

A simple example of how the self assembled state can be influenced by temperature (and deposition rate) is given by Röder et al. (1993). Röder deposited silver atoms onto the Pt(111) surface and found the size and shape of the SA nanostructure can be controlled at the

[2] Reprinted with permission from Tuning the Packing Density of 2D Supramolecular Self-Assemblies at the Solid−Liquid Interface Using Variable Temperature, Camille Marie et al., ACS Nano. Copyright 2010 American Chemical Society.

atomic level by means of temperature. In figure 2.3, all surfaces had 1.2% of a silver monolayer deposited on the Pt(111) surface. Holding the substrate at 40 K gives rise to homogenously distributed silver dimers. A substrate temperature of 110 K as in figure 2.3 b) leads to silver clusters with an average of 6 atoms per aggregate. However, in figure 2.3 c), (150 K) each cluster contained an average of 26 atoms.

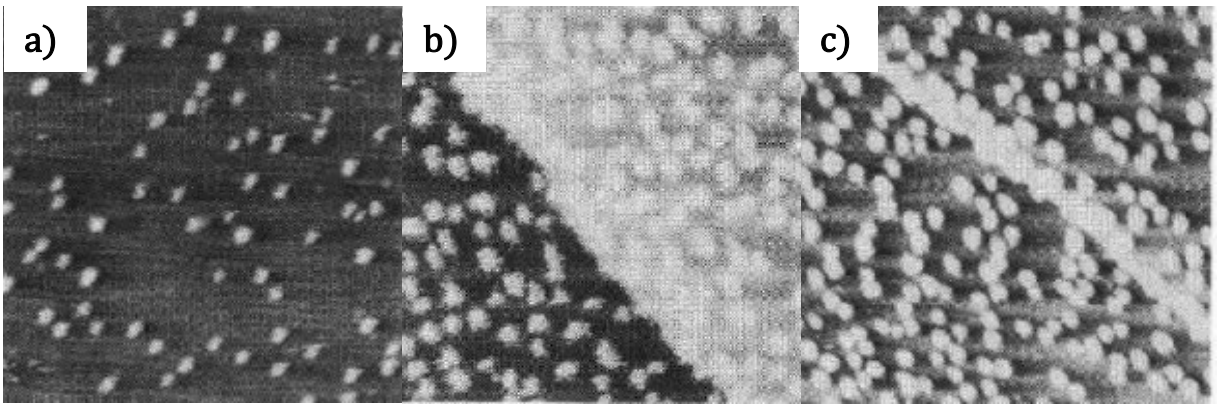

Fig. 2.3: STM topographs of silver deposited on the Pt(111) surface at three temperatures, a) -233°C gives rise to dimers while b) -163°C and c) -123°C lead to aggregates with 6 or 26 atoms on average respectively. a) (300 Å x 300 Å); b) (215 Å x 215 Å); c) (530 Å x 530 Å). (Röder et al., 1993)[3]

2.2 Self-Assembly

Self-assembly (SA) or self-assembled molecular networks (SAMNs) may be an avenue to affordably and repeatably mass-manufacture 2-D nanostructures. As mentioned before, SA is a powerful bottom-up technique. A bottom-up approach can be compared to 3-D printing an object with a desired geometry, whereas a top down approach is comparable to chiseling the object from a block. Because of the bottom-up nature of self assembly, it can leverage the influential and catalytic properties of substrates to rapidly produce SA nanostructures or SAMNs in 1-D or 2-D with tunable electrical properties (Gutzler, Cardenas & Rosei, 2011).

[3] Reprinted by permission from Copyright Clearance Center: **Springer Nature**, **NATURE**, (Building one- and two-dimensional nanostructures by diffusion-controlled aggregation at surfaces, Röder, 1993), © **1993**

Self-assembly on surfaces refers to the organization of molecules into large stable complexes held together by weak non-covalent interactions (Whitesides, Mathias & Seto, 1991). Examples of non-covalent interactions include van der Waals (Gao et al., 2015), hydrogen bonding (MacLeod et al., 2009) or halogen-halogen bonds (Gutzler et al., 2011) to reach the self-assembled state. The SA process happens without outside intervention to a stable or meta-stable state.

Self-assembly is a reversible process. Reversible processes by their nature can eliminate or correct unfavourable bonds or defects and result in highly periodic structures with long range order. The repair or elimination of defects in supramolecular structures is known as "self-healing". The relatively weak non-covalent bonds between monomers allow SAMNs the possibility of self-healing (Di Giovannantonio, & Contini, 2018). The possibility to self-heal is one of the main advantages of SA. The caveat of reversible, non-covalently bonded structures is that they are fragile – chemically, physically, and thermally. However, this does not necessarily preclude SAMNs or nanostructures as active media in organic electronic devices (Di Giovannantonio, & Contini, 2018).

The structural and chemical properties of the precursor molecules determines the chemical and physical characteristics of the resultant supramolecular structure. Information on the specifics of our precursor molecule can be found in Chapter 3.7. Precursor molecules can be thought of as small dots of "ink" in the proverbial 3-D printed object. Compared to top-down approaches, bottom-up techniques (including SA) are direct fabrication processes which leverage Nature. Self-assembly on surfaces has been and continues to be investigated with various precursors and substrates – see the work by Pham et al., (2014); Menzli et al., (2016); Liu et al., (2016) or Zhang et al., (2020).

2.2.1 van der Waals Stabilized Self-Assembly

Van der Waals interactions are weak non-local, non-covalent dipole interactions. Originally, van der Waals interactions encompassed electrostatic (permanent moment-permanent moment), induction (permanent moment-induced moment), and dispersion (induced moment-induced moment) interactions (Hermann, DiStasio & Tkatchenko 2017). These three types of dipoles are often referred to as non-covalent interactions, while the term van der Waals interactions is reserved specifically for induced-induced dipole interactions (Hermann, DiStasio & Tkatchenko 2017). This work refers to any such combination of dipoles as van der Waals interactions.

Van der Waals interactions can range from a fraction of to a few kcal/mol in magnitude, making them the weakest known bonding types (Barth, 2007). For example, Ne atoms have an interaction strength of 0.7 kcal/mol, whereas Xe atoms experience 2.2 kcal/mol of interaction energy (Ondrechen, Berkovitch-Yellin & Jortner, 1981).

Several groups have demonstrated the on-surface SA of organic molecules. For example, 1,3,5-triethynylbenzene, 1,3,5-triethynyl-2,4,6-trimethylbenzene and 1,3,5-tributyl-2,4,6-triethynylbenzene (molecules with akyl side chains of length 0, 1 or 4) where shown to form ordered SAMNs on Ag(111) and Au(111) (Gao et al., 2015). The smallest of the molecules was mobile enough that the authors were able to observe the molecule diffusing on the Ag(111) surface at 78 K while imaging with STM. Gao et al. (2015) found that modest annealing to temperatures between 90^{o}C (molecule 1) to 137^{o}C (molecule 3) was enough to disrupt the intermolecular forces and trigger a phase transition. Van der Waals forces are relatively weak in comparison to hydrogen or even halogen bonding (Gao et al., 2015).

Yokoyama et al. (2001a; 2001b) observed the nonplanar macrocyclic conformation of

porphyrin based molecules on the Au(111) surface. They used 5,10,15,20-tetrakis-(3,5-*di-tertiary*-butylphenyl) porphyrin (H_2-TBPP) for the study. H_2-TBPP consists of a free-base porphyrin core and four *di-tertiary*-butyl phenyl substituents. Yokoyama et al. (2001a; 2001b) found the van der Waals stabilized structures have controllable planarity and surface structure by changing the porphyrin substituents. This was demonstrated by the inclusion or exclusion of nitrile groups. Density functional theory calculations support the authors' observations of van der Waals stabilized SA structures.

2.2.2 Hydrogen Bond Stabilized Self-Assembly

Van der Waals interactions can compete to stabilize SAMNs with other intermolecular forces. Liao et al., (2014) were able to show that different stilbene molecules substituted with ester groups formed various surface structures by modifying the length of the alkoxy chain. By removing 6 carbon atoms from the alkoxy chain, the SA structure switches to a Kagomé

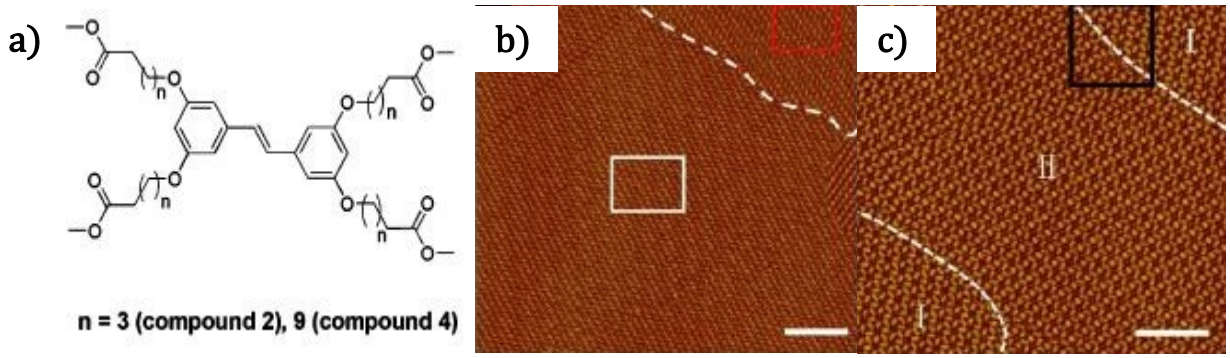

Fig. 2.4: a) The stilbene derivatives with varied side chain length; labelled compounds 2 or 4. b) The linear striped network forms when van der Waals interactions dominate. (U_{bias} = 0.62V, I = 290pA) c) The Kagomé structure results when the side chain is shortened and hydrogen bonding dominates. (U_{bias} = 0.59V, I = 290pA) (Liao et al., 2014)[4]

network from a linearly striped structure. The authors attribute the change in phase to a

[4] Reprinted with permission from Two-Dimensional Supramolecular Self-Assembly of Stilbene Derivatives with Ester Groups: Molecular Symmetry and Alkoxy Substitution Effect, Ling-yan Liao et al., The Journal of Physical Chemistry C. Copyright 2014 American Chemical Society.

change in regimes - either dominated by van der Waals or hydrogen bonding forces.

Hydrogen bonds are a non-covalent, attractive interaction between a proton donor, R–H, and a proton acceptor, Ac, in the same, or in a different molecule, i.e. $R—H \cdots Ac$. According to the conventional definition, the hydrogen atom is bonded to electronegative atoms such as nitrogen, oxygen or fluorine. The proton acceptor, Ac, is either an electronegative region or a region of electron excess, such as an atom or molecular fragment (Parthasarathi & Subramanian, 2006). Typical examples of the proton acceptor include O-H, O=C, N-R functional groups.

Hydrogen bonds are stronger than van der Waals interactions. Conventional hydrogen bonds are regarded as being in the range from 4 kcal/mol – 15 kcal/mol. Any hydrogen bonds below or above this range are considered weak or strong hydrogen bonds respectively (Parthasarathi & Subramanian, 2006). Hydrogen bonds have some directionality, but deviations up to $\pm 20^{o}$ from linearity show an insignificant effect on the hydrogen bond strength (Parthasarathi & Subramanian, 2006).

Theobald et al., (2003) were one of the first groups to demonstrate a SAMN held together by hydrogen bonds. They found an open honeycomb network formed when perylene tetra-carboxylic di-imide (PTCDI) is co-adsorbed with melamine (1,3,5-triazine-2,4,6-triamine) on Si(111)-$\sqrt{3} \times \sqrt{3}$-R30^{o}-Ag. In addition, hydrogen bonding has been shown to mediate SA by other groups (De Feyter et al., 2005). MacLeod et al. (2009) found that terthienobenzenetricarboxylic acid (TTBTA) self-assembles at the octanoic acid/graphite interface into either a close-packed hexamer motif or a porous network linked by hydrogen bonding associations.

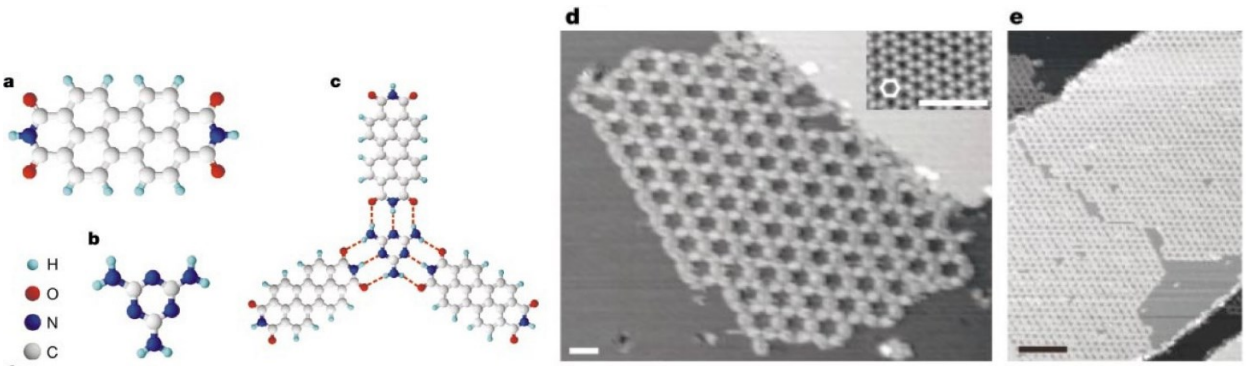

Fig. 2.5: (a) The PTCDI molecule and (b) melamine interact in (c) where the hydrogen bonds are highlighted in dashed red lines. STM images of the honeycomb network can be seen in (d) and (e). The scale bars are 3nm and 20nm respectively. Both images are taken at -2V and 0.1nA. (Theobald et al., 2003)[5]

2.2.3 Halogen-Halogen Interaction Stabilized Self-Assembly

Self-assembly can also be supported by halogen-halogen interactions. Similar to hydrogen bonds, halogen-halogen interactions refer to highly directional interactions between a charge donor, R–X, and a charge acceptor, Ac, where X is any halogen and Ac is an electronegative atom. Interestingly, halogens are sufficiently polarizable such that they can act as both charge acceptors and charge donors (Politzer, Murray & Clark, 2010). That is to say, the general bonding scheme for halogen interactions is $R{-}X \cdots Ac$, but halogen-halogen interactions specifically, are represented by $R{-}X \cdots X{-}R'$. In halogen-halogen interactions, the halogens are commonly chlorine, bromine or iodine with interaction energies of a few kcal/mol (Metrangolo, 2011). The energy of halogen interactions has been shown as high as 12 kcal/mol in the case of 3,5-difluorobromobenzene (Metrangolo, 2011).

Halogen-halogen stabilized SAMNs have been demonstrated on metal surfaces (Pham et al., 2014; Walch et al., 2010; Chung et al., 2011; Gatti et al., 2014) and passivated

[5] Reprinted by permission from Copyright Clearance Center: **Springer Nature**, **NATURE**, (Controlling molecular deposition and layer structure with supramolecular surface assemblies, Theobald et al, 2003), © **2003**

semiconducting substrates (Gutzler et al., 2011; Makoudi et al., 2014; Liu et al., 2016). For example, Chung et al. (2011) studied a rod-like molecule, 4,4”-dibromo-*p*-terphenyl, (DBTP) with brominated ends on Ag(111) using DFT and low-temperature STM. The low temperature of the substrate is a subtle point with large implications: halogenated molecules are susceptible to forming metal atom coordinated structures on certain metal substrates at and above room temperature. This is discussed further in Chapter 3.8. Chung et al. (2011) found three different SA structures were formed; stabilized by a triangular motif consisting of a halogen-halogen and halogen-hydrogen bonds. Square, rectangular and hexagonal network were formed on the silver surface.

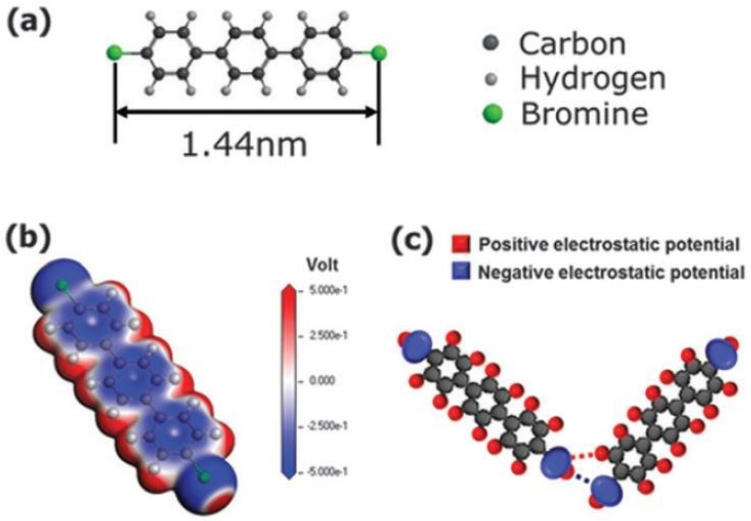

Fig. 2.6: a) The DBTP molecule forms three SAMNs on Ag(111). b) An electrostatic potential map of DBTP. c) Two DBTP molecules with the triangular bonding motif highlighted with dashed lines. (Chung et al., 2011)[6]

[6] Reproduced from Ref. (Chung et al., 2016) with permission from The Royal Society of Chemistry.

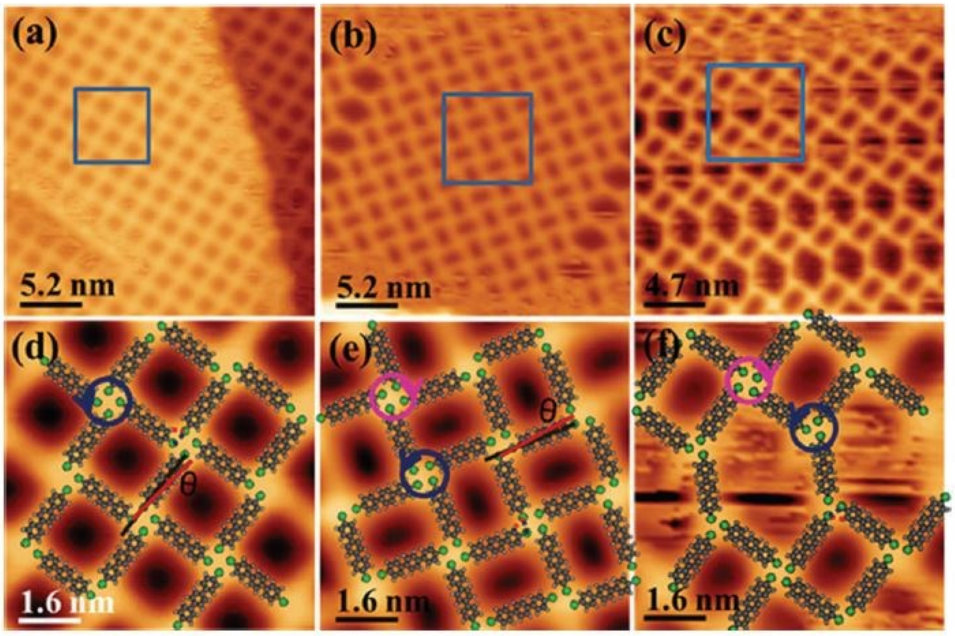

Fig. 2.7: a) – b) STM images of the square and rectangular DBTP SAMN phases. Both images are are 26nm x 26nm. c) STM image of the hexagonal network. 23.5nm x 23.5nm d) – f) 8nm x 8nm STM images with DBTP molecules overlaid. Bromine atoms are circled. All images are taken at $U_{bias} = 1V$, $I_{tunnelling} = 0.1nA$ (Chung et al., 2011)[6]

Likewise, 1,3,5-tris(4-bromophenyl)benzene (TBB) forms halogen stabilized SAMNs on silver and copper (Walch et al., 2010). Their study found silver supported the SA of halogen-halogen mediated structures at low- and room- temperature whereas copper only formed such structures at low temperature. Molecules deposited on copper at room temperature formed an organometallic structure (see figure 2.8). An organometallic is any compound containing at least one chemical bond between a carbon atom and a metal, including alkaline, alkaline earth, and transition metals (Crabtree, 2009). In a surface science context, an organometallic structure is a 2-D planar structure that consists of organic monomers linked to one another via metal adatoms of the substrate.

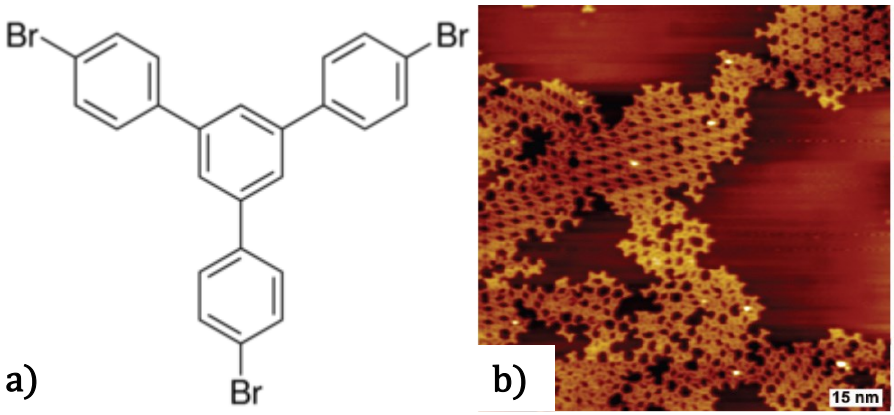

Fig. 2.8: a) TBB molecule. b) STM image of different self-assembled TBB phases on Ag(111). Molecules were deposited at room temperature. Right image presents two coexisting ordered phases, namely, a row structure on the upper center part and a hexagonal flower structure in the upper right part. The lower half depicts a disordered phase. (U_{bias} = -1.11 V, $I_{tunnelling}$ = 102 pA) (Walch et al., 2010)[7]

2.3 Advantages of Halogen-Halogen Interactions Over Other Non-Covalent Forces

Halogen reactive sites provide unique possibilities to construct a new class of functional supramolecular structures (Priimagi, et al., 2013). Unlike hydrogen atoms involved in hydrogen bonding, halogen atoms are hydrophobic. This could open the door to unforeseen possibilities in the pharmaceutical field since lipophilicity is a key parameter for drug delivery across biological barriers (Priimagi, et al., 2013). In addition, halogen atoms are large in comparison to the organic atoms. Steric hinderance could inhibit unfavourable reaction pathways.

The two main advantages of halogen-halogen interactions over other non-covalent interactions for creating SA nanostructures is their tunability and high directionality. In a

[7] Reprinted with permission from Material-and orientation-dependent reactivity for heterogeneously catalyzed carbon—bromine bond homolysis, Hermann Walch et al., The Journal of Physical Chemistry C., Copyright 2010 American Chemical Society.

halogen bond, the induced dipole is confined narrowly to the elongation axis of the R–X covalent bond (Priimagi, et al., 2013). This directionality dictates that (R–X ⋯ R') intermolecular interactions are very close to 180°. Halogen-halogen interactions are considered tunable because of the increasing bond strength of the Group 17 elements. Bond strength increases in the order I < Br < Cl (Metrangolo, 2011). Consequently, single atom changes within molecular building blocks can select for various dissociation temperatures without having to manipulate the remainder of the molecule. This allows researchers to adjust the temperature at which a 2-D polymer or organometallic phase forms without altering the organic backbone.

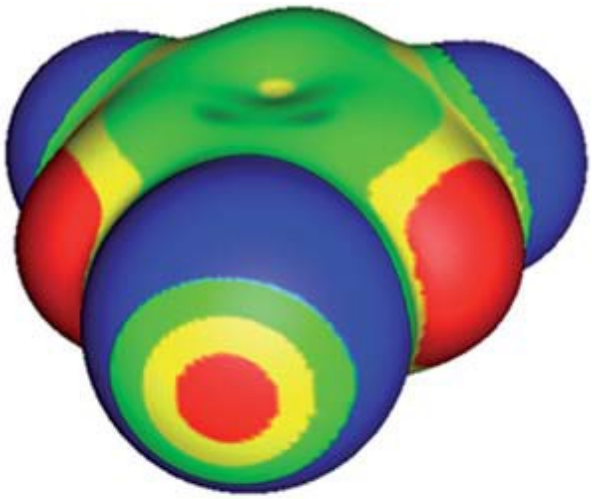

Fig. 2.9: Computed electrostatic potential of 3,5-difluorobromobenzene. A bromine is in the foreground with two fluorine atoms in the back left and right. The bromine atom has a positive region on its outer surface, along the extension of the C–Br bond, with the characteristic negative belt around its lateral sides. The fluorine atoms have completely negative potentials on their surfaces. (Metrangolo et al., 2011)[8]

As a consequence of the interchangeability of terminal halogen atoms, SAMNs mediated by halogen-halogen interaction can be chemically activated in a hierarchical fashion to form

[8] Reproduced from Ref. (Metrangolo et al., 2011) with permission from The Royal Society of Chemistry.

other nanostructures such as surface-confined metal-organic networks (SMONs) or 2-D polymers. For example, Lafferentz et al. (2012) were able to demonstrate growth of 1-D chains followed by the subsequent bonding of these chains into a 2-D network under UHV on Au(111). Lafferentz et al. (2012) used a porphyrin molecule with four phenyl legs as a central building block but with two *trans* bromine and two *trans* iodine atoms. First, thermally activated dissociation of the iodine sites (120°C) created linear growth in one direction. Subsequent activation of the bromine sites at temperatures >200°C combined the linear chains into a 2-D network. This stepwise approach (Lafferentz et al., 2012) was found to create a 2-D network with less defects than when the same molecule base was used in a one-step approach (Grill et al., 2007;) and has since been adapted by others creating SMONs (Lin et al., 2013).

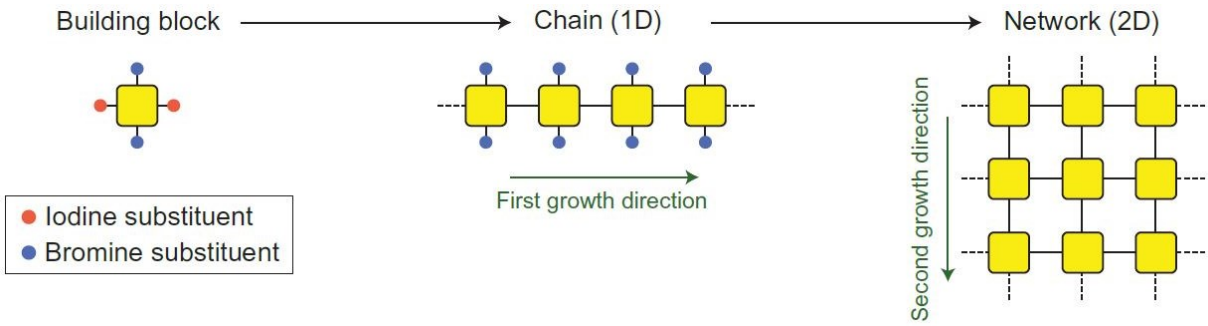

Fig. 2.10: The number of binding sites determines the dimensionality of surface confined growth. Growth can be forced to happen stepwise by using various halogen ends. First, linear chains are formed, and second, the chains amalgamate to create a 2-D network. (Lafferentz et al., 2012)[9]

2.4 Effects of the Substrate

Consideration of the substrate is an important parameter in self-assembly and other surface-confined experiments. The elemental composition of the substrate can affect

[9] Reprinted by permission from Copyright Clearance Center: **Springer Nature**, **NATURE CHEMISTRY**, (Controlling on-surface polymerization by hierarchical and substrate-directed growth, Laffrentz et al, 2012), © **2012**

adsorbates' diffusivity on the surface, thereby directing a reaction towards the thermodynamic or kinetically favoured state. For example, gold and silver allow for a given adsorbed species to diffuse faster than on a copper surface (Galeotti et al., 2019). This was significant enough for Galeotti et al., (2019) to observe tridentate tribromoterthienobenzene (TBTTB) form ordered hexagonal structures on Au(111) and Ag(111) but disordered chain structures on Cu(111) at room temperature.

Furthermore, the hexagonal structure on Au(111) was a SAMN whereas on Ag(111), the structure was organometallic. This illustrates the potential catalytic properties of substrates. Although both gold and silver have identical fcc bulk crystal structures, only silver provided the activation energy necessary to initiate the transition to the organometallic phase.

The crystallographic plane of the substrate is another significant parameter to consider. Walch et al., (2010) found that 1,3,5-tris(4-bromophenyl)benzene (TBB) was able to form a SAMN on Ag(111) at low temperature. However, on Ag(110), only a disordered arrangement of single molecules was achieved. The authors attributed this difference to the suppressed lateral mobility of TBB on the (110) face (Walch et al., 2010). Walch et al., (2010) also deposited TBB on Ag(110) and Ag(111) at room temperature. While large ordered dehalogenated organometallic structures were observed on Ag(110), TBB precursors did not dehalogenate at room temperature on Ag(111). Therefore, in addition to substrate identity, substrate morphology can affect on-surface reactions.

The importance of the substrate is not limited to metals. In fact, semiconductor substrates are often more reactive than metal substrates. A classic example is that of Suzuki et al., (2009), who compared the adsorption of terephthalic acid (TPA) on pristine Si(111)–7x7, passivated Si(111)–$\sqrt{3}$x$\sqrt{3}$–Ag and clean Ag(111) substrates.

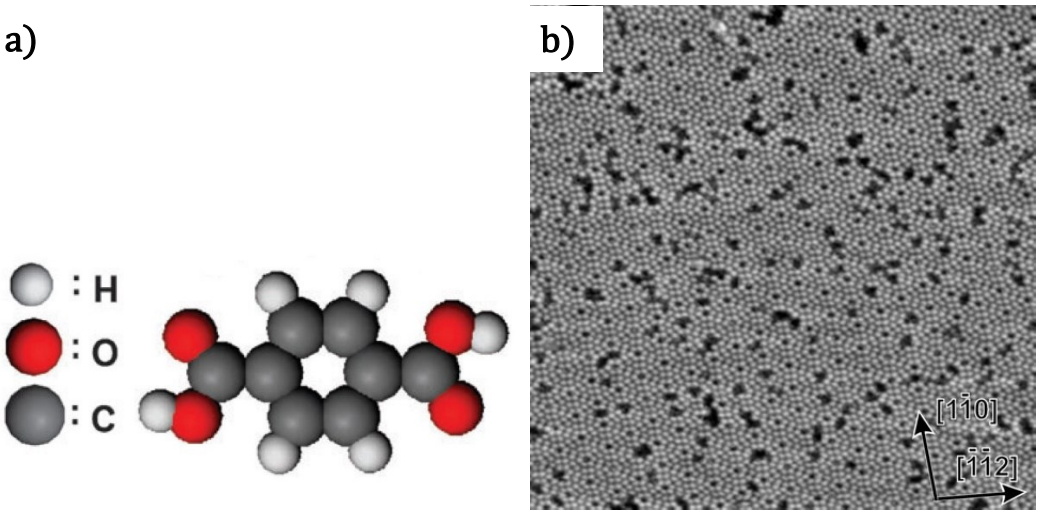

Fig. 2.11: a) The TPA molecule used by Suzuki et al. (2009). b): STM image of TPA deposited on the Si(111)-7x7 surface. The molecules are shown in black and can be seen randomly scattered. ($U_{bias} = +1.9$ V, $I_{tunnelling} = 350$ pA; 50nm x 50nm) (Suzuki et al., 2009)[10]

The bare silicon substrate reacts with the molecules and forms covalent bonds. As a result, TPA molecules are bound to the surface wherever they land upon deposition. Simply put, the TPA molecules "hit-and-stick" to the surface. The high reactivity of semiconductor substrates, such as the pure silicon in this example, prevents SA. This is because the diffusivity of adsorbed species is effectively zero and bare semiconductor surfaces have the capability to break the molecules apart (Yates, 1991). On the other hand, Suzuki et al., (2009) found that TPA forms very similar SA structures stabilized by hydrogen bonds on both the Si(111)–$\sqrt{3}$x$\sqrt{3}$–Ag and Ag(111) surfaces. The surface reactivity is a key parameter for semiconductor substrates which can be passivated via a metal overlayer (Suzuki et al., 2009), via hydrogen or oxide termination (Mayne et al., 2006; Bonilla et al., 2017), or via Group 13 dopants (Oura et al, 2013) among other methods (Sundaravel et al., 1999).

[10] Reproduced from Ref. (Suzuki et al., 2009) with permission from the PCCP Owner Societies.

3. Theory & Nomenclature

This chapter will introduce some of the notation necessary to understand the molecular arrangements within the data and the orientation of the substrates. As well, surface reconstructions of the substrates used is explained. Insight into the design considerations of our molecule is given along with theory surrounding the behaviour of similar molecules on metal surfaces.

3.1 Miller Indices

Miller indices are used to define particular planes of a crystal. Miller indices are determined using the intercept of the specified plane with the axes of the lattice vectors. The reciprocal of the origin-intercept distance is used to find the smallest set of integers having the same proportional value. For example, if the intercepts of a plane cross the axes of a lattice at values of 1;2;3, then the reciprocals are 1; ½; 1/3, and the Miller index is (621). In the case where the plane does not intercept an axis, the distance is infinite, and the reciprocal is taken as 0. An intercept along a negative axis is expressed with a bar above the index. Curly brackets indicate a set of crystallographic equivalent planes.

This thesis utilizes the (111) plane of various surfaces. The (111) plane can be described as the plane normal to a vector with equal components in all three lattice directions. This plane is visualized in figure 3.1 below.

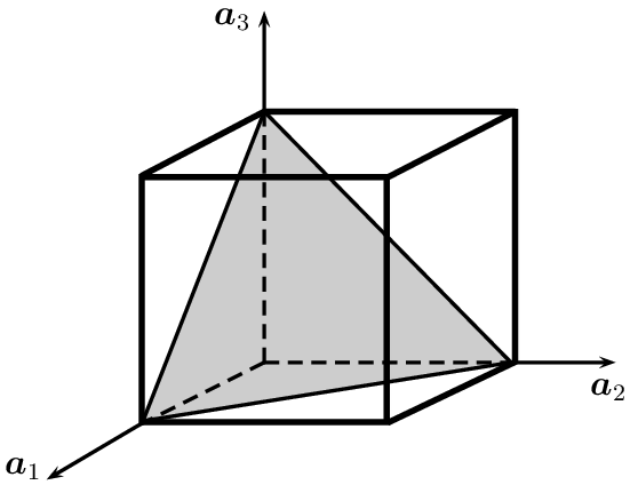

Fig. 3.1: The (111) plane of an arbitrary conventional cubic cell shown in grey.

3.2 Crystal Structures

One of the most common crystal structures of the elements is the face-centered cubic (fcc) structure. The fcc lattice structure is a cube with atoms at the corners and center of the six faces of the cube. This structure is shared by all of the coinage metals – copper, silver, and gold – they are all Group 11 elements. As well, the {111} planes are the most inert for these substrates. The relatively non-reactive {111} planes of the coinage metals, typically have higher diffusion coefficients than the remaining planes in the crystal (Ayrault & Ehrlich, 1974). This allows molecules to diffuse with high mobility when compared to the other crystal planes (Ayrault & Ehrlich, 1974; Oura et al., 2003). The high mobility for molecules on the {111} planes makes these surface planes an ideal substrate for 2-D SA network formation. However, the {111} planes of silicon are not naturally passive. Silicon has a diamond-cubic crystal structure. It can be described as two fcc structures offset by $\sqrt{3}/4$ of the lattice constant along the body diagonal.

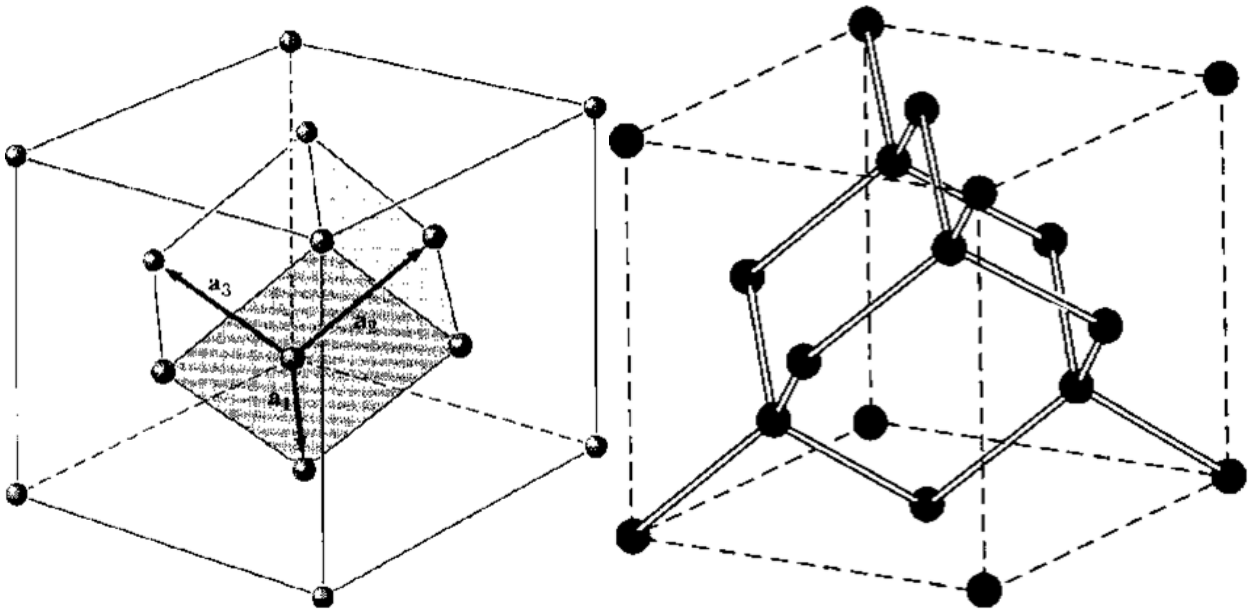

Fig. 3.2: Ball and stick representation of the fcc (left) and diamond-cubic (right) structures. The primitive and conventional cell is shown for the fcc. Only the conventional cell is shown in the diamond-cubic. (Kittel, 2004)[11].

For both the fcc and diamond-cubic structures, the lattice constant defines the side-length of the conventional cell. Information on the lattice parameter along with other data, can be found in the following table for the coinage metals and silicon.

Element	Atomic Number	Lattice Constant [Å]	Cubic Crystal Structures	Nearest Neighbour Distance [Å]	{111} Interatomic Spacing [Å]
Si	14	5.430	Diamond	2.351	3.839
Cu	29	3.61	Face Centered	2.55	2.55
Ag	47	4.09	Face Centered	2.89	2.89
Au	79	4.08	Face Centered	2.88	2.88

Table 3.1: Crystallographic data for silicon and the coinage metals. (Kittel, 2004)

Another common crystal structure is the hexagonal closed packed (hcp) structure. In the hard sphere model, we treat atoms as solid spheres and pack the "spheres" in a 2-D layer.

[11] Reprinted by permission from Copyright Clearance Center: **John Wiley and Sons**, **Wiley**, (Introduction to Solid State Physics, 8th Edition, Kittel, 1996), © **2004**

We denote the location of the spheres in the first layer as A-sites. If a second layer is added it will want to sit in the regions between the spheres of the initial layer, which we denote as B-sites. This process is repeated for a third layer and again the spheres will sit between the hollow regions between the spheres of the most recent layer. The third layer has two choices: if the third layer spheres sit directly above the first layer spheres (A-sites) the structure is hexagonal close packed. However if the third layer does not sit directly above the first, and instead sits at the spaces between the second layer, i.e. in C-sites, the resulting structure is fcc. See figure 3.3 below.

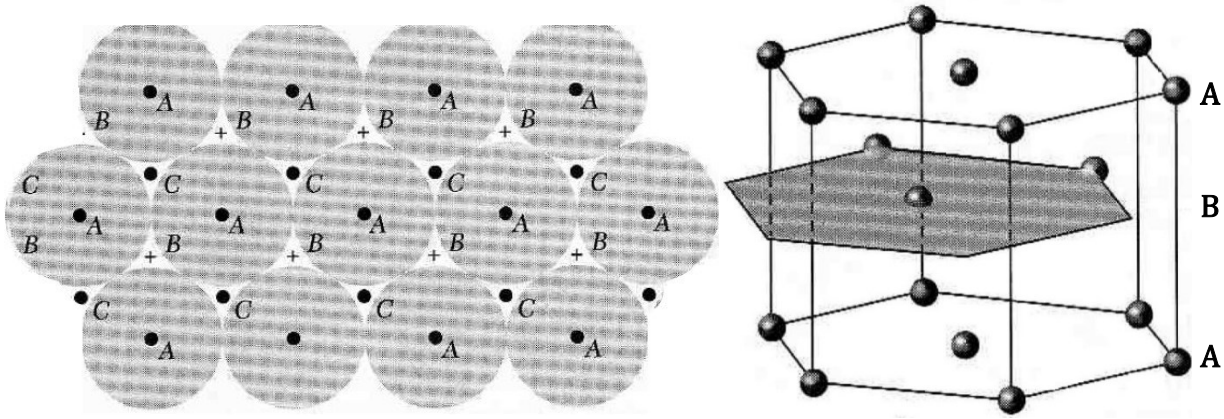

Fig. 3.3: Close-packed sphere stacking model of either fcc or hcp structures. ABABA is hcp and ABCABC is fcc (left). Ball and stick representation of the hcp structure (right). (Kittel, 2004)[11].

3.3 Wood's Notation

Wood's notation is used to describe the surface structure of crystal faces after they have undergone a lateral rearrangement. Surface rearrangement could be induced by doping, adsorption or thermal processes (Oura et al., 2003). As well, a reconstruction can be driven by a reduction in the surface free energy configuration (Oura et al., 2003). In Wood's notation, the ratio of lengths of the basic surface vectors to those of the modified surface vectors is given alongside any angle the new mesh makes with respect to the original. A surface vector can be

thought of the lattice vectors in the plane of the surface, assuming the bulk is suddenly truncated. The mesh, or the surface unit cell, refers to the area unit defined by the surface vectors of the 2-D lattice.

For example, on the surface plane (hkl) of element *Xx*, with original surface vectors $\mathbf{s_1}$ and $\mathbf{s_2}$, and reconstructed surface vectors $\mathbf{S_1}$ and $\mathbf{S_2}$, where

$$|\boldsymbol{S_1}| = \mathrm{M}|\boldsymbol{s_1}| \qquad |\boldsymbol{S_2}| = \mathrm{N}|\boldsymbol{s_2}| \tag{3.3.1}$$

the Wood's notation is expressed as

$$\mathrm{Xx(hkl)\ M \times N - R\theta^o} \tag{3.3.2}$$

provided there exists a rotation, θ, between reconstructed and original meshes. If there is no relative rotation the, "$-\mathrm{R}\theta^o$" is omitted. If the reconstruction is induced by a dopant or adsorbant, the element is indicated at the end, "–Yy". Strictly speaking, Wood's notation requires the original and reconstructed surface mesh to have the same symmetry, although in practice, Wood's notation is occasionally used despite the symmetry requirement. In cases where mixed symmetry meshes exist, matrix notation should be used.

3.4 Si(111)-√3x√3-R30°-B Surface Reconstruction

As mentioned previously the (111) planes of silicon are not suitable for SA baring intervention. One way to passivate and hence increase the surface mobility for molecules on a silicon face is through a boron induced surface reconstruction (Headrick et al., 1989). Boron atoms can chemisorb onto the (111) face of silicon and subsequently diffuse to a subsurface position inducing a √3x√3-R30° reconstruction (Lyo, Kaxiras & Avouris 1989; Avouris et al., 1990). Boron atoms within the bulk can also diffuse to the surface to induce this transition (Headrick et al., 1989). Boron atoms settle in the S5 subsurface position displacing a silicon atom to an adatom position. If we denote the topmost adatom silicon as located at the T4

position (Northrup, 1984), the S5 position would sit directly beneath the T4 position (Bedrossian et al., 1989). Vertically between the T4 and S5 there exists three silicon atoms in offset positions which are known as T5 positions (Northrup, 1984).

The substitution of boron at the S5 position induces a relaxation of the bonds to the T5 silicon atoms which is responsible for the rearrangement of the surface mesh. The B-Si bond is about 12% shorter than the Si-Si bond. Consequently, the three T5 atoms move inward, which decreases their separation by 10% relative to the bulk atomic spacing (Bedrossian et al., 1989). This inward relaxation is favorable, since the boron atom in the S5 position prefers smaller bond lengths (Bedrossian et al., 1989). This reduces the bond-angle stress at the T5 position. The shortening of S5 to T5 bonds can only happen to every other "S5" position; the result is that every second S5 silicon is displaced to the T4 adatom position, resulting in a new surface layer (Baumgärtel et al, 1999). The unreconstructed 1x1 silicon (111) surface atom separation is one half of the face diagonal in the conventional diamond-cubic cell (3.839 Å). The $\sqrt{3}$ reconstruction of the new surface dictates that the separation of raised surface atoms is 6.650 Å (Andrade et al., 2015).

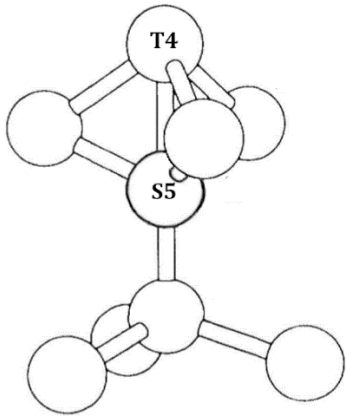

Fig. 3.4: Schematic diagram illustrating the first 5 layers of a diamond-cubic crystal in a (111) face orientation. The T4 and S5 position are marked. The dark outline of the S5 position corresponds to concentric T4 and S5 rings in the figure below.

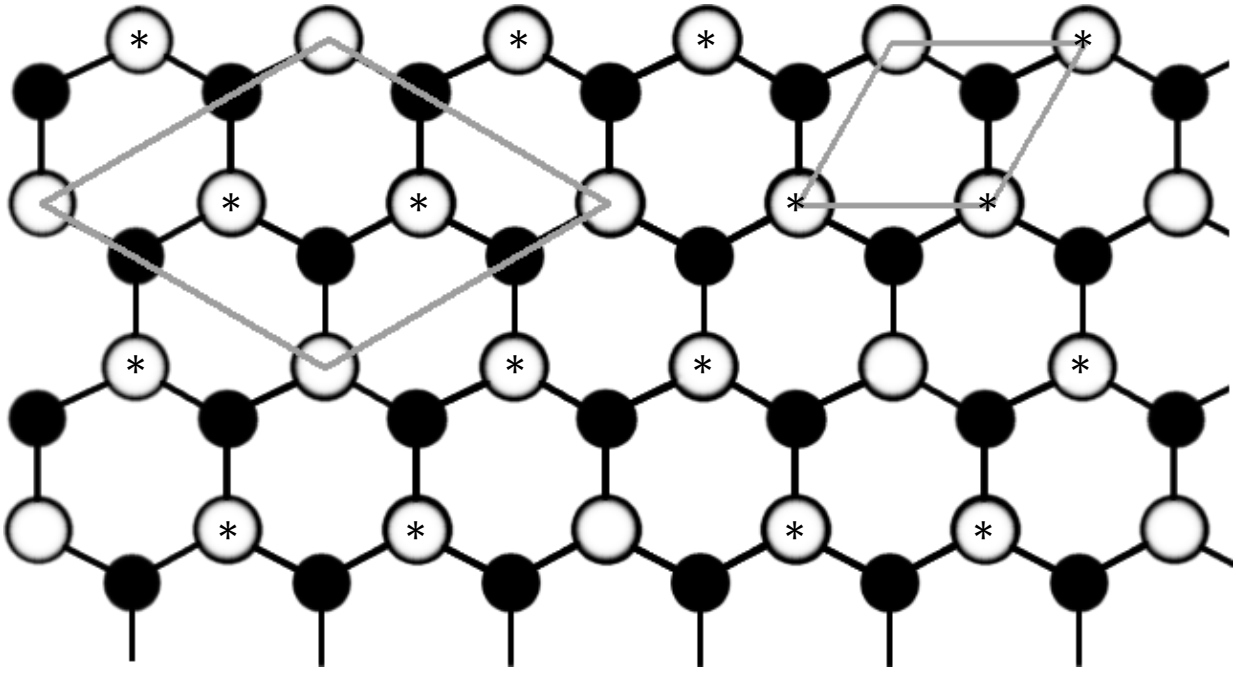

Fig. 3.5: Top down view of the Si(111)-$\sqrt{3}$x$\sqrt{3}$-R30^{o} reconstruction as induced by B substitution in the S5 position. The grey lines illustrate the $\sqrt{3}$x$\sqrt{3}$-R30^{o} and the 1x1 mesh. After reconstruction, the "white and hollow atoms" represent the top layer and second sub-layer. The "black atoms" are the first sub-layer. The "* atoms" represent either the first sublayer pre-reconstruction or the second sublayer after reconstruction.

The $\sqrt{3}$x$\sqrt{3}$-R30^{o}-B reconstruction is particularly important because it passivates an otherwise reactive silicon surface. Without reconstruction, the (111) plane of silicon contains many dangling bonds. Dangling bonds are unpaired electrons constrained by their associated atoms at the surface of a solid. The atoms which constrain the unpaired electron have too few bonding partners to satisfy its valence shell and so the unpaired electron can be thought of as a "dangling bond". Chemically, a dangling bond behaves very similarly to a free radical and is therefore very reactive, so much so, dangling bonds are sometimes called immobilized free radicals (Yates, 1991).

The benefit of the boron reconstruction is that charge transfer from the T4 Si atom to

the S5 B atom eliminates the surface dangling bonds of the topmost silicon atoms. Boron atoms are trivalent despite bonding to four neighbouring silicon atoms. To form four bonds, electrons are transferred from the dangling Si bonds to the boron atoms beneath the surface (Cao, Yang, & Pianetta, 1993). Passivation is essential in molecular epitaxy as a passive surface is required for surface diffusion and subsequent bottom-up self-assembly (Tan, & Zhang, 2019).

3.5 Muscovite / Mica

Mica is a class of inert, flat, crystalline solids. Visibly, mica could be easily mistaken for glass. Micas cleave easily along their basal plane. In particular, our lab makes use of the clear, colourless and odourless muscovite type mica. Muscovite is a hydrated phyllosilicate mineral of aluminium and potassium – $KAl_2(Si_3Al)O_{10}(OH)_2$ (Zhong, & Li, 2019). It crystallizes in a monoclinic structure with the unit cell consisting of an aluminum octahedral ($AlO_4(OH)_2$) sheet sandwiched between two silicate tetrahedral ($(Si, Al)O_4$) sheets. The sheets are held together by potassium cations (Zhong, & Li, 2019). Together the two sheets form one layer. Adjacent layers are weakly held together by van der Waals forces (Zhong, & Li, 2019). The weak interlayer forces explain why mica cleaves so readily (Zhong, & Li, 2019). The ability to cleave the material makes mica an ideal candidate to form clean, thin, inert sheets for epitaxial growth.

Mica was used in this work to support the growth of polycrystalline thin films of Au(111) in a high vacuum chamber – separate from the UHV system. The lowest energy surface of gold is the exposed (111) plane. After initial formation of the gold thin film samples, they are annealed with a torch to promote recrystallization into large crystallites with (111) termination.

3.6 Herringbone Reconstruction

The (111) surface of gold has a 22x√3 reconstructed surface mesh, known as the herringbone reconstruction. The reconstruction is energetically motivated by the reduction of 12 nearest neighbours in the bulk compared to 9 available at the surface (Ohring, 2001). The herringbone surface reconstruction of gold (111) is due to mismatched fcc and hcp areas. Between the mismatched fcc and hcp locations are bridging sites. The bridging sites result from a surface compression caused by a uniaxial stress (Chambliss, Wilson, 1991; Chambliss, Wilson & Chiang, 1991). The bridging atom sites are displaced by 0.20 Å, while hcp atom sites are displaced by 0.12 Å, with respect to the fcc regions (Dishner et al., 1997).

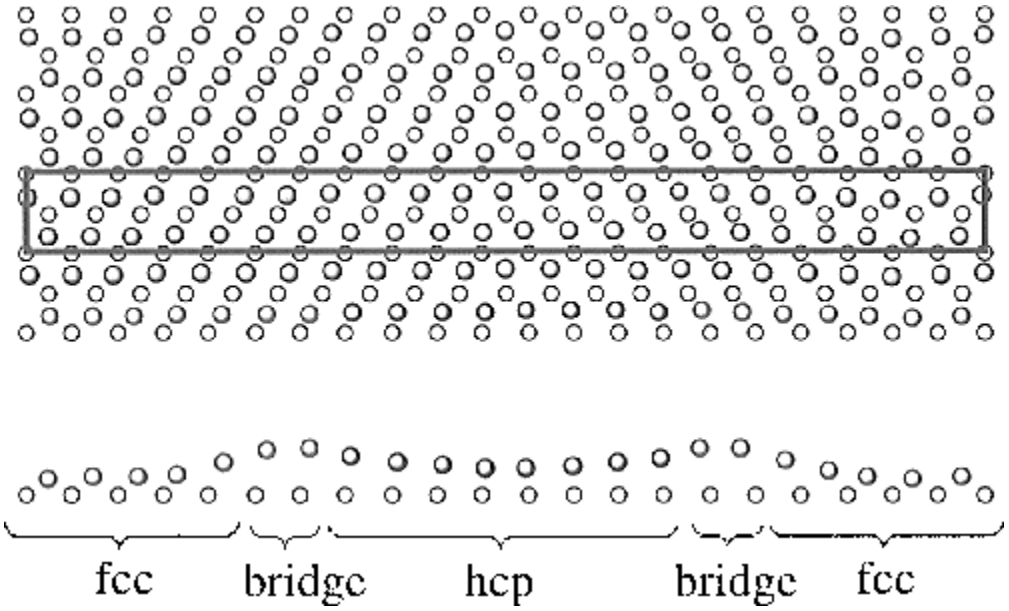

Fig. 3.6: Top: Bird's eye view of the gold 22×√3 reconstruction. The 63 Å x 5 Å unit cell is highlighted. The experimentally observed herringbone is a result of stacking these unit cells along the 5 Å direction. Bottom: Side view of the reconstructed surface. (Dishner et al., 1997)[12]

[12] Reprinted with permission from Direct observation of substrate influence on chemisorption of methanethiol adsorbed from the gas phase onto the reconstructed Au (111) surface, Mark Dishner, Langmuir, 13(8), 2318-2322. Copyright 1997 American Chemical Society.

3.7 TBTANGO

Tribromotrioxoazatriangulene (TBTANGO) was the primary molecule we chose to study in this thesis. No other molecule is reported on in this work. TBTANGO is a triphenylamine derivative and a member of the heterotriangulene family (Fang et al., 2009). Triphenylamine is a well-known hole-transport material used in optoelectronic devices (Agarwala & Kabra, 2017; Jing & Heine, 2018) which suggests TBTANGO and other engineered triphenylamine derivatives are strong candidates for use in future molecular electronics as 2-D conjugated polymers with non-zero bandgaps (Galeotti et al., 2020). TBTANGO is shown in figure 3.7 below. The TBTANGO used in this work was synthesized in Montréal by the research group of Professor Dimitrii Perepichka at McGill University. The procedure for the synthesis of TBTANGO was adapted from Fang et al. (2009) and is published by Galeotti et al. (2020).

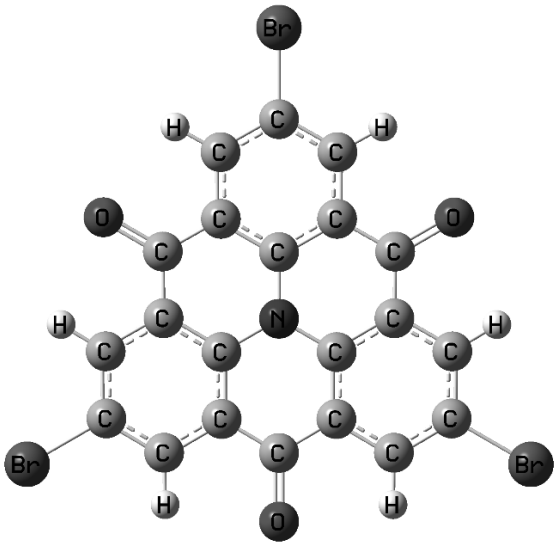

Fig. 3.7: Ball and stick representation of TBTANGO. Atoms are labelled by their chemical symbol.

The carbonyl bridges between phenyl groups act as a rigid link to ensure a planar geometry (Fang et al., 2009; Galeotti et al., 2020). The flat geometry improves π-conjugation

within the molecule and modulates the electronic properties via electron-withdrawing effects (Cai et al., 2013; Galeotti et al., 2020). The terminal bromine atoms enable TBTANGO monomers to leverage halogen-halogen interactions for SA. Moreover, under certain conditions the halogen atoms can dissociate, potentially allowing adjacent monomers to form 2-D self-assembled metal-organic networks or to C-C couple to one another via Ullmann coupling (Steiner et al., 2017). TBTANGO contains a central nitrogen atom. The inclusion of nitrogen (or other atoms such as boron) produce modifications to the resulting electronic properties of any realized SA layers or 2-D nanomaterial.

For example, band structure (Jing & Heine, 2018; Adjizian et al., 2014) and π-conjugation (Fang et al., 2009) are modified by the inclusion of such atoms. Jing & Heine, (2018) used density functional theory calculations to study 2-D polymers made from heterotriangulene units. They found that varying the central atom between carbon, boron, or nitrogen changed the band structure of the polymer. The heterotriangulene unit with a carbon atom formed a semimetallic polymer, with Dirac cones at the K point of the Brillouin zone. Boron or nitrogen-based units formed single-band semiconductors – materials with either exclusively electron (N center) or hole (B center) carriers. Fang et al., (2009) report the three N-C bonds to be essentially in one common plane supporting π-conjugation to the attached phenyl rings.

3.8 Reaction Mechanism for Surface-Confined Metal-Organic Networks from Halogenated Precursors on Coinage Metals

The deposition of TBTANGO on the Ag(111) surface results in dehalogenation of the constituent monomers and the formation of a 2-D organometallic phase. In this study, the organometallic structure represents the final state formed on the silver substrate. In the

literature however, the formation of the organometallic state on coinage metals is often discussed within the full context of Ullmann coupling and the formation of 2-D polymers. The discussion of the Ullmann reaction is only presented herein to elucidate the chemistry of our final organometallic state.

Strictly speaking, the Ullmann reaction originated as a method to form aryl halides in solution using a copper catalyst. However, Xi and Bent, (1992), first demonstrated that the reaction can also proceed on surfaces. They proposed two mechanisms following the same reaction pathways as the in-solution variant (Xi & Bent, 1992). The distinction between the two mechanisms is whether a surface adatom or lattice atom bonds to the organic precursor (Xi & Bent, 1992). Since the work of Xi & Bent (1992), on-surface Ullmann reactions have been demonstrated with a variety of halogen and metal substrates (Wang et al., 2011; Di Giovannantonio et al., 2013; Di Giovannantonio et al., 2016; Dong et al., 2015; Basagni et al., 2015; Fan, Zhu & Gottfried, 2018). Herein, on-surface Ullmann-like reactions will be referred to as Ullmann reactions. Figure 3.8 of the full Ullmann reaction is included for completeness. The reductive elimination of the organometallic structure to form carbon linked monomers is not considered in this work.

The reaction mechanism forming the organometallic structure of the Ullmann reaction is focussed on in this work. This mechanism is known to result in a metal-carbon linkage between the substrate and the halogenated organic molecule. The formation of the organometallic structure has been demonstrated on copper (Di Giovannantonio et al., 2013; Di Giovannantonio et al., 2016; Pham et al., 2016; Galeotti et al., 2017), silver (Cardenas et al, 2013; Eichorn et al., 2014a; Zhang et al., 2020) and gold (Eichorn et al., 2014b; Gatti et al., 2014; Pham et al., 2016) surfaces. In this context, copper is the most reactive of these

substrates, with silver being more reactive than gold (Walch et al., 2010; Galeotti et al., 2019). The amount of thermal activation required for the reaction to proceed increases in inverse order of reactivity (Walch et al., 2010; Shi et al., 2016; Galeotti et al., 2019).

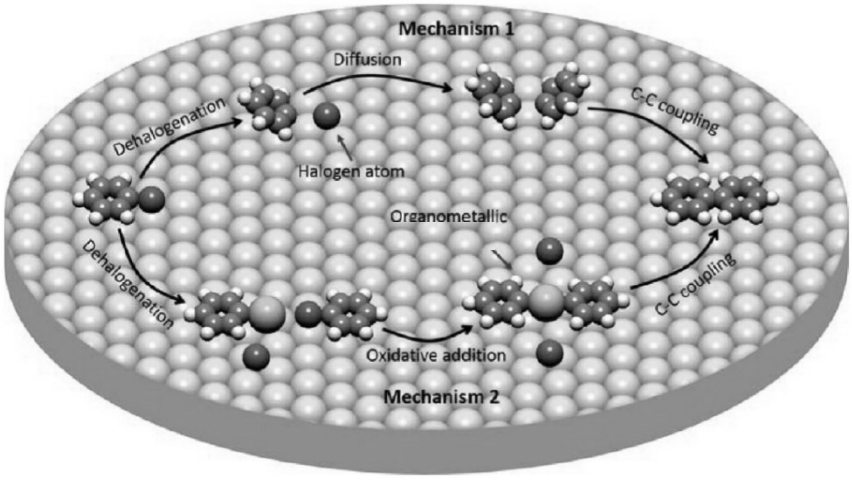

Fig. 3.8: Schematic of the on-surface Ullmann-like reaction illustrating the two reaction mechanisms and potential polymerization. The final polymer covalently linked state is not considered. (Fan, Gottfried & Zu, 2015)[13]

The proposed ionic mechanism of the Ullmann reaction explains the chemistry of dehalogenation and organometallic formation. This mechanism begins with the oxidative addition of a coinage metal to the aryl halide followed by a single electron transfer (SET) to form an organo-metal reagent. This organo-metal performs another oxidative addition on an aryl halide which forms the biaryl metal complex (Mondal, 2016). The reaction mechanism is illustrated in figure 3.9. The process occurs at other halogenated sites of the precursor molecules to create a SMONs (Björk, 2016; McCarty & Weiss, 2004; Di Giovannantonio et al., 2016). The reaction of TBTANGO on Ag(111) forms an organometallic phase via the reaction mechanism discussed up to the organometallic state. In the complete reaction, the biaryl metal

[13] Reproduced from (Fan, Gottfried & Zu, 2015), an open-source article. This is an unofficial translation of an article that appeared in an ACS publication. ACS has not endorsed the content of this translation or the context of its use.

complex eliminates the metal resulting in a covalently linked surface-confined polymer.

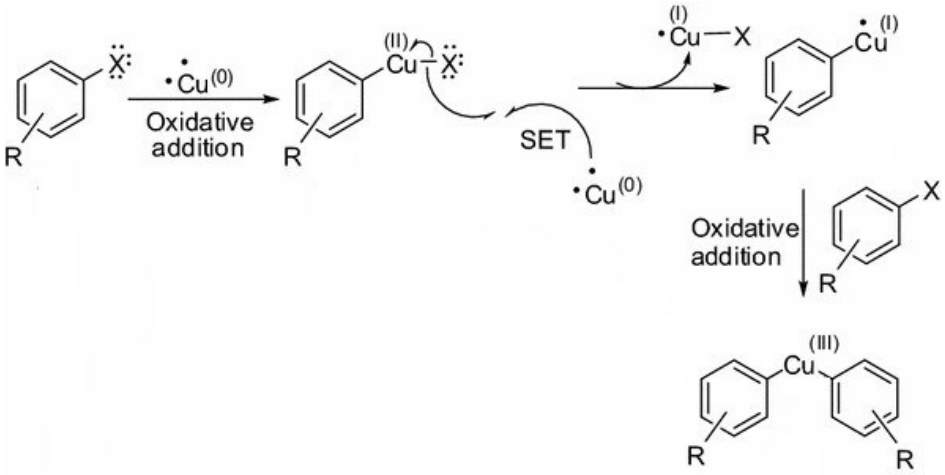

Fig. 3.9: The proposed ionic mechanism of our final state organometallic structure which is typically an intermediate state of Ullmann coupling. This diagram uses the historical copper substrate although any coinage metal can support the reaction. (Mondal et al., 2016)[14]

[14] Reprinted by permission from Copyright Clearance Center: **Springer Nature**, **CHEMTEXTS**, (Recent advancement of Ullmann-type coupling reactions in the formation of C–C bond, Mondal et al, 2016), © **2016**

4. Equipment & Experimental Methods

This chapter explores the theoretical underpinnings of the instrumentation used in the laboratory to prepare and monitor the surfaces studied. Specifications of the equipment is given where known. Surface techniques such as Auger electron spectroscopy, low-energy electron diffraction, and scanning tunnelling microscopy are explained in depth. Sample data is given to facilitate the interpretation of later results. The chapter closes with a brief commentary on density functional theory used to corroborate the experimental findings.

4.1 Pumps & Ultra-High Vacuum

4.1.1 Turbomolecular Pump

A variety of pumps are used to achieve ultra-high vacuum in our chamber. The initial evacuation is accomplished by a turbomolecular pump in conjunction with its backing pump. Turbomolecular pumps, or "turbos" as they are affectionately called, are commonly used for their high pumping speed, large compression ratios, low ultimate pressures and the fact that they do not backstream oil. In our laboratory, a Varian Turbo-V60[15] is used. The turbo operates at an impressive 70,000 rpm to achieve a pumping speed of 65 L/s for nitrogen and an outlet pressure to inlet pressure ratio of $5x10^7$. Turbos operate under the principle of momentum transfer. High speed rotating blades 'bat' gas molecules imparting a change in momentum upon them. In addition, turbos contain stationary slotted stator blades oriented opposite to that of the slotted rotating blades. The alternating alignment of the blades give the gas molecules a much higher probability of being transmitted to the outlet side of the pump rather than to the inlet.

[15] Agilent Technologies Inc, www.agilent.com

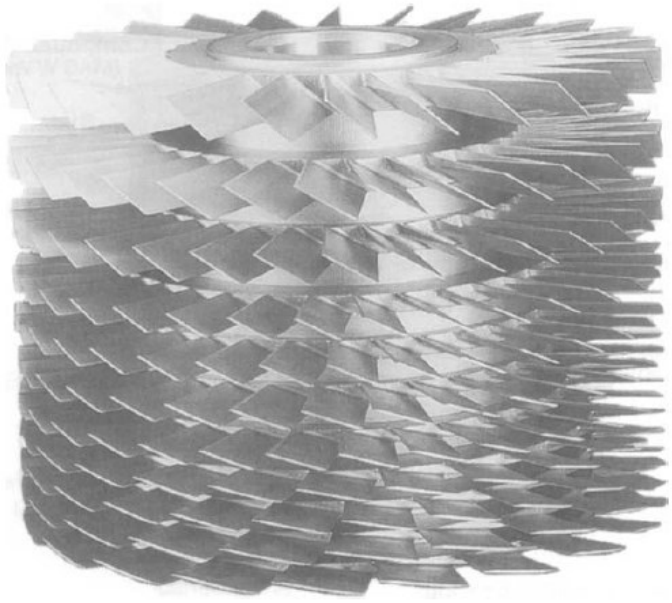

Fig. 4.1: A rotor from a typical turbomolecular pump. Blades are angled less heavily towards the bottom of the assembly. This section of blade assembly increases the compression ratio at the expense of pumping speed. (O'Hanlon, 2005)[16]

Pumps which operate under the principle of momentum transfer, such as turbomolecular or diffusion pumps, work best in the molecular flow regime, where the mean free path of gas molecules is much larger than the container size, therefore, turbo pumps cannot exhaust to atmosphere and must be backed by a foreline pump.

4.1.2 Two-Stage Rotary Vane Pump

Our turbo pump is backed by a two-stage rotary vane pump. Our foreline pump, was produced by Can-Vac Technologies[17]; it has a pumping speed of 5.95 m^3/hour. In a rotary vane pump, air is compressed between a rotor and a vane in a crescent shaped cavity. In a two-stage rotary vane pump, this process is repeated twice before the gas is discharged through an

[16] Reprinted by permission from Copyright Clearance Center: **John Wiley and Sons**, **Wiley**, (A User's Guide to Vacuum Technology, 3rd Edition, O'Hanlon, 2004), © **1969**

[17] http://canvactech.ca/wp

exhaust valve to pump fluid and subsequently the atmosphere. The surfaces between the vane(s), rotor(s) and housing are sealed by pump fluid.

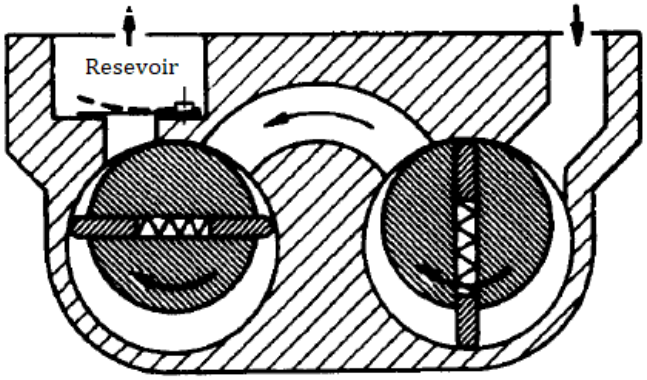

Fig. 4.2: A cross section view of a basic two-stage rotary vane pump. (O'Hanlon, 2005).[18]

4.1.3 Ion Pump

All of the remaining pumps used to achieve vacuum in our laboratory are types of entrainment pumps. Entrainment pumps do not backstream oils and are often called clean pumps (O'Hanlon, 2005). The three entrainment pumps we use are an ion pump, titanium sublimation pump (TSP) and a non-evaporable getter pump (NEG). The main pump used to achieve and maintain the pressure in our chamber is the ion pump. It is a Varian VacIon Plus 150[19] diode style ion pump. It boasts an ultimate pressure below 10^{-11} Torr and a pumping speed of 150 L/s for nitrogen.

Ion pumps are essentially a collection of Penning cells. A Penning cell uses a combination of static magnetic (~0.1T) and electric (~1kV) fields, to trap electrons which ionize gas particles so the ions may be pumped. Electrons are emitted from the cathode. The magnets are oriented such that the Lorentz force induces the electrons to travel a spiral path

[18] Reprinted by permission from Copyright Clearance Center: **John Wiley and Sons**, **Wiley**, (A User's Guide to Vacuum Technology, 3rd Edition, O'Hanlon, 2004), © **1969**

[19] Agilent Technologies Inc, www.agilent.com

before reaching the anode. The increased path length of the electrons increases the probability of ionizing collisions with gas molecules (O'Hanlon, 2005). The ions produced are then accelerated towards the cathode.

Ions that reach the cathode can either i) sputter fresh cathode material, ii) bury themselves in the cathode material or iii) generate more electrons to be accelerated by the fields.

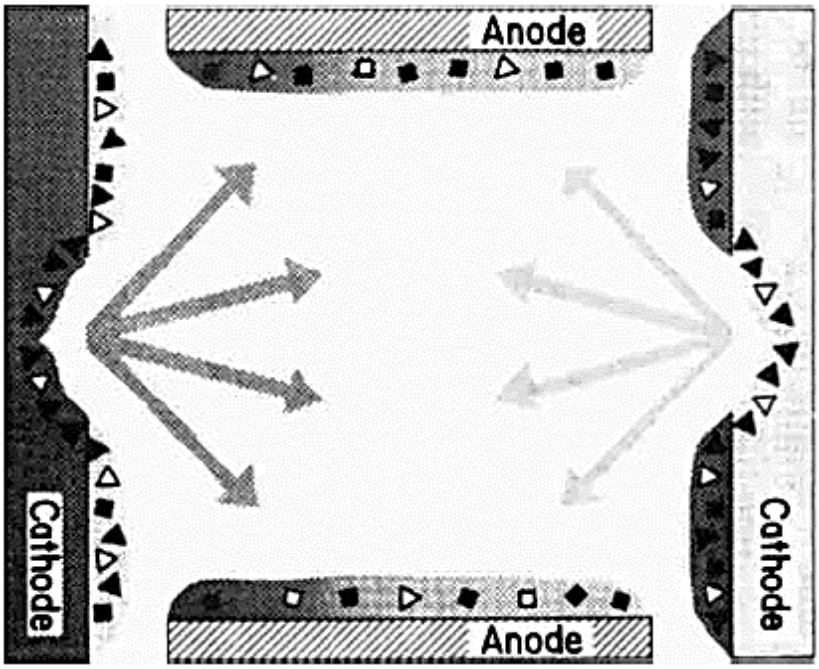

Fig. 4.3: A Schematic diagram showing pumping mechanisms in a Penning cell. Squares represent neutral particles and triangles represent ionized particles before burial. (O'Hanlon, 2005)[20]

The cathode in a Penning cell is made from a metal such as titanium that can react with, or *getter*, gases. The material that is sputtered off the cathode getters gases in the cell. This process, along with ion burial, effectively removes the gas ions from the chamber. Many other

[20] Reprinted by permission from Copyright Clearance Center: **John Wiley and Sons**, **Wiley**, (A User's Guide to Vacuum Technology, 3rd Edition, O'Hanlon, 2004), © **1969**

processes are present in a Penning cell such as molecular dissociation or ion-electron neutralization. The molecular fragments and fast neutral atoms are still subject to burial and gettering (O'Hanlon, 2005).

4.1.4 Titanium Sublimation Pump

Titanium sublimation pumps (TSP) and non-evaporable getter pumps (NEG) are subtypes of entrainment pumps known as getter pumps. In a TSP, titanium is sublimated typically by a filament and deposited as a thin layer onto a surface. The freshly sublimated layer of titanium inside the chamber is the active pump. To continuously pump, a fresh layer of titanium must be periodically deposited. In our laboratory, a fresh layer was deposited every several days.

Different gases are pumped at different rates by the TSP. Each gas has a unique sticking coefficient, which determines the likelihood the gas will be adsorbed by the titanium. A gas with a higher sticking coefficient can displace a gas with a lower sticking coefficient. More information of the sticking coefficient of various gases can be found in Gupta & Leck (1975).

4.1.5 Non-evaporable Getter Pump

Unlike surface getter pumps such as TSPs, non-evaporable getter pumps (NEGs) are a bulk getter pump. After gases adsorb onto the surface, they diffuse into the bulk of the material. NEGs are made from high surface area, porous materials such as zirconium alloys. Our lab uses a Capacitor-D400 NEG pump[21] made by SAES Getters. The getter material is a 70% zirconium, 24.6% vanadium and 5.4% iron mix. Each time a NEG is exposed to atmosphere it must be "regenerated" because exposure to atmosphere will cause the entire surface area to be enclosed by a thick outer layer of oxides and nitrides. Regeneration then is

[21] SAES Getters, S.P.A, http://seasgetters.com

the process which prepares the getter surface for pumping. To regenerate a NEG pump, the pumps are usually heated between 150^{o}C to 300^{o}C.

During the regeneration process, NEG pumps will outgas diatomic hydrogen. All other gases are entrapped permanently by NEG pumps and are not released during regeneration (O'Hanlon, 2005). Following regeneration, gases in the chamber are pumped by reaction with the NEG surface. The pumping speed for active gases (such as carbon oxides, oxygen or water vapour) is determined by the gas diffusion rate into the bulk. The NEG continues to pump until enough gas has been adsorbed to completely coat the NEG surface as before regeneration. In ultrahigh vacuum, the pumping duration after regeneration is many years for our Capacitor-D400 NEG pump.

4.1.6 Baking

Baking, as it is called, refers to the stimulated thermal desorption of the surface science chamber to reach ultra-high vacuum (UHV). This step is absolutely necessary as solids at standard temperature and pressure are a vessel for gases to dissolve into or adsorb onto. If an unbaked system is allowed to continue pumping without baking, it would take ~11,400 years to reach ultra-high vacuum (O'Hanlon, 2005). With the intervention of baking, this process can be accelerated to several days. Outgassing rates are heavily dependent on temperature. O'Hanlon (2005) has calculated the residence time for water chemisorbed onto a metal surface as 10^{5} seconds at 22^{o}C but only a measly 10^{-5} seconds at 450^{o}C. In our laboratory, the chamber is held around 100^{o}C for three days to desorb the gases within the chamber. This is achieved by using long resistive heaters wrapped around the chamber. The resistors are coated in a carbon fibre sheath to prevent electrical short circuits. The current is adjusted with portable transformers. The entire chamber is wrapped in a reflective blanket.

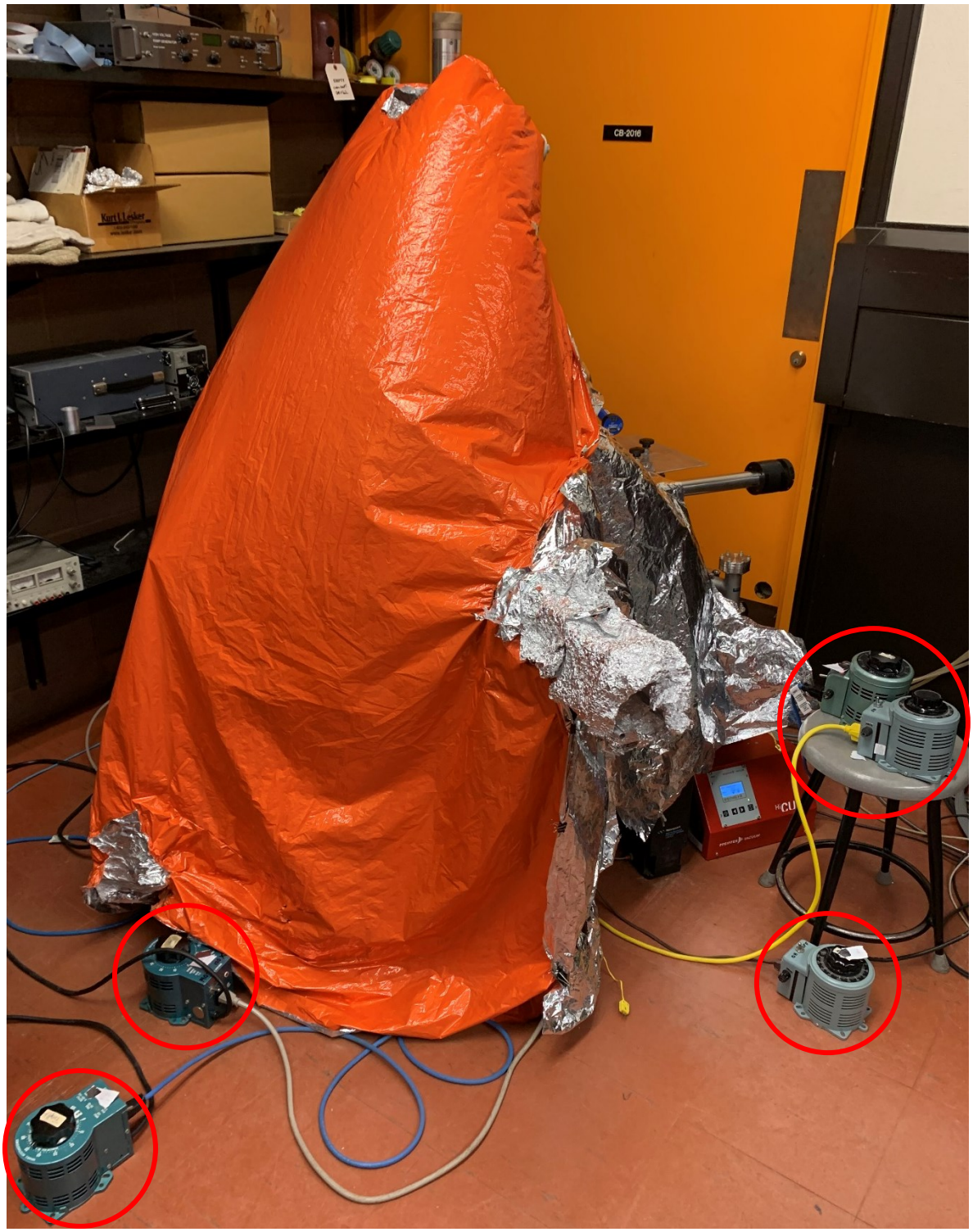

Fig. 4.4: Our UHV chamber during the baking process. Variable AC power supplies are circled in red. Temperatures are monitored with thermocouples.

Following a bake out, the ultimate pressure, or the lowest pressure of the chamber, is

achieved. The ultimate pressure is achieved when the outgassing rate from the chamber walls is in equilibrium with the chamber's pumping capacity. The ultimate pressure achieved in our chamber is less than $1x10^{-10}$ Torr. In our laboratory, a more typical pressure is approximately $2x10^{-10}$ Torr, due to ongoing experiments which increase the pressure as consequence of outgassing. The low pressures allow us to work with reactive surfaces such as silicon without immediate contamination.

4.2 Other Equipment

4.2.1 Ion Gauge

Our vacuum chamber uses a nude Bayard-Alpert ion gauge to monitor the main chamber pressure. Ion gauges use a filament to emit electrons which ionize nearby gas molecules. The positive ions are collected, and this current is proportional to the number density of the gases. Knowledge of the gauge's sensitivity, which is dependent on a host of parameters, is necessary to convert the ion current into a pressure reading. Gauge sensitivity is unique for each gas. Usually gauges are calibrated for nitrogen and the relative sensitivity is needed to gain a pressure reading for a different gas.

Figure 4.5 contains two images of standard and UHV grade nude Bayard-Alpert gauges. Nude gauges are not shielded by glass. Both gauges contain a filament for producing electrons, a grid to accelerate ions, and an ion collector. The UHV grade has a capped grid and much thinner inner collector which increases the measurable limit. The thin collector is less likely to capture X-rays generated from electrons striking the grid. X-rays captured by the collector induce a current which is indistinguishable from the ion flow (O'Hanlon, 2005).

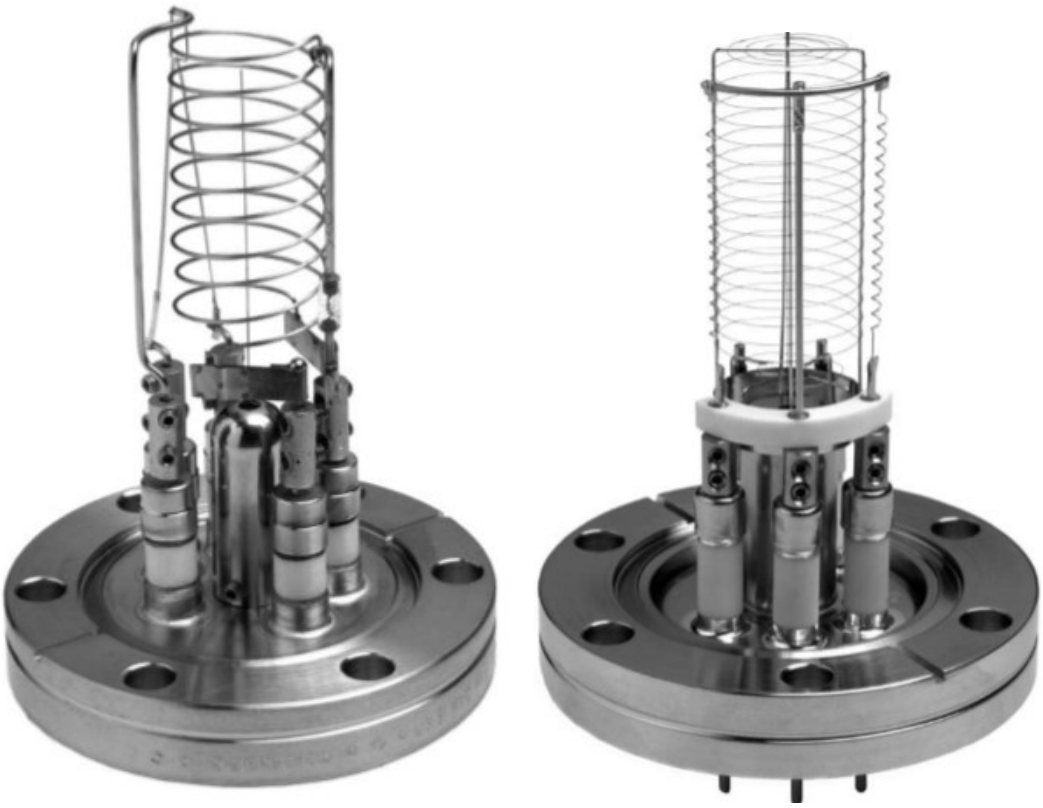

Fig. 4.5: A non UHV-grade (left) and UHV-grade (right) Bayard-Alpert gauge. Note the difference in wire thickness and grid end.[22]

4.2.2 Thermocouple Gauge

To introduce samples into the UHV chamber, we utilize a load lock chamber. The load lock is connected to the main chamber via a gate valve. We can pump on either the load lock or the main chamber independently using our turbomolecular pump. To roughly monitor the pressure of the turbo's backing pump, a thermocouple gauge is integrated to the turbo's foreline.

A thermocouple gauge utilizes an internal thermocouple to measure pressure dependent heat flow. A filament near a thermocouple gauge is heated to a certain temperature

[22] Stanford Research Systems. Retrieved from www.thinksrs.com/downloads/pdfs/applicationnotes/IG1selectapp.pdf

via a constant current. Typically, the thermocouple's measurement junction is spot welded to the midpoint of the current carrying wire (O'Hanlon, 2005). As gases interact with the filament, heat is transferred away (at a rate dependent on the thermal conductivity of the gas), which causes a change in temperature of the filament. The change in temperature is measured as a voltage output and is converted to a pressure. The higher the pressure, the greater the temperature change.

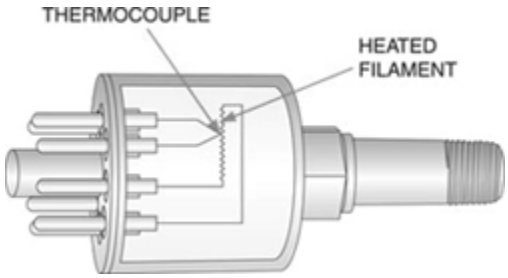

Fig. 4.6: A simple schematic illustrating the basic concept of the thermocouple gauge.[23]

Thermocouple gauges are notoriously unreliable. For example, oxide build up on the output posts of the gauge connectors can affect the reading. At best the gauge gives a rough idea of the pressure at the inlet of the roughing pump.

4.2.3 Quadrupole RGA

Residual Gas Analyzers (RGAs) are used to measure the ratio of the mass-to-charge of an ionized atom or molecule. Molecules are ionized, then directed through a quadrupole electric field, to a detector. Gases are ionized in much the same manner as in ion gauges – electron impact ionization. Accordingly, positive ion production is not the same for all gases; the sensitivity is normalized to nitrogen. Unlike an ion gauge, an RGA counts each ion's mass-to-charge ratio separately. Furthermore, an ion gauge makes no distinction between N^+ and

[23] © Stanford Research Systems. Retrieved from www.thinksrs.com/downloads/pdfs/applicationnotes/IG1selectapp.pdf

N_2^+ ions, whereas the RGA does. This allows users to identify different gas species based on the mass-to-charge ratio.

Our RGA is a Stanford Research Systems[24], RGA100, quadrupole mass analyzer. The quadrupole field is the functional component inside the RGA which allows it to distinguish particles with a sort of "band-pass" filter. Sweeping over various mass-to-charge ratios linearly in time produces scans ranging over hundreds of amu in a matter of seconds. The quadrupole itself is constructed of two pairs of pole shaped electrodes, each set with an opposite DC offset. The potential is zero along the axis of symmetry. As well, each set of poles has a RF field, or VAC, which creates potential "hills" for ions that are too light or too heavy. Instability in the trajectory of ions outside of the selected mass range are filtered out before or at the screen of the detector (O'Hanlon, 2005).

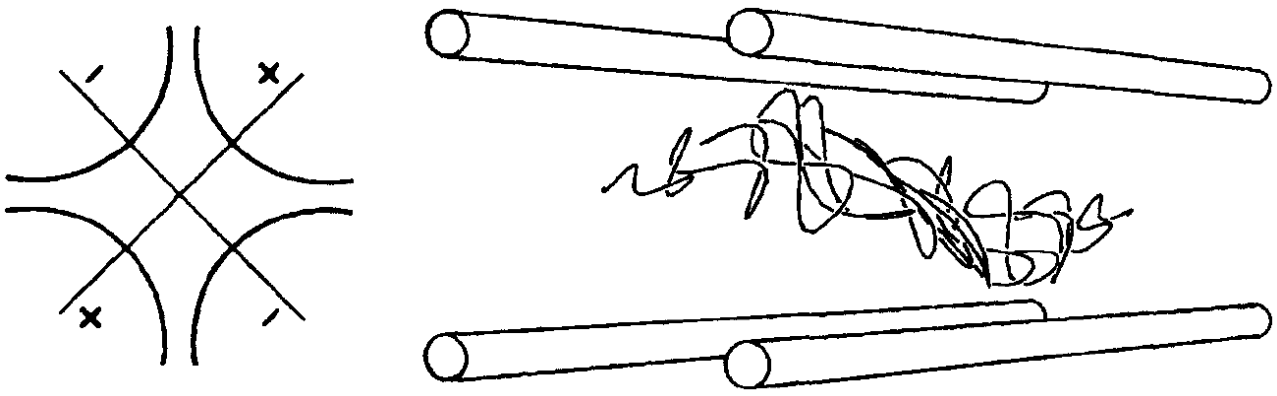

Fig. 4.7: Quadrupole mass filter's hyperbolic electrode cross section (left) and conceptual ion path (right). (O'Hanlon, 2005)[25]

Solving for the path of the ion in a quadrupole field is mathematically quite complex as this problem reduces to solving the Mathieu equations in the x- and y-directions. This cannot

[24] www.thinksrs.com/products/rga.html

[25] Reprinted by permission from Copyright Clearance Center: **John Wiley and Sons**, **Wiley**, (A User's Guide to Vacuum Technology, 3rd Edition, O'Hanlon, 2004), © **1969**

be done analytically and is complicated by the fact that there exists a range of suitable entrance angles and velocities (O'Hanlon, 2005). A rigorous explanation of the mathematics can be found in the work of Major et al. (2005).

4.2.4 Evaporator

A repurposed electron beam evaporator is used in our lab for molecular deposition. The device is manufactured by tectra[26] and is a single evaporator – that is it has one crucible for holding molecules. The footnote provides the exact product listing from tectra's website. For crucible temperatures $<500^{o}C$, it is possible to forgo the high voltage and electron beam feature and to use the thermal radiation from the hot filament to heat the crucible. Our crucible is Alumina. Overall, the evaporator is a very flexible instrument capable of being fitted with many options – e.g. a flux monitor or a PID (feedback) controller. While our lab does not utilize all the features of the evaporator, our evaporator is regularly used with the shutter, thermocouple and water-cooling options. The thermocouple used in the evaporator is a type C thermocouple.

4.2.5 Pyrometer

Our lab uses an infrared pyrometer to monitor the temperature of silicon wafers in UHV remotely from outside the chamber. The pyrometer is an Ircon[27], Ultimax-20P handheld non-contact thermometer. Pyrometers operate on the Stefan-Boltzmann law modified to account for the radiative emissivity of various surfaces.

$$j^{*} = \varepsilon\sigma T^{4} \qquad (4.2.5.1)$$

[26] www.tectra.de/deposition-progress/e-beam-evaporator/
[27] www.flukeprocessinstruments.com/en-us/products/infrared-temperature-solutions/spot-pyrometers

j* is the total power per unit area radiated across all wavelengths, ε is a dimensionless constant known as the emissivity, σ is the Stefan-Boltzmann constant and T is the temperature in Kelvin. Typically, pyrometers use a system of optical lenses to collimate the radiation onto an internal detector. The Ultimax-20P specifically, measures a single wavelength at 960nm and uses an internal silicon photodetector.

4.2.6 Sputter Gun

Metal single crystal substrates in our laboratory are cleaned via ion sputtering. Argon atoms are ionized by a filament within our IPS model sputter gun. It is manufactured by OCI Vacuum Microengineering[28] and features a selectable filament current, source bias and beam focus. In our instrument, the sample is grounded, and the source is biased to ~1 kV. Different substrates, such as copper or silver, require various sputtering biases, 500V and 800 V respectively, to dislodge contamination while causing the least surface damage. When sputtering, our chamber is backfilled to an equilibrium pressure of $5x10^{-6}$ Torr of argon gas. Argon is pumped out by our turbomolecular pump. The argon is leaked in through the sputter gun where a portion of the gas is ionized and accelerated. The collision of the accelerated argon ions with the substrate is used to clean it. Surface atoms are knocked off by momentum and energy transfer. The fresh metal surface of a noble metal substrate, such as silver, is relatively inert. They do not getter gases. After sputtering, the metal crystals must be annealed to repair the surface of sputter damage. Annealing heals the pits and divots introduced by the sputtering.

[28] www.ocivm.com/

4.3 Surface Analytical Techniques

4.3.1 Auger

Auger electron spectroscopy (AES) is an analytical technique used to determine the elemental composition of the atoms in the near surface region of a solid material. The binding energy of a core level electrons is a sensitive function of the atomic identity. Thus, kinetic energy measurements of ejected electrons can identify the emitting elements. The Auger process was first described by French physicist Pierre Auger in 1925. An Auger electron spectrum plots either the number of electrons or the first derivative of the number of electrons versus kinetic energy. The derivative plot is much more useful in peak identification because the derivative easily shows changes in the signal strength due to Auger electrons. The signal is otherwise dominated by a large background due to secondary electrons. Elements are identified by the energy positions of the Auger signals, while the surface concentration of the element is related to the peak intensity.

The Auger process begins with the ionization of a core level of an atom. Ionization can be induced by electron impact, ion bombardment, or X-ray irradiation. Our instrument utilizes an electron beam for ionization. Following core level ionization, the process can be explained by the conservation of energy. An electron from a higher atomic level relaxes to fill the core level vacancy, creating a vacancy where it left. To conserve energy, an Auger electron is simultaneously ejected with kinetic energy equal to the difference of the singly ionized initial state and the doubly ionized final state (Hedberg, 1995).

Auger transitions are typically labelled by the energy levels of the electrons involved, using X-ray spectroscopy nomenclature. The first label corresponds to the energy level of the initial core hole. The second and third labels refer to the initial energy levels of the two

electrons involved in the Auger transition. Thus, the Auger transition shown in figure 4.8 is a KLL transition.

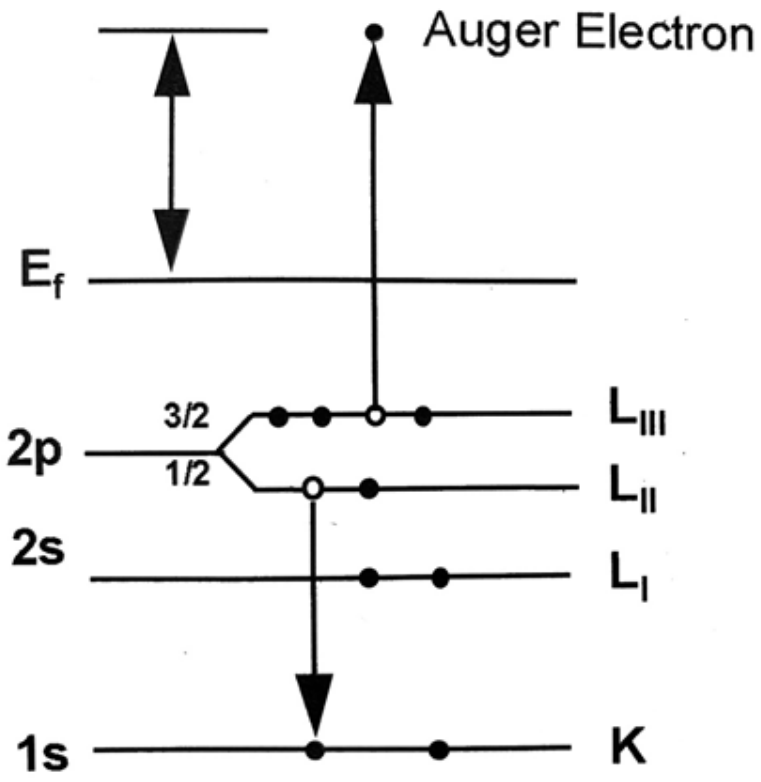

Fig. 4.8: Schematic diagram of the Auger process showing the filling of the core level hole and Auger electron emission. Creation of the K shell hole is not considered here.

For example, the Auger decay of a 1s core hole can be written:

$$KE_{KLL} = |E_K| - |E_{L_{II}}| - |E^*_{L_{III}}| \qquad (4.3.1)$$

where E* is the binding energy of a level already in the presence of a core hole. In AES, binding energies are commonly measured with the zero of energy taken at the Fermi level. More formally, the zero should be taken as that at the vacuum level (Briggs & Seah, 1983).

More exact calculations of the Auger energies also account for the Coulomb repulsion between the two holes in the final state and the relaxation energies. Including these effects, the equation for the kinetic energy of an Auger electron can be written:

$$KE_{KLL} = |E_K| - |E_{L_{II}}| - |E^*_{L_{III}}| - |H| + |P| \qquad (4.3.1.1)$$

where H is the hole-hole interaction energy of the two-hole final state, and P accounts for any screening polarisation or relaxation effects (Woodruff & Delchar, 1994).

Not all elements have the same sensitivity to Auger processes. The sensitivity can be relatively high for elements such as carbon, but lower for elements such as oxygen. The escape depth for Auger electrons is only several Ångströms, which is why it is considered a surface sensitive technique.

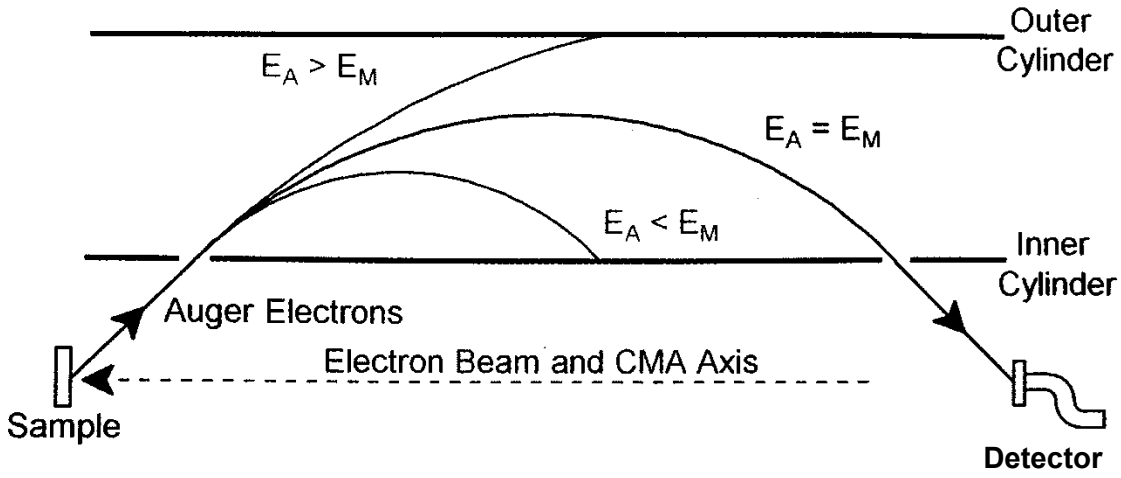

Fig. 4.9: Schematic diagram of the top half of a cylindrical mirror analyzer illustrating the energy selectivity of the analyzer.

The detection of Auger electrons in our instrument uses a cylindrical mirror analyzer (CMA) and a channel electron multiplier. The Auger spectrometer in our laboratory was produced by Omicron NanoTechnology GmbH[29], and contains a 5kV electron gun for primary excitation and a CMA 100 analyzer. A CMA consists of two concentric cylinders in which a negative potential difference is applied between the outer and inner cylinders. Auger electrons

[29] https://scientaomicron.com/en

collected by the CMA will be repelled by the negative potential on the outer cylinder. Electrons within the pass energy range will traverse a second aperture to the detector. The Auger spectra is created by increasing the pass energy and recording the detected current.

An Auger spectrum often plots the first derivative of the number of electrons detected versus the emitted electron kinetic energy. As mentioned, plotting the derivative of the current results in sharp, well-defined transitions which makes the identification of transitions easier. Figure 4.10 shows sample spectra plotted as electron count (or current) versus pass energy and the first derivative of the intensity versus pass energy.

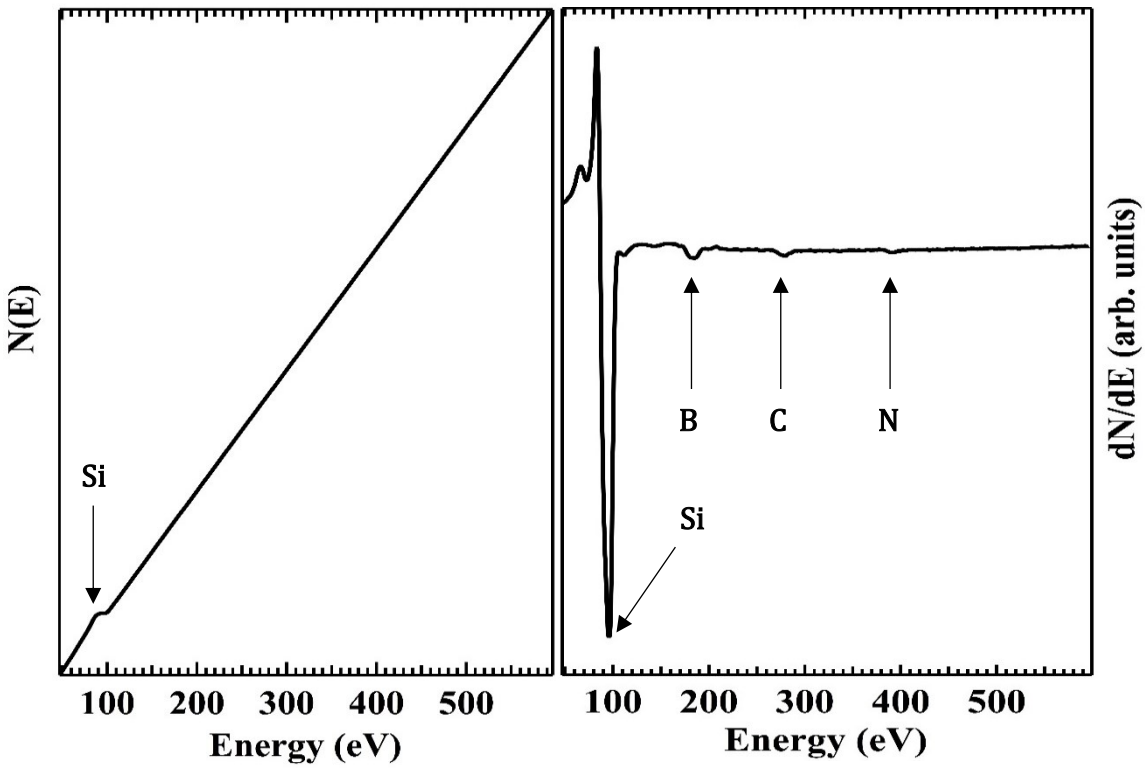

Fig. 4.10: Sample spectra for a silicon surface plotted in intensity and derivative modes. The intensity mode (left) shows hints only of a transition at 96eV. The derivative mode (right) is much more useful showing evidence of three elements on the surface – boron, carbon and nitrogen.

4.3.2 Low Energy Electron Diffraction

Low Energy Electron Diffraction (LEED) is a surface science technique used in our

laboratory and is one of the oldest modern surface science techniques. In fact, LEED provided the first experimental evidence of the wave nature of the electron in 1927. LEED provides information on the "translational symmetry" or periodicity of a surface structure through a direct visual display of the reciprocal lattice. That is, the points associated with the diffracted electron beams are characteristic of the reciprocal lattice. To define the reciprocal lattice, we quickly review the real space lattice and basis.

Crystal structure can be described in terms of a lattice with a group of atoms, or basis, attached to every lattice point. The lattice can be described by three fundamental translation vectors, $\mathbf{a_1}$, $\mathbf{a_2}$, $\mathbf{a_3}$, such that the atomic arrangement looks the same at a point $\mathbf{r}$ as it does from a point $\mathbf{r'} = \mathbf{r} + u_1\mathbf{a_1} + u_2\mathbf{a_2} + u_3\mathbf{a_3}$ where u_1, u_2, u_3 are arbitrary integers. The translation vectors of the reciprocal lattice are then defined by:

$$\mathbf{b}_1 = 2\pi \frac{\mathbf{a_2} \times \mathbf{a_3}}{\mathbf{a_1} \cdot \mathbf{a_2} \times \mathbf{a_3}} \quad \mathbf{b}_2 = 2\pi \frac{\mathbf{a_3} \times \mathbf{a_1}}{\mathbf{a_1} \cdot \mathbf{a_2} \times \mathbf{a_3}}$$
$$\mathbf{b_3} = 2\pi \frac{\mathbf{a_1} \times \mathbf{a_2}}{\mathbf{a_1} \cdot \mathbf{a_2} \times \mathbf{a_3}} \qquad (4.3.2.1)$$

The set of vectors, $\{\mathbf{G}\} = h\,\mathbf{b_1} + k\,\mathbf{b_2} + l\,\mathbf{b_3}$, where h, k, l are integers define the reciprocal lattice and determine the possible diffraction maxima in 3-D. More information can be found in Kittel (1996).

The phenomenon of LEED is founded on momentum conservation. The difference between the emerging and incident electron wavevectors must be equal to a reciprocal lattice vector:

$$\Delta\mathbf{k} = \mathbf{k}' - \mathbf{k} = \mathbf{G} \qquad (4.3.2.2)$$

This is a general restatement of the Bragg diffraction condition and a re-expression of the Laue condition. Because elastic scattering is required for diffraction, we have by conservation of

energy the further condition that:

$$|\mathbf{k}| = |\mathbf{k}'| \qquad (4.3.2.3)$$

LEED instruments use a retarding potential to filter the inelastically scattered electrons.

These diffraction conditions can be visualized using the geometric concept of the Ewald sphere. The Ewald sphere has a radius of k = k'. It is superimposed on the reciprocal lattice such that **k** terminates on a reciprocal lattice point and maintains the direction of the incident beam. If the surface of the sphere passes through any other reciprocal lattice points, then the diffraction condition is satisfied by the translational invariance of the reciprocal lattice. That is to say, any reciprocal lattice vector connecting the lattice point at the end of **k** to another reciprocal lattice point can be associated with a diffracted wavevector **k'** at some angle to **k**:

$$\mathbf{k}' = \mathbf{k} + \mathbf{G}. \qquad (4.3.2.4)$$

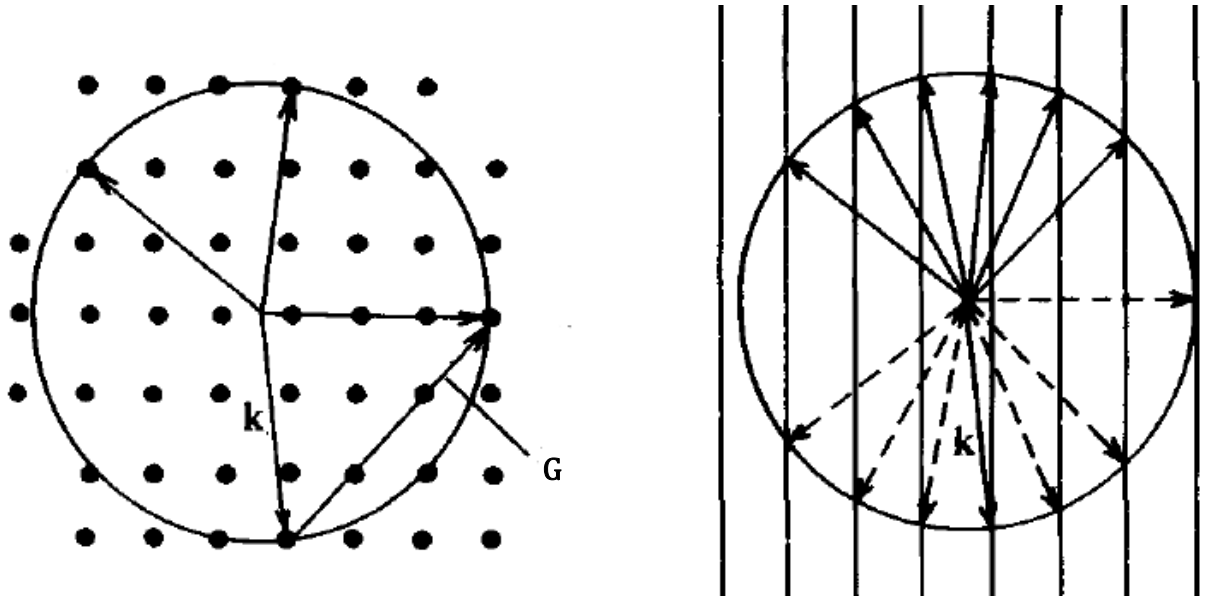

Fig. 4.11: Ewald sphere construction for bulk (left) and surface (right) cases. In the surface case, the dashed scattered wavevectors propagate into the solid and are not observed. (Woodruff & Delchar, 1994)[30]

[30] Reproduced with permission of Cambridge University Press through PLSclear. The copyright notice is available at https://gofile.io/d/1N3JaR .

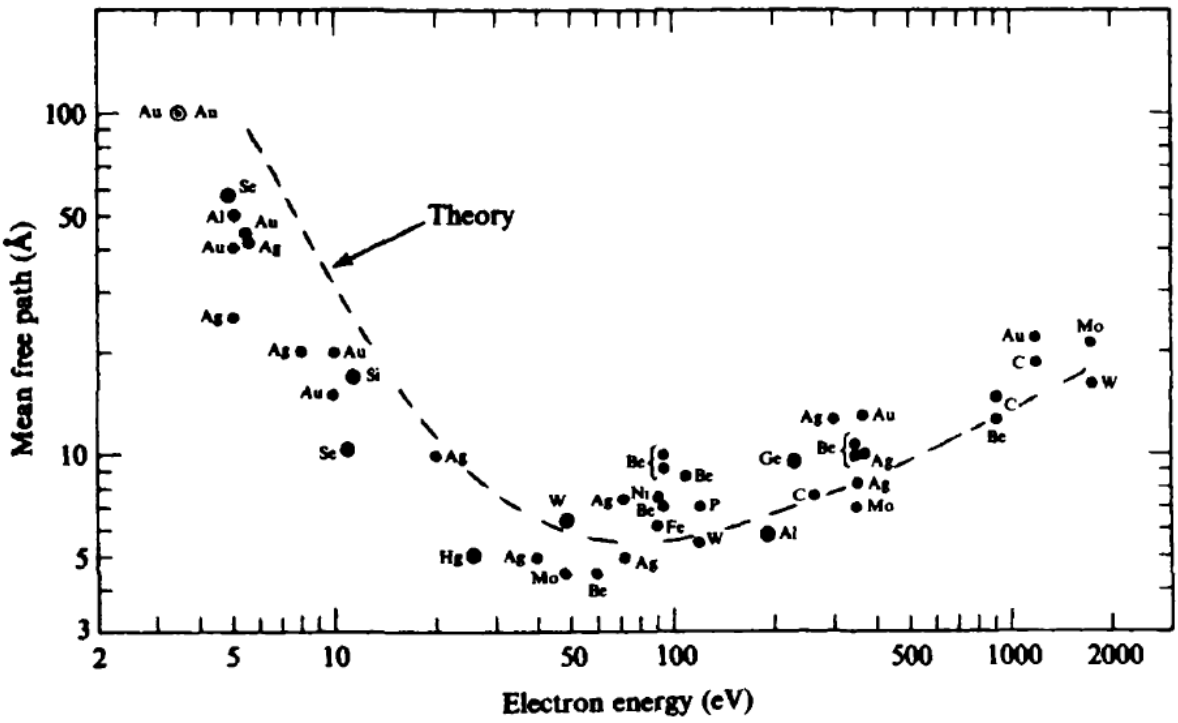

Fig. 4.12: Universal curve of electron mean free path in various solids. (Zangwill, 1988)[31]

The beauty of LEED is that the mean free path of (elastic) electrons from 10 – 150eV is quite low and element independent. The fact that the mean free path is small regardless of the energy allows the diffraction conditions to relax significantly. Since LEED mainly samples the surface of the crystal and not the bulk, the normal component of the incident wavevector becomes irrelevant. In real space, the electrons do not "see" past the first layer so perpendicular layers appear infinitely far apart. Accordingly, the reciprocal lattice points normal to the surface condense into "infinite lattice rods". In reality, there is some 3-D dependence on the diffraction pattern, but this effect is greatly reduced. If $k_{\parallel}$ represents the parallel and $k_{\perp}$ the perpendicular components of the electron waves, the diffraction conditions reduce to

[31] Reproduced with permission of Cambridge University Press through PLSclear. The copyright notice is available at https://gofile.io/d/1N3JaR .

$$\mathbf{k'}_{\parallel} = \mathbf{k}_{\parallel} + \mathbf{G_{hk}}$$

with $\mathbf{G_{hk}} = \mathrm{h}\,\mathbf{c_1} + \mathrm{k}\,\mathbf{c_2}$

where

$$\mathbf{c_1} = 2\pi \frac{\mathbf{a_2} \times \mathbf{n}}{\mathbf{a_1} \cdot \mathbf{a_2} \times \mathbf{n}} \qquad \mathbf{c_2} = 2\pi \frac{\mathbf{n} \times \mathbf{a_1}}{\mathbf{a_1} \cdot \mathbf{a_2} \times \mathbf{n}}$$

General examples of real space surface mesh and the corresponding LEED reciprocal space patterns are given in the figure 4.13 below. In this figure, $\mathbf{c_2}$ and $\mathbf{c_2}$ are called **a** and **b** respectively. In general, the quality of a surface can be qualitatively interpreted by evaluating the LEED pattern on the brightness and sharpness of the diffraction spots. A surface with a high number of defects will result in dim, broad diffraction spots. In highly contaminated or defective surfaces which reconstruct, the spots associated with the reconstruction spots may not be visible at all. Poor, sufficient, and high-quality silicon 7x7 reconstructions are shown in figure 4.14.

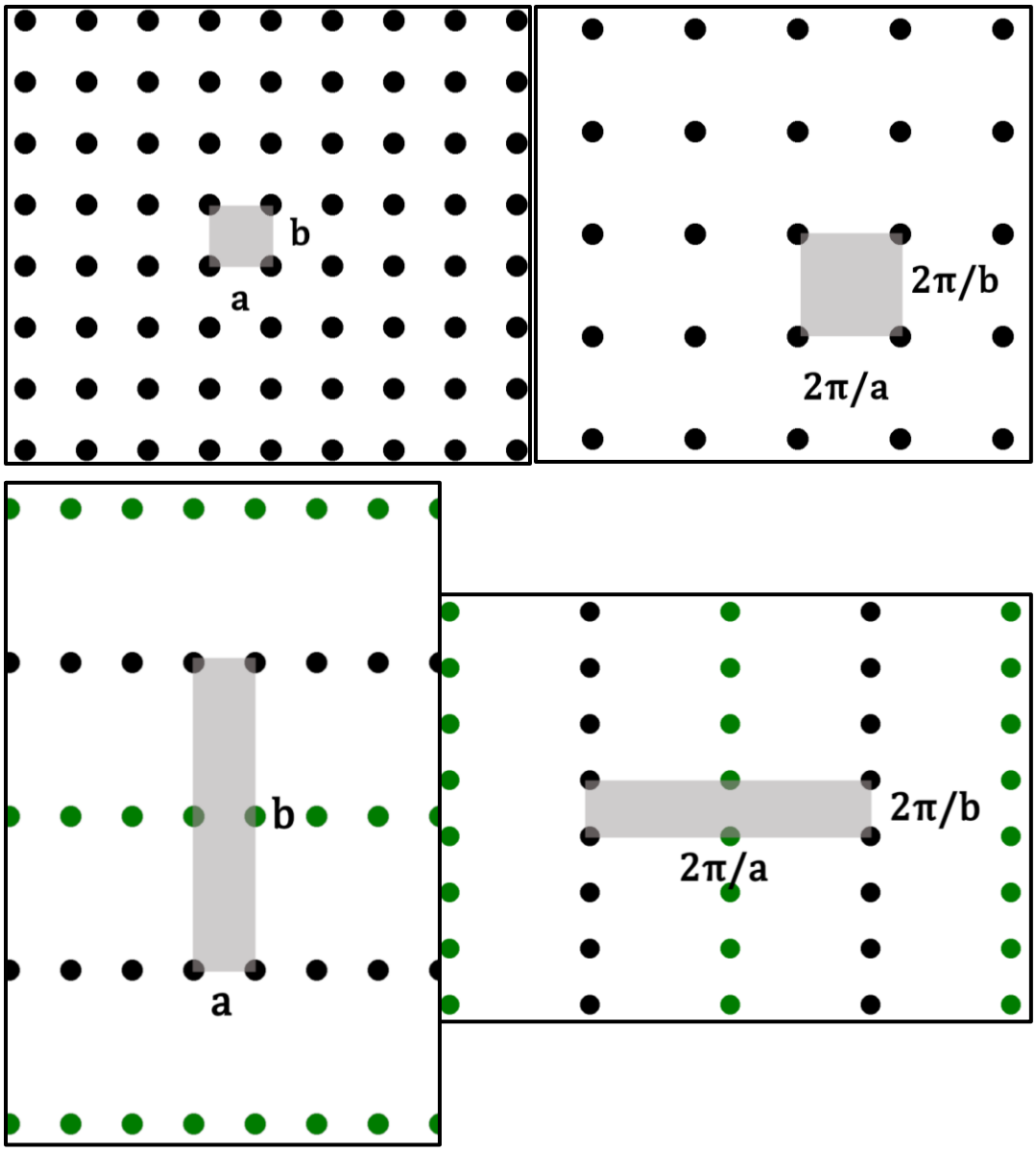

Fig. 4.13: Real space and reciprocal space schematics of two surfaces. Top: A simple square lattice. Black spots represent diffraction spots resulting from the substrate. Bottom: A rectangular lattice with additional green surface atoms. In both cases, the Laue condition is maintained: $\mathbf{a}_i \cdot \mathbf{c}_j = 2\pi\delta_{ij}$.

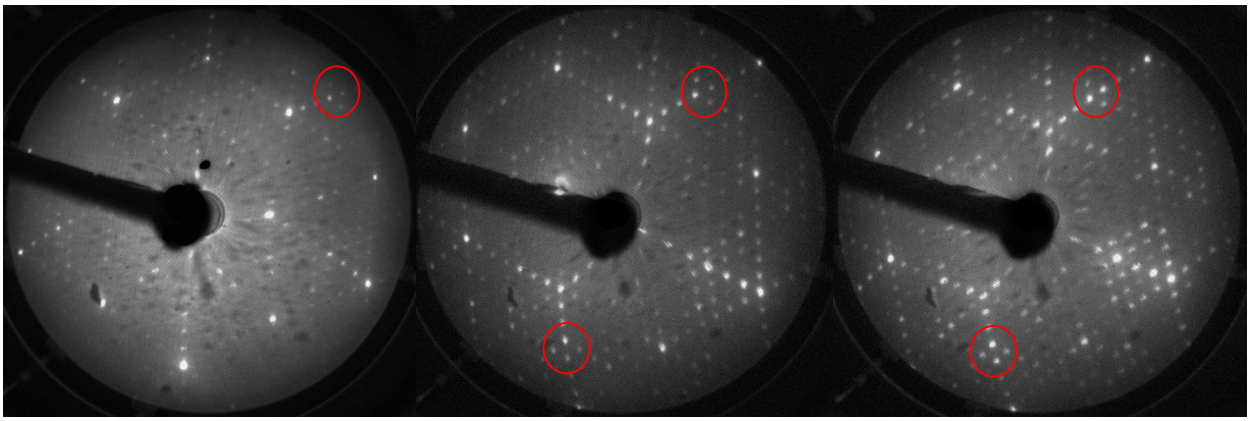

Fig. 4.14: LEED patterns of a 7x7 reconstructed silicon surface. LEED patterns of increasing quality are shown from left to right. The highlighted spots (red circles) are characteristic of highly periodic 7x7 surface. The amount of fine detail increases rightward, indicative of a pristine surface.

The LEED apparatus in our laboratory was manufactured by OCI Vacuum Microengineering[32], model LPS 075/300. The LEED screen is recorded with a model EDC-2000N CCD camera from Electrim Corporation[33]. Typically, these instruments include an electron gun, three or four hemispherical grids and a fluorescent phosphorous screen. The sample and first grid are both grounded to create a field free region for electrons to travel towards and away from the sample (Van Hove et al., 2012). A suitable negative potential is applied to the second and third grids to allow a narrow range of elastically scattered electrons to the fluorescent screen. Often, a fourth grid is present, which is also grounded, to prevent the suppressor grids from being affected by the screen voltage (Van Hove et al., 2012). The screen is biased to the order of kilovolts to render the diffraction pattern visible. The incoming electrons must have a high kinetic energy to activate the phosphor. The LEED optics in our laboratory are capable of delivering over a 4kV potential to the screen and can accelerate the electron beam to well over 100eV.

[32] www.ocivm.com/
[33] electrim.co.za/

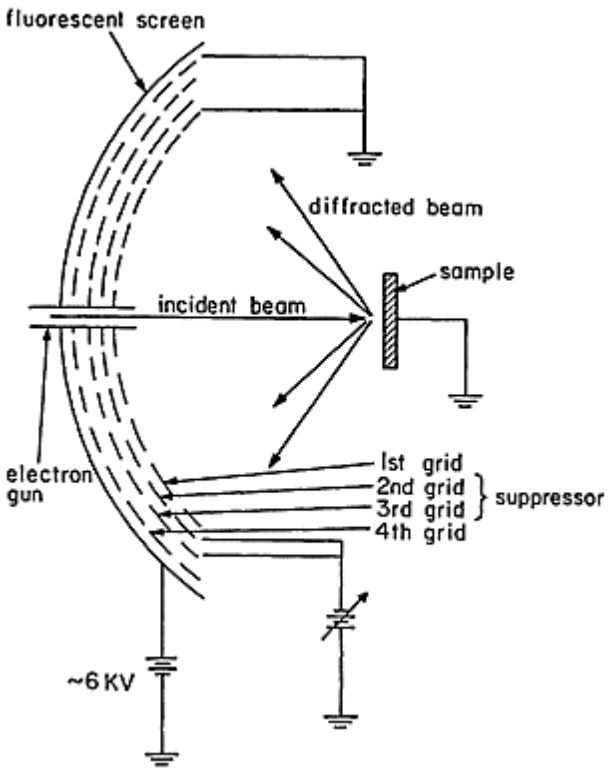

Fig. 4.15: Schematic diagram of a four grid LEED setup. (Van Hove et al., 2012)[34]

4.3.3 Scanning Tunnelling Microscopy

Without a doubt, the most important piece of equipment in our lab is the scanning tunnelling microscope. Our microscope was manufactured by Omicron[35] and is the Micro SPM model. It is controlled through RHK Technology[36] SPM 100 electronics and RHK software. There are several theoretical models of how a scanning tunnelling microscope operates with each model relying upon quantum tunnelling to a different level of rigor. The models we shall consider are the Bardeen approach and its extension, the Tersoff-Hamann method. The expanded method of Chen (1993) is left to the reader. We begin with a gross oversimplification of the potential energy barrier between tip and sample to a 1-D square

[34] Reprinted by permission from: **Springer-Verlag Berlin Heidelberg**, **Springer Series In Surface Sciences**, Low-Energy Electron Diffraction. Experiment, Theory and Surface Structure Determination by Van Hove et al, 2012, © **1986**

[35] https://scientaomicron.com/en

[36] https://www.rhk-tech.com/

barrier to illustrate the basis of scanning tunnelling microscopy (STM).

Classical mechanics tells us that an object moving under the influence of gravity, down a frictionless hill and up another can make it up to a height at most equivalent to where was released. In quantum mechanics, quantum tunnelling can occur, whereby very small particles with a kinetic energy less than the potential energy barrier can traverse said barrier. Another way this is often described is such that the particle "tunnels" through the barrier. Hence the name, quantum tunnelling. In STM, it is electrons which undergo quantum tunnelling.

A quantum mechanical treatment predicts an exponentially decaying solution for electrons with kinetic energy less than the potential energy of the 1-D square barrier. Consider an electron subject to the potential U(z) as in Fig. 4.16. Its wavefunction satisfies the Schrödinger equation

$$-\frac{\hbar}{2m}\frac{d^2}{dz^2}\psi(z) + U(z)\psi(z) = E\psi(z) \qquad (4.3.3.1)$$

at any given position. The potential of the barrier may not be constant in general. We take the barrier to be the physical vacuum between the substrate and the probe. Accordingly, the potential of the barrier, U_B, is the vacuum level. For states at the Fermi level, U_B-E is the work function, ϕ.

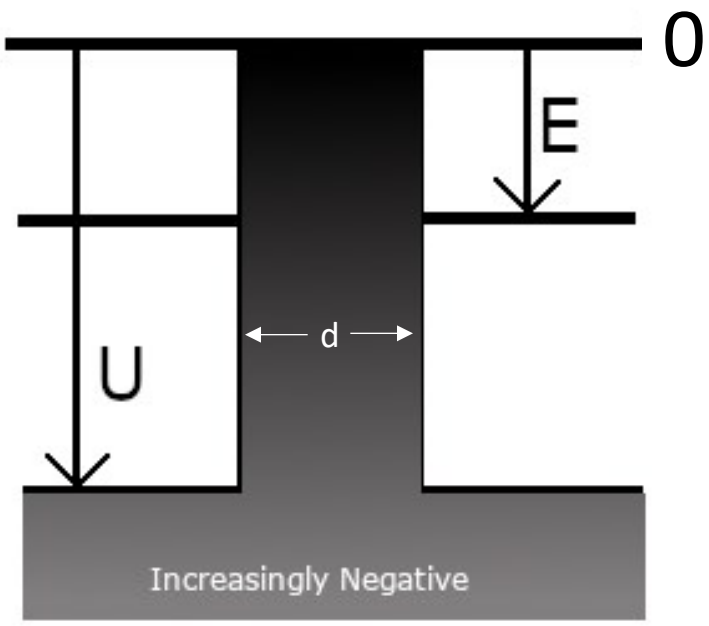

Fig. 4.16: A simple barrier as shown explains the physics of tunnelling. The barrier represents the physical vacuum between the substrate and tip. When the two are far apart, the wave functions of both decay into the vacuum or barrier region. Tunnelling can occur if the substrate and tip are close together. The potential energy outside the barrier is U, while inside the shaded barrier, the potential is $U_B = 0$. Particles incident on the barrier have an energy $E < 0$.

Inside the barrier, the wavefunction has a form $\psi(z) = C\, e^{-\kappa z} + D\, e^{\kappa z}$ where $\kappa = \sqrt{(-2mE)}/\hbar$, E is a negative value and the letters are constants. Outside the barrier, the form of the wavefunction is $\psi(z) = B\, e^{-ikz} + A\, e^{ikz}$ where $k = \sqrt{(2m(E-U))}/\hbar$ and U is the potential of either the sample or tip. Considering electrons incident from the left, the wavefunction simplifies to only a rightward travelling wave (positive exponential) on the righthand side of the barrier. Applying the boundary conditions of the wavefunction – continuous everywhere, continuous derivative everywhere – at both sides of the barrier gives the transmission coefficient, T.

$$T = \left[1 + \frac{1}{4}\left(\frac{\kappa}{k} + \frac{k}{\kappa}\right)^2 \sinh^2 \kappa d\right]^{-1} \qquad (4.3.3.2)$$

In the limit where κd is large, as is the case for a strongly attenuating barrier, the transmission

coefficient simplifies to

$$T \sim \frac{16\kappa^2 k^2}{(\kappa^2 + k^2)^2} \cdot e^{-2\kappa d} \qquad (4.3.3.3)$$

From this simple model, we begin to see the basis of STM, the transmission likelihood is exponentially dependent on the barrier width, d. Because we chose our barrier and zero of energy to be at the vacuum level, -E is equal to ϕ. Substituting a typical work function for a metal, ~5 eV, (Hölzl & Schulte, 1979), into κ for -E yields a transmission coefficient – or tunnelling current – that decreases by a factor of 10 for every 1 Å increase in barrier width. Even though this model is too simple to describe realistic STM experiments it explains the high sensitivity of the instrument to height changes in sample topography. It also demonstrates that atoms within the tip, even one atomic layer back from the apex, have a substantially reduced contribution to the tunnelling current.

Transfer Hamiltonian Approach

Bardeen (1961) developed a model for tunnelling in solids – the Bardeen or Transfer Hamiltonian Approach – for metal-oxide-metal junctions. The model can be applied to STM although it did not exist at the time. Here we will refer to the electrodes Bardeen originally studied as tip and sample to clarify the discussion. Bardeen separated the tip-vacuum-sample system into two independent subsystems (tip-barrier and sample-barrier). A separation surface, ($S_{Tip/Sample}$), divides the subsystems. The potential of the complete system is the total of the individual subsystems; the potential of the subsystems is zero after crossing the separation surface (Stroscio, 1993). To consider tunnelling from tip to sample, the presence of tip is the perturbation to the sample. While the model may resemble ordinary first-order perturbation theory, it is formally different in that the eigenstates are from different Hamiltonians and are non-orthogonal.

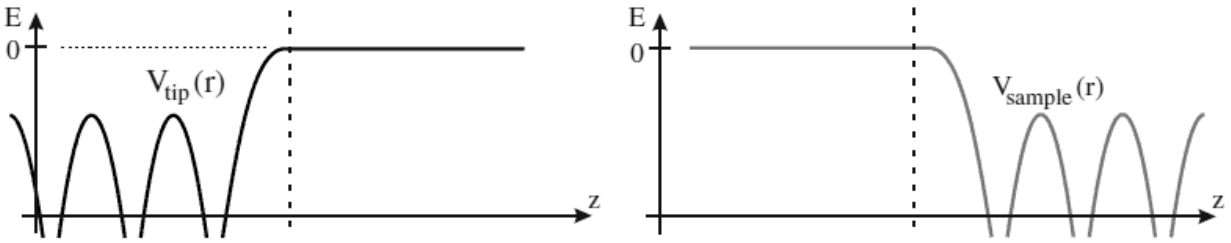

Fig. 4.17: Perturbation theory potentials for the tip and sample subsystems. The vertical dashed line represents the separation surface.

If we consider a tunnelling event from an initial state i to a final state f, the wavefunction for the electron in the combined system is

$$\Psi_{Total}(\boldsymbol{r},t) \;=\; \Psi_{Tip,i}(\boldsymbol{r},t) \;+\; \sum_{j} a_j(t)\Psi_{Sample,j}(\boldsymbol{r},t) \tag{4.3.3.4}$$

with the time-dependent subsystem solutions written in the usual way

$$\Psi_{i/j}(\mathbf{r},\mathrm{t}) \;=\; \psi_{\mathrm{i/j}}(\mathbf{r})\mathrm{e}^{-\mathrm{iE_{i/j}t}/\hbar}\,. \tag{4.3.3.5}$$

The coefficient a_j is the probability amplitude for a given sample state. All a_j are zero at time $t_0 = 0$ and are small for small times. After much rearrangement, direct substitution of the total wavefunction into the time-dependent Schrödinger equation gives

$$\begin{aligned} \mathrm{i}\hbar\sum_{j}\frac{da_j(t)}{dt}\,\psi_{Sample,j}(\mathbf{r})\mathrm{e}^{-\mathrm{iE_j t}/\hbar} \;=\; & \mathrm{U}_{Sample}(\mathbf{r})\,\psi_{\mathrm{Tip,i}}(\mathbf{r})\mathrm{e}^{-\mathrm{iE_i t}/\hbar} \\ & + U_{Tip}(\boldsymbol{r})\sum_{\mathrm{j}} a_j(t)\,\psi_{Sample,j}(\mathbf{r})\mathrm{e}^{-\mathrm{iE_j t}/\hbar}\,. \end{aligned} \tag{4.3.3.6}$$

Provided the wavefunctions between sample and tip are approximately orthonormal, the sums in Equation 4.3.3.6 can be reduced by taking the inner product with the f^{th} stationary sample state, $\psi_{\mathrm{Sample,f}}$:

$$\begin{aligned} i\hbar\frac{da_f(t)}{dt}\,\mathrm{e}^{-\mathrm{iE}_f\mathrm{t}/\hbar} \;=\; & \int \psi^{*}_{Sample,f}(\boldsymbol{r})\,\mathrm{U}_{Sample}(\mathbf{r})\,\psi_{\mathrm{Tip,i}}(\mathbf{r})\mathrm{e}^{-\mathrm{iE_i t}/\hbar}\,dV \\ & + U_{Tip}(\boldsymbol{r})\mathrm{a}_f(\mathrm{t})\mathrm{e}^{-\mathrm{iE}_f\mathrm{t}/\hbar}\,. \end{aligned} \tag{4.3.3.7}$$

The last term on the right-hand side of Equation 4.3.3.7 can be neglected since the a_j are small for the small time regime. The result becomes

$$a_f(t) = \frac{1}{i\hbar}\int \psi^*_{Sample,f}(\boldsymbol{r})\, \mathrm{U}_{Sample}(\mathbf{r})\, \psi_{\mathrm{Tip,i}}(\mathbf{r})\mathrm{dV} \int_0^t \mathrm{e}^{-\mathrm{i}(\mathrm{E_i}-\mathrm{E}_f)\mathrm{t}/\hbar}\, dt' \qquad (4.3.3.8)$$

with the volume integral defining the matrix element M_{fi}. After evaluating the time integral and taking the modulus square of a_f, we obtain the probability of finding an electron in sample state j which was originally in tip state i as

$$\left|a_f(t)\right|^2 = \frac{2\pi}{\hbar}\left|M_{fi}\right|^2 \delta(E_{Sample,f} - E_{Tip,i}) \qquad (4.3.3.9)$$

where the identity $\delta(x) = \lim_{a\to\infty} \frac{1}{\pi}\frac{\sin^2 ax}{ax^2}$ has been used. In the limit of large time, $|a_f(t)|^2$ becomes the transition rate from tip to sample:

$$\omega_{Tip,i\,\rightarrow\, Sample,f} = \frac{2\pi}{\hbar}\left|M_{fi}\right|^2 \delta(E_{Sample,f} - E_{Tip,i}) \qquad (4.3.3.10)$$

Equation 4.3.3.10 is Bardeen's *twist* on Fermi's Golden Rule. The transition rate is proportional to the matrix element. The Dirac delta in Equation 4.3.3.10 shows that the energy of the final state must be the same as the initial state. Evaluation of the matrix element (the volume integral in Equation 4.3.3.8) is made more tenable by the subsystem condition imposed by Bardeen. The integral over all space can be reduced to the sample space only because the sample potential is zero in the tip region. Likewise, the tip potential is zero in the sample space, further simplifying the calculation. Bardeen (1961) then leverages Green's second identity to produce the matrix elements which depend only on the sample and tip wavefunction at the separation surface. The matrix element M_{fi} becomes:

$$M_{\mathrm{fi}} = \frac{\hbar^2}{2m} \int_{S_{Tip/Sample}} \left[\psi_{tip,i}(\boldsymbol{r})\boldsymbol{\nabla}\psi^*_{sample,f}(\boldsymbol{r}) - \psi^*_{sample,f}(\boldsymbol{r})\boldsymbol{\nabla}\psi_{tip,i}(\boldsymbol{r})\right] \cdot d\boldsymbol{S} \quad (4.3.3.11)$$

The calculation of the matrix element M_{fi} involves an integration over an arbitrary tip-sample separation surface $S_{Tip/Sample}$. To obtain the total transition rate from any initial state to any final state requires a summation over all pairs of states

$$\omega_{\mathrm{tip}\,\rightarrow\,\mathrm{sample}} = \frac{2\pi}{\hbar}\sum_{i,f}\left|\mathrm{M_{fi}}\right|^2 \delta(\mathrm{E_f} - \mathrm{E_i})\,. \quad (4.3.3.12)$$

This gives the Bardeen equation for the tunnelling current as

$$I = \frac{4\pi\mathrm{e}}{\hbar}\sum_{i,f}\left|\mathrm{M_{fi}}\right|^2 \delta(\mathrm{E_f} - \mathrm{E_i}) \quad (4.3.3.13)$$

where the original work assumes step functions for the state occupation. Advanced texts will give this equation as $\mathrm{I} = \frac{4\pi\mathrm{e}}{\hbar}\sum_{\mathrm{i,f}}\left\{\mathrm{f(E} - \mathrm{E_{Fermi,Tip}}) - \mathrm{f(E} - \mathrm{E_{Fermi,Sample}})\right\}\left|\mathrm{M_{fi}}\right|^2 \delta(\mathrm{E_f} - \mathrm{E_i})$ where f(E) represents the Fermi distribution function at energy E (Stroscio & Kaiser, 1993). The Bardeen equation for the tunnelling current above can be evaluated further. It can be modified to focus on the energy dependence of the density of states of the tip and sample. According to Voigtländer, (2015) the result is:

$$I = \frac{4\pi\mathrm{e}}{\hbar}\int_{E_{Fermi,Sample}}^{E_{Fermi,Tip}} n_{tip}(\varepsilon)n_{sample}(\varepsilon)|M(\varepsilon)|^2\, d\varepsilon \quad (4.3.3.14)$$

with

$$\mathrm{M}(\varepsilon) = \frac{\hbar^2}{2m}\int_{S_{tip/sample}} \left[\psi_{tip}(\boldsymbol{r},\varepsilon)\boldsymbol{\nabla}\psi^*_{sample}(\boldsymbol{r},\varepsilon) - \psi^*_{sample}(\boldsymbol{r},\varepsilon)\boldsymbol{\nabla}\psi_{tip}(\boldsymbol{r},\varepsilon)\right] \cdot d\boldsymbol{S} \quad (4.3.3.15)$$

and $\mathrm{n}(\varepsilon)$ the density of states. Equations 4.3.3.13 and 4.3.3.14 assume a step function of states at the Fermi level. For non-zero temperatures, the "{window function}" must be included. The

result for the current becomes

$$I = \frac{4\pi e}{\hbar} \int_{-\infty}^{\infty} \{f(\varepsilon - E_{Fermi,Tip}) - f(\varepsilon - E_{Fermi,Sample})\} n_{tip}(\varepsilon) n_{sample}(\varepsilon) |M(\varepsilon)|^2 \, d\varepsilon \,. \quad (4.3.3.16)$$

While the density of states modification is an important model to demonstrate the topological map produced by scanning tunnelling microscopy, using it in practice requires the density of states of the tip. Data regarding the tip, such as its wavefunction or density of states is almost certainly unknown in STM. This is the main weakness of the Transfer-Hamiltonian Approach. The Tersoff-Hamann approximation to the Bardeen Approach does not require strict knowledge about the tip.

Tersoff-Hamann (S-Wave) Approximation

Many consider the Tersoff-Hamann approximation the *de facto* explanation of tunnelling for the purposes of STM. The Tersoff-Hamann explanation of STM approximates the tip wavefunction by a $l = 0$ spherical harmonic, i.e. an s-orbital wavefunction. In addition, the energy dependence of the matrix elements (Equation 4.3.3.15) is neglected and tunnelling is considered only near the Fermi level, in the limit where the bias is small. This greatly reduces the challenge of evaluating the matrix elements in the Bardeen theory of tunnelling. Tersoff and Hamann (1985), evaluated Equation 4.3.3.15 using a plane wave Fourier expansion to describe the wavefunction of the surface. They found the tunnelling current is proportional to the local density of states of the sample at energy E_F at the center of the s-wave, $\mathbf{r}_t$.

$$I \propto \sum_m |\psi_m(\boldsymbol{r}_t)|^2 \, \delta(E_{F,Sample} - E_m) \equiv n_{Sample}(E_{F,Sample}, \boldsymbol{r}_t) \quad (4.3.3.17)$$

ψ_m are the surface wavefunctions and the absolute square is the probability of finding a surface state electron at the position of the tip. An ideal Tersoff-Hamann scanning tunnelling

microscope – where the tip can be modelled as an s-wave – therefore measures the local density of states of the surface without reference to the tip-sample system. More information on the Tersoff-Hamann approximation or generalized tip wavefunctions can be found in Chen's research papers (1990a, 1990b), or his book (1993).

4.3.4 STM Design Considerations

Scanning tunnelling microscopes must raster the tip at a fixed bias across the sample in order to acquire a topographic image of a constant local density of states. In addition, the tip of the microscope must maintain an Ångström order distance from the sample. To maintain such precise distances, scanning tunnelling microscopes utilize piezoelectric crystals. Piezoelectric crystals can develop a potential difference in response to mechanical stress, or conversely, they can deform mechanically due to an applied voltage difference.

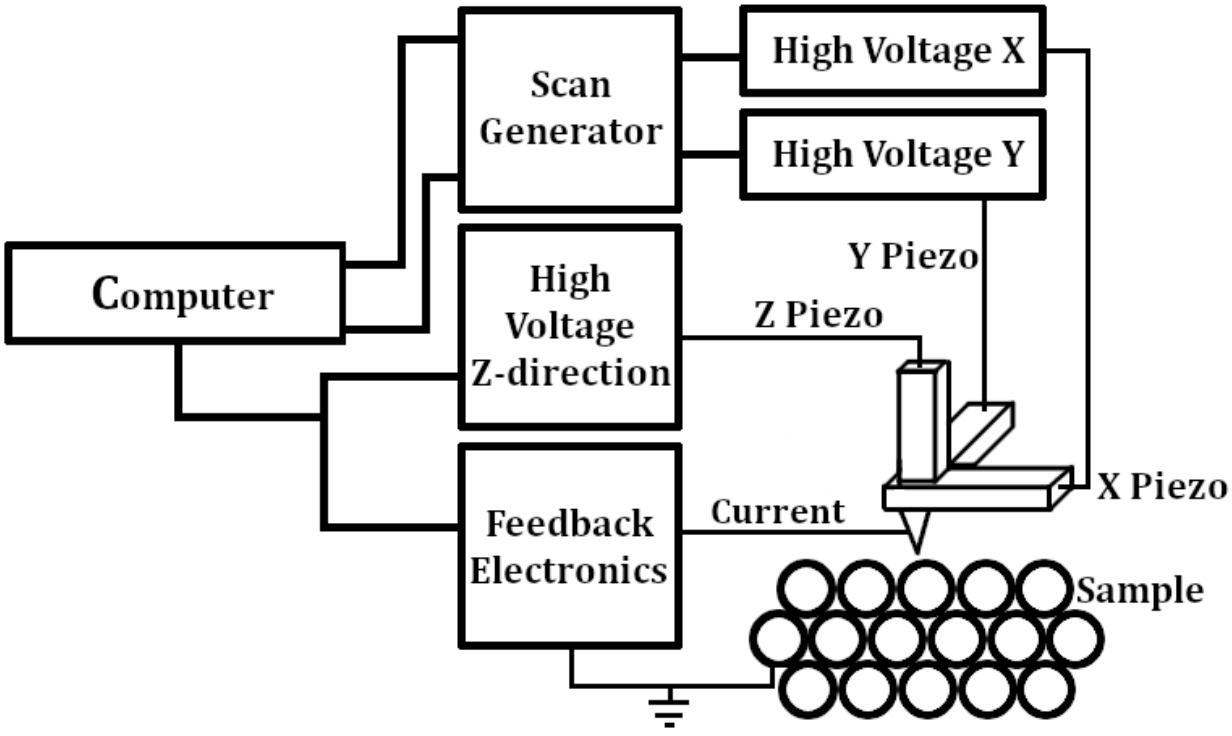

Fig. 4.18: A schematic diagram of a STM system showing the feedback electronics and piezoelectric crystals as blocks. Not to scale. Figure based upon Woodruff & Delchar, (1994)

Our microscope operates in constant current mode, with a xy- and z-sensitivities of 51 nm/V and 5nm/V respectively. There are several styles of piezo arrangements. Our machine uses a tube style with electrodes on the inner and outer walls of an open cylinder. The outer tube electrode is divided in four quadrants, $\pm$x and $\pm$y. A voltage difference between the inner and outer electrodes induces a uniform extension or contraction in z and a differential bias between outer electrode regions induces a bend. The change in the z-direction associated with the bend is neglected, reducing it to a planar deflection for small area scans.

To monitor tip-sample separation, a feedback loop monitors the tunnelling current and adjusts the voltage of the z-piezo to alter the tip-sample separation distance and maintain a constant current. This is known as the constant current mode of operation. STM can also operate in constant height mode, where the current varies freely due to a very slow feedback response.

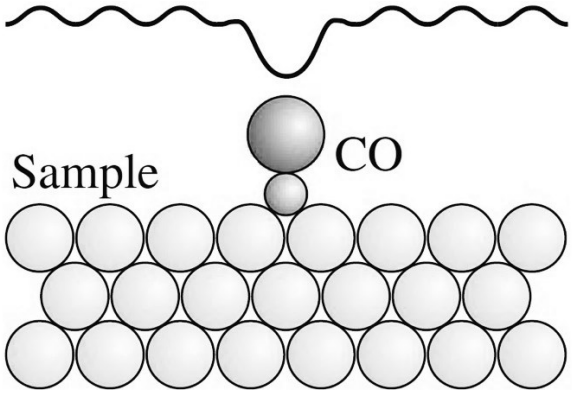

Fig. 4.19: The black line illustrates the topography if this surface was scanned in STM. Although the CO molecule is a physical protrusion on the surface, the tip sees a decrease in current since the density of states is lower due to the CO molecule[37].

[37] Reprinted by permission from: **Springer-Verlag Berlin Heidelberg**, **NanoScience and Technology**, (Scanning Probe Microscopy - Atomic Force Microscopy and Scanning Tunneling Microscopy by Voigtlaender, 2015), © **2015**

Tip sharpness is paramount in STM, as the tip sharpness is the major factor in microscope resolution. Tips are made in a simple electrochemical etching procedure. Over the course of this thesis, many variations of tip etching techniques were executed but the long turn around time made quantifying the quality of one particular method difficult. Textbooks such as Woodruff & Delchar (1994) or Voigtländer (2015) claim that without post-etching modification, the sharpest tips result from random asperities when the tip fractures.

The basic idea is to dip a small diameter metal wire into an electrolyte solution in which a counter electrode is sitting and to apply a DC voltage between these two electrodes until enough of the positively biased wire has been etched away so that part of the wire becomes so thin its tensile strength cannot sustain the weight of the lower end of the wire. The latter breaks off and a tip shaped like Toricelli's trumpet is left behind. We use a 2 M sodium hydroxide solution and several volts to etch a tungsten tip. The counter electrode is also tungsten. The overall reaction governing the electrochemical etching is the following (Ibe et al., 1990):

cathode: $6\ H_2O + 6\ e^- \rightarrow 3\ H_2(g) + 6\ OH^-$

anode: $W(s) + 8\ OH^- \rightarrow WO_4^{2-} + 4\ H_2O + 6e$

$$W(s) + 2\ OH^- + 2\ H_2O \rightarrow WO_4^{2-} + 3\ H_2(g)$$

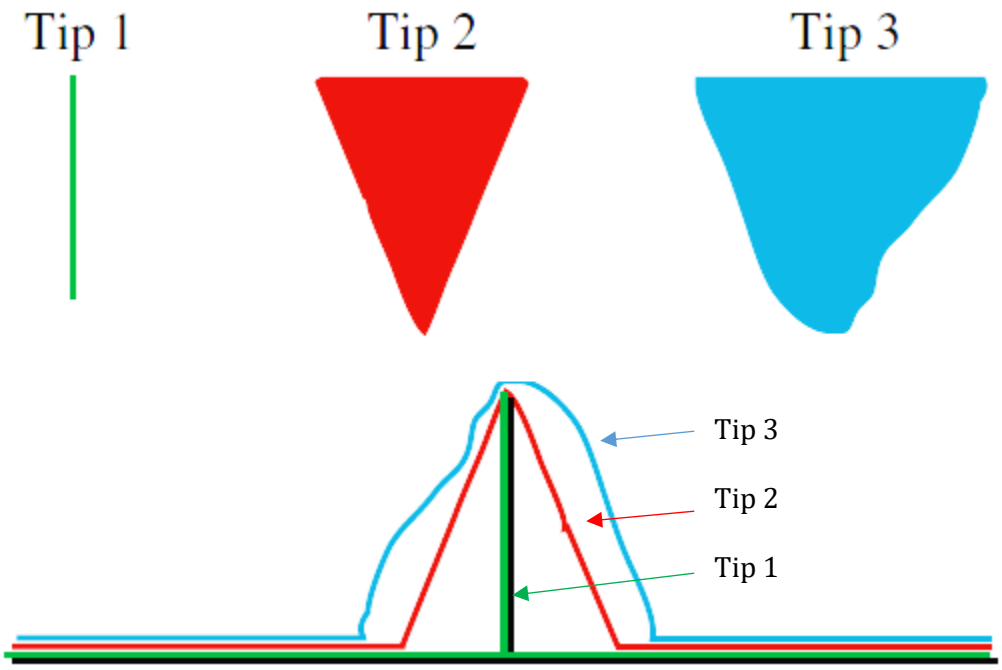

Fig. 4.20: Schematic diagram illustrating the importance of a sharp tip in STM. A conceptual sample surface is given in black as a delta function. The resultant surface topography of three different tips is overlaid upon the proposed sample surface. A blunt tip will resolve the delta function as a mirror of itself. As well, blunt tips will not be able to resolve small structures which are sandwiched between large structures. (Voigtländer, 2015)[38]

An automated tip etching system was used for making tips in our lab. The system automatically stops when the positive tungsten anode fractures to ensure the apex is not etched dull. The circuit supplies current via the electrodes in a sodium hydroxide solution. The same current flows through a LM311 comparator as part of the etching circuit. The comparator compares the current with a preset threshold (typically 5 mA). When the current falls below the threshold, the comparator switches state and removes the gate bias to an IRF520 M16 MOSFET, the MOSFET then switches off and the circuit path for etching is interrupted.

More important than the tip etching mechanism, is the ability to sharpen tips in situ.

[38] Reprinted by permission from: **Springer-Verlag Berlin Heidelberg**, **NanoScience and Technology**, (Scanning Probe Microscopy - Atomic Force Microscopy and Scanning Tunneling Microscopy by Voigtlaender, 2015), © **2015**

Our laboratory uses a high DC voltage to ionize the oxide layer on our tip. Removal of the oxide layer is important because oxides are insulating. A heavily oxidized tip could be in contact with the sample and still not be able to tunnel.

To bring the tip of our scanning tunnelling microscope into tunnelling range we use a motorized coarse approach plus a computerized inertial approach. The inertial approach can be called a "stick-slip" or "inertial slider" approach. In this method, a voltage is applied to the z-piezo and is slowly increased to maximum extension. Meanwhile, the feedback system is checking for a tunnelling current. If no current is detected, the computer retracts the piezo fully and an actuator takes a step towards the sample which is slightly smaller than the range of the z-piezo. This process is repeated until a tunnelling current is detected.

The operation of any scanning tunnelling microscope is very sensitive to building vibrations. Scanning tunnelling microscopes must employ some fashion of vibration isolation. Set-ups may include stacks of metal-Viton® disks or bungee-cords suspension to dampen vibrations. More intricate isolation systems such as pneumatic or eddy-current dampening legs exist.

Our scanning tunnelling microscope is elevated by a Newport[39] vibration isolation system. It consists of four legs each with an air piston to dampen vibrations of the system. Three of the four legs have leveling valves accurate to within 1mm. The air pistons are fed by a tank of compressed nitrogen and are regulated to 80 lbs/in^2.

4.4 Density Functional Theory Calculations

Density functional theory (DFT) is a method of obtaining an approximate solution to

[39] https://www.newport.com/g/products

the Schrödinger equation of a many body system. A functional refers to a function which intakes another function. In DFT, the electron density is the key function. The electron density is a function of space and time. All of the ground state properties of a system are derived from the electron density function. This makes the system a functional of the electron density – hence the name.

The calculations in this thesis were performed using Gaussian 16 software (Frisch et al., 2016) through the Compute Canada Database. All calculations were done in the gas phase without the influence of a substrate. Calculations used the B3LYP functional exclusively (Becke, 1988; Becke, 1993; Lee, Yang & Parr, 1988) and a 6-31G(d,p) basis (Ditchfield, Hehre & People, 1971; Hehre, Ditchfield & People 1972; Harihan & People, 1973; Rassolov et al., 1998). The 6-31G(d,p) basis was used exclusively unless otherwise stated. The sole exception pertains to calculations for the Ag(111) surface. Results on the Ag(111) surface are compared to density functional calculations using a dual basis set to model the silver atom separately from the organic atoms. The DFT calculations were performed using the usual 6-31G(d,p) basis set for the main atoms, (H, C, N, O), in conjunction with the Los Alamos National Laboratory 2 Double-Zeta (LANL2DZ) basis set for silver atoms (Hay, & Wadt, 1985). Both of these basis sets have been widely used in density functional methods for studies of systems containing transition metals and a mixed basis set approach is popular to preserve accuracy and minimize computational expense (Yang, Weaver & Merz, 2009). The inner electrons of the silver atoms are modelled by an effective core potential.

A substrate was not included in the calculations as including a substrate significantly raises the complexity of the calculation. This approximation is justified as intermolecular forces typically dominate the ordering of molecules on surfaces. Significant molecule-surface

interactions which bind the molecules to the surface do exist. However, surface interactions can be neglected when considering how molecules arrange themselves on a surface as they usually pale in comparison to intermolecular forces.

5. Results

The results section is broken into three categories, one for each of the surfaces studied – Si(111)-√3x√3-R30°-B, Ag(111) and Au(111) thin films. Each section is further divided into substrate preparation, and molecular deposition at various parameters. Major findings are compared with density functional theory calculations and are also given in the context of similar research by others.

5.1 Si(111)-√3x√3-R30°-B

5.1.1 Substrate Preparation

Several variations on resistance-based heating were used to prepare the Si-B surface from doped wafers. Two sets of boron doped wafers were purchased from Sil'tronix[40]. They had a resistivity of either 0.002 Ω·cm or 0.001 $\pm$ 0.0002 Ω·cm. The wafers with the lower resistivity were purchased to determine if a higher boron concentration would lead to a high-quality √3 surface without contaminating the surface during the annealing process. Various methods were used in attempt to create the Si-B surface.

Many of the methods share the same general approach. Our silicon samples are degassed overnight at 690°C. The temperature is measured by an infrared pyrometer with the emissivity set to 0.4 . A computer program is used to rapidly adjust the current supplied to the wafer. Temperatures are manipulated by adjusting the supplied current.

After the extended degas, a specific temperatures sequence (or the corresponding currents) was sought. Typically, two currents corresponding to particular temperature regimes were used to prepare the samples. The hotter of the two temperatures, near 1200°C,

[40] https://www.sil-tronix-st.com/en/home

was used to remove carbon from the surface (Lin et al., 1998). The lower temperature, often around 950°C, was used to allow for boron from the bulk to migrate to the surface (Headrick et al., 1989; Yates, 1991). Samples were flashed several times for approximately 8 seconds and then rapidly cooled to between 800°C – 1000°C for anywhere between 3 minutes to 200 minutes. The various methods used to create the reconstruction are differentiated by several factors and are explained below.

5.1.2 Annealing Studies

We attempted various methods to create the Si-B reconstruction. Several factors differentiate the various attempts. The factors distinguishing the different approaches to create the Si(111)-$\sqrt{3}$x$\sqrt{3}$-R30°-B reconstruction include the number of times the wafers were flashed, the anneal time and the annealing temperature. In addition, ex-situ treatment of wafers with organic solvents or cleaners and a cyclical flash-anneal process are considered distinguishing factors. The various factors were used in combination to adapt processes used by others, (Andrade et al., 2015; Baris et al., 2020; Copie et al., 2014; Eom, Moon & Koo, 2015; Lindner et al., 2019; Spadafora et al., 2014; Wagner & Zhang, 2014), in an attempt to create our own optimized procedure. None of the methods attempted produced a pristine Si-$\sqrt{3}$x$\sqrt{3}$-B reconstruction. Flashing the wafer to temperatures >1200°C and then holding it at 930°C for 100 minutes produced the best results (Section 5.1.2 Figure 5.10).

Given below are select examples of various preparation procedures used for the highly doped wafers ($\rho = 0.001 \pm 0.0002$ Ω·cm). The focus is given to the wafers with lower resistivity because they produced superior LEED and AES results in all instances where the same preparation method was applied to both the higher and lower-doped wafers. The AES and LEED results associated with a simple flashing to 1200°C can be seen below in figure 5.1.

Although the wafers appeared free from contamination, there was a plethora of dangling bonds as revealed by STM (figure 5.2). In contrast, annealing a wafer at 820°C for 30 minutes

Research Group	Si-B Preparation Procedure	Wafer Resistivity [Ω·cm]

Andrade et al., 2015	• Degas for 48 hr; 500°C – 600°C
	• 5 – 10 cycles:
	  ○ Flash to 1200°C; hold 10s – 15s
	  ○ Rapidly cool to 800°C
	  ○ Slowly cool to ambient
		< 0.001

Baris et al., 2020	• Multiple flashes ≲1200°C. • Anneal 1hr; 800°C	0.001 [41]
Copie et al., 2014	• Anneal few hours; > 900°C	'High Quality'
Eom, Moon & Koo, 2015	• Repeated flashes 1473°C • Following final cycle, cool to ambient at 2°C/s	< 0.001
Lindner et al., 2019	• Repeated Anneal 1200°C • Anneal ½ hr; 900°C	< 0.002

Spadafora et al., 2014	• Degas for 12 hr; 550°C
	• ≥ 5 Cycles:
	  ○ Flash to 1200°C; hold 10s;
	  ○ Rapidly cool to 800°C
	• Following final cycle, cool to ambient at 10°C/s
		< 0.001

Wagner & Zhang, 2014	• Ex situ cleaning via standard RCA1 & RCA2 etch • Flash to 1200°C • Anneal extended periods; 800°C	'Heavily Doped'

Table 5.1: A summary of the various preparation procedures used to prepare the Si-√3x√3-B reconstruction from different research groups. The resistivity of the wafer used is also given.

produced a strong √3x√3 diffraction pattern. Unfortunately, STM revealed the surface again possessed a large number of dangling bonds, (figures 5.3 and 5.4). Improvements to surface quality were made by annealing wafers for 1 hour between 800°C and 900°C following a 1200°C flash. The LEED and AES spectra of these wafers were promising (figure 5.5) although,

[41] This value may not be correct as authors report resistivity in units of W·cm

the presence of dangling bonds could not be totally eliminated using this approach (figure 5.6).

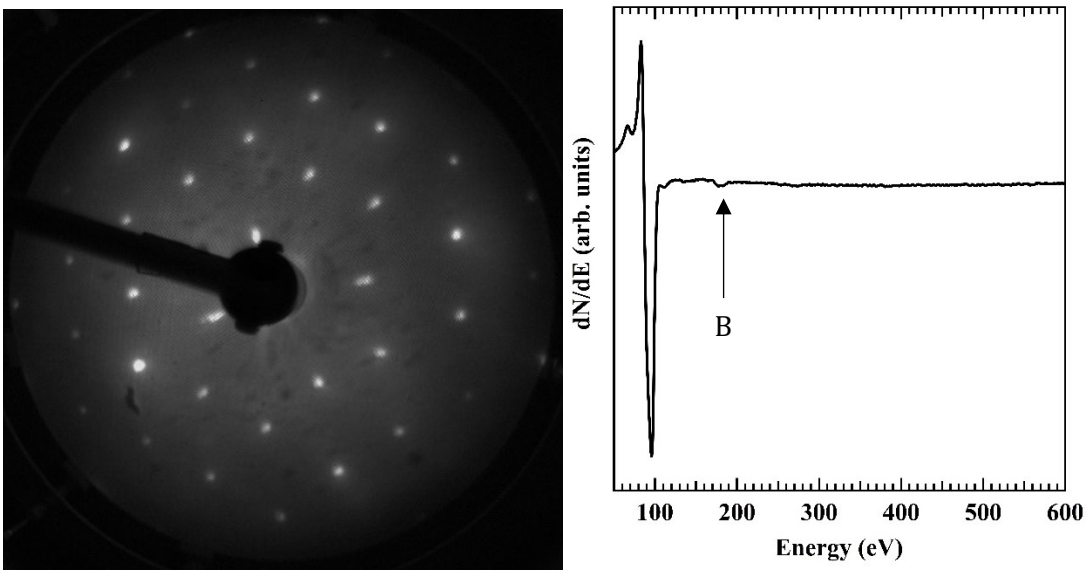

Fig. 5.1: LEED and AES spectra of a highly doped Si wafer revealing a contamination free surface after simple flashing. The dim and fuzzy diffraction spots are indicative of a weak $\sqrt{3}x\sqrt{3}$ reconstruction. The AES spectra shows the main silicon MNN transition at 96eV, and a much weaker A KLL boron transition is shown at 180eV. LEED Beam Energy, 75eV

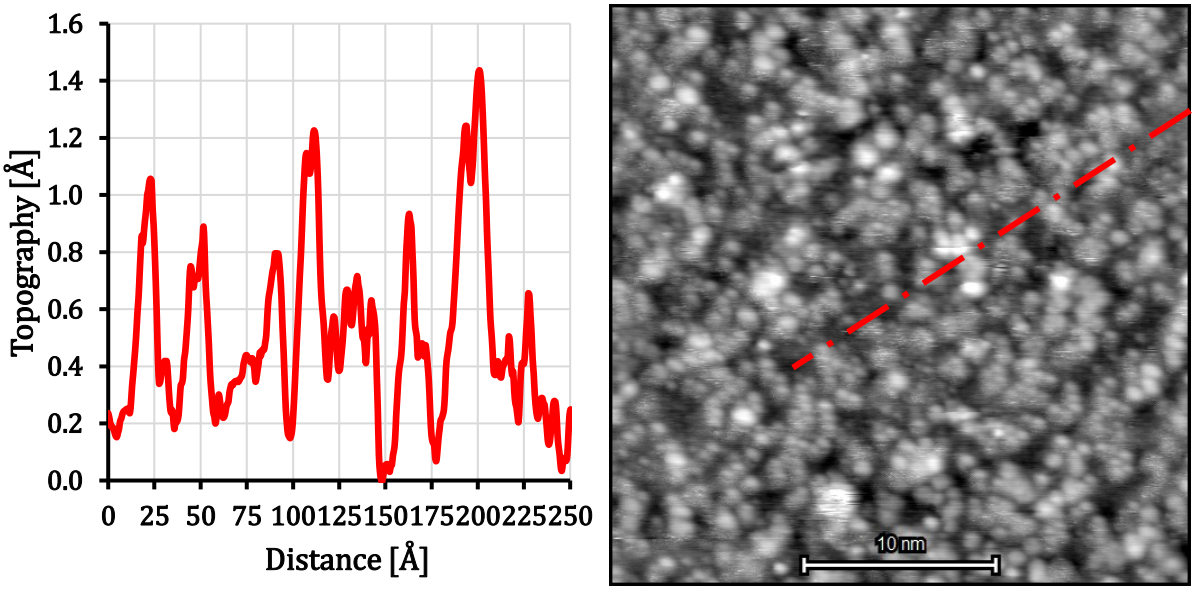

Fig. 5.2: STM image of a highly doped wafer subjected to flashing at 1200°C. Although the surface is free from contamination, it is riddled with dangling bonds. A height profile is extracted to show the surface roughness. (U_{bias} = -1.37 V; $I_{tunnelling}$ = 487pA; 300 Å x 300 Å)

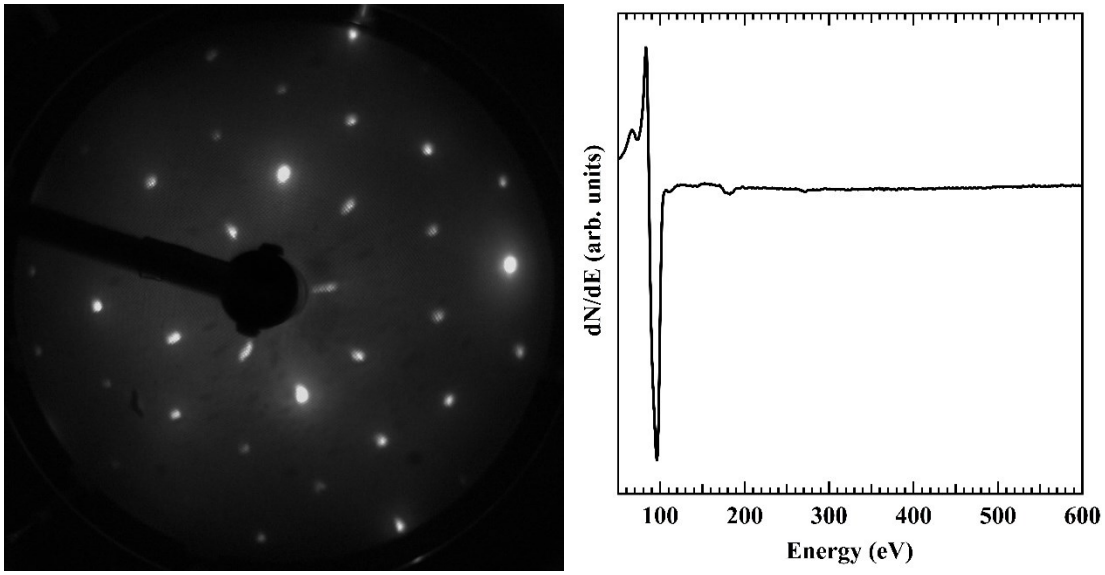

Fig. 5.3: LEED and AES spectra of a highly doped wafer after flashing then annealing at 820°C for 30 minutes. Both LEED and AES are of a quality to suggest the surface may be suitable for molecular deposition. A small carbon transition is visible in the AES at 270eV. LEED Beam Energy: 75eV

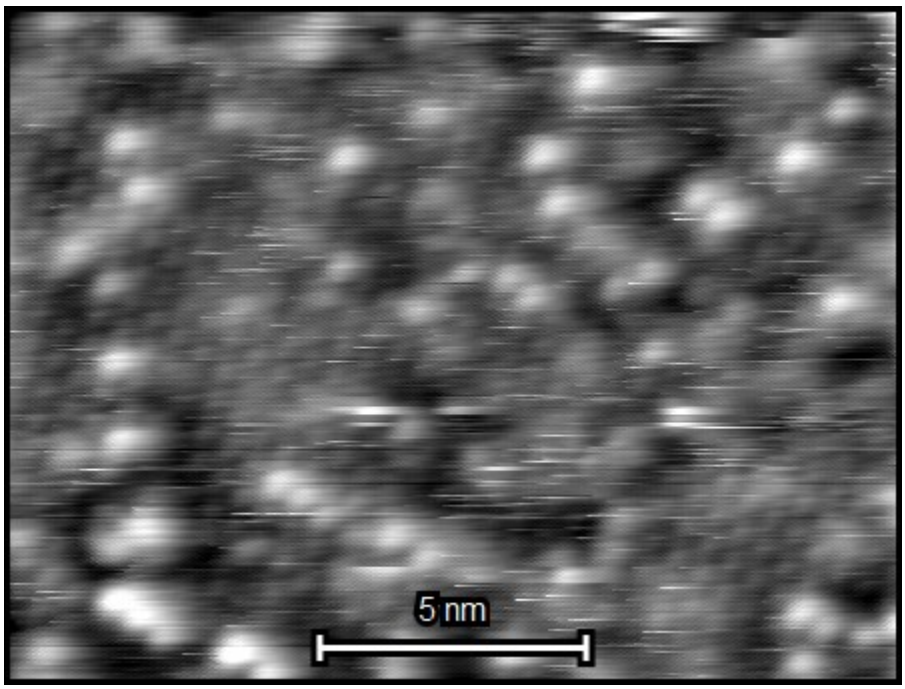

Fig. 5.4: STM image of the highly doped wafer from Fig. 5.3 which was subjected to a half hour anneal at 820°C. The amount of dangling bond defects is still high which makes the surface difficult to resolve in STM. The blurred bright spots correspond to adjacent dangling bonds. The $\sqrt{3}$ lattice is visible in the background. ($U_{bias} = +1.50$ V; $I_{tunnelling} = 441$pA; 166 Å x 125 Å)

The next two figures illustrate the continual improvement to surface quality gained by extending the anneal time to one hour. The LEED pattern is slightly improved in figure 5.5 compared to figure 5.3.

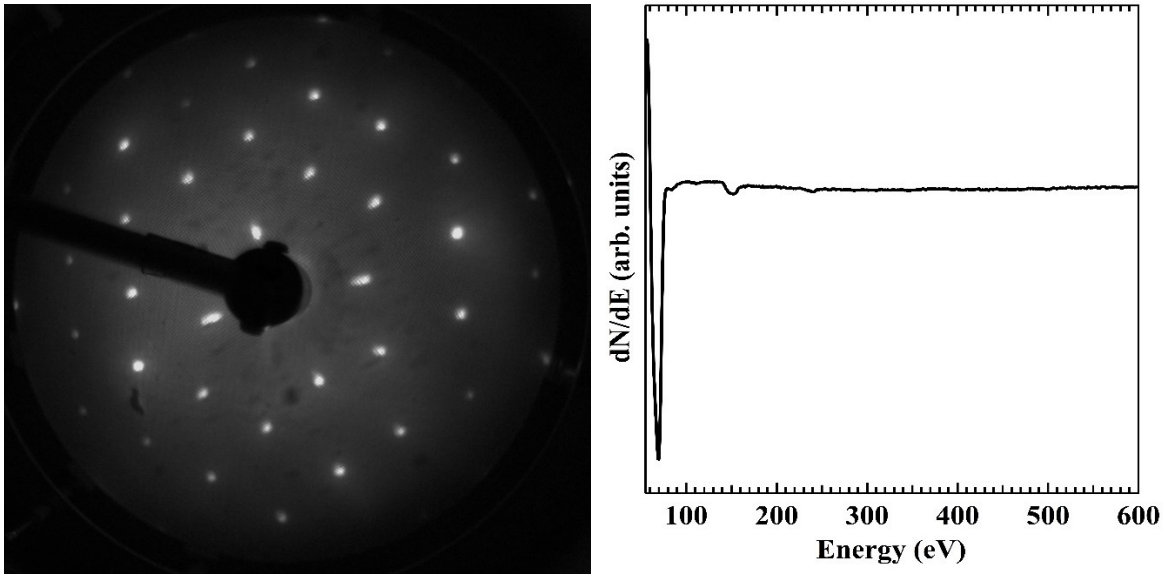

Fig. 5.5: LEED and AES spectra of a highly doped wafer after flashing to 1200°C, then annealing for 1 hour between 800°C and 900°C. A small carbon trace is visible in the AES at 270eV. LEED Beam Energy: 67eV

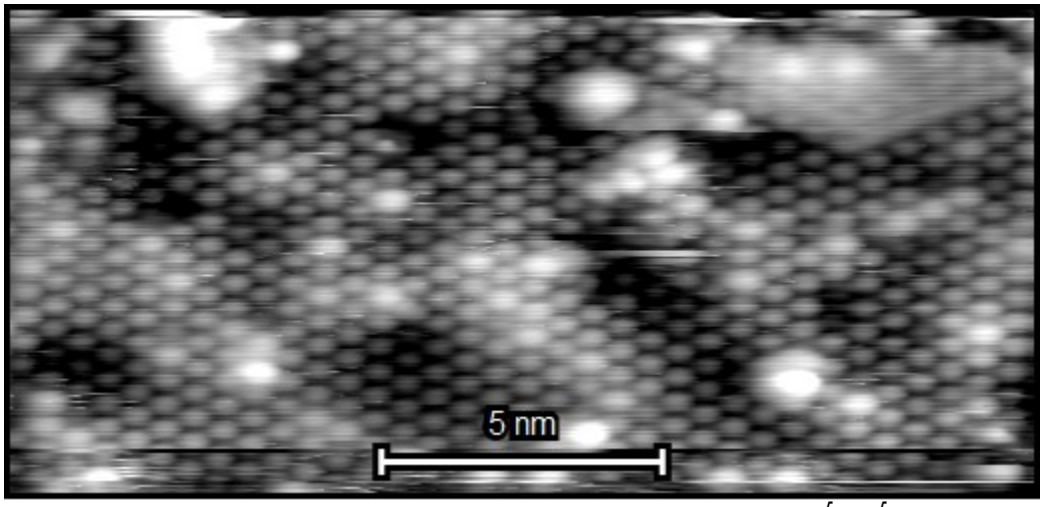

Fig. 5.6: An atomic resolution STM topographic image of the Si(111)-$\sqrt{3}$x$\sqrt{3}$-R30°-B surface as prepared by flashing at 1200°C then annealing for 1 hour between 800°C and 900°C. The dangling bonds are seen as bright spots. Dark spots are boron induced defects. ($U_{bias} = +2.04$ V; $I_{tunnelling} = 416$pA; 182 Å x 82 Å)

The preceding three examples with continually increasing anneal time showed continual improvement in the LEED pattern and the reduction of dangling bonds. However, in doing so, AES revealed that contamination emerged on the surface from what would have been an atomically clean surface without annealing. This illustrates the emergence of a trend: higher temperature annealing or longer duration anneals produced well reconstructed surfaces but at the cost of increased contamination. Our data revealed that partitioning the anneal time into smaller time periods did not prevent the accumulation of contamination unless the quality of the $\sqrt{3}$ reconstruction was sacrificed. In addition, cleaning the wafers *ex-situ* with boiling methanol or with a standard RCA etch (Kern, 1990) did not have a noticeable effect on the resultant $\sqrt{3}$ surfaces.

Raising the anneal time and temperature to 40 minutes at 1000^{o}C met the limit of our experimental instrumentation. Although there was still improvement to the strength of the LEED pattern, the surface started becoming contaminated with carbon and small traces of surface nitrogen and oxygen as revealed by AES. Figure 5.7 shows a comparison of AES spectra of clean wafer prepared by annealing at 950^{o}C for 30 minutes and a contaminated wafer prepared by annealing at 1000^{o}C for 40 minutes. The size of the boron transition is noticeably larger in the wafer annealed at the higher temperature.

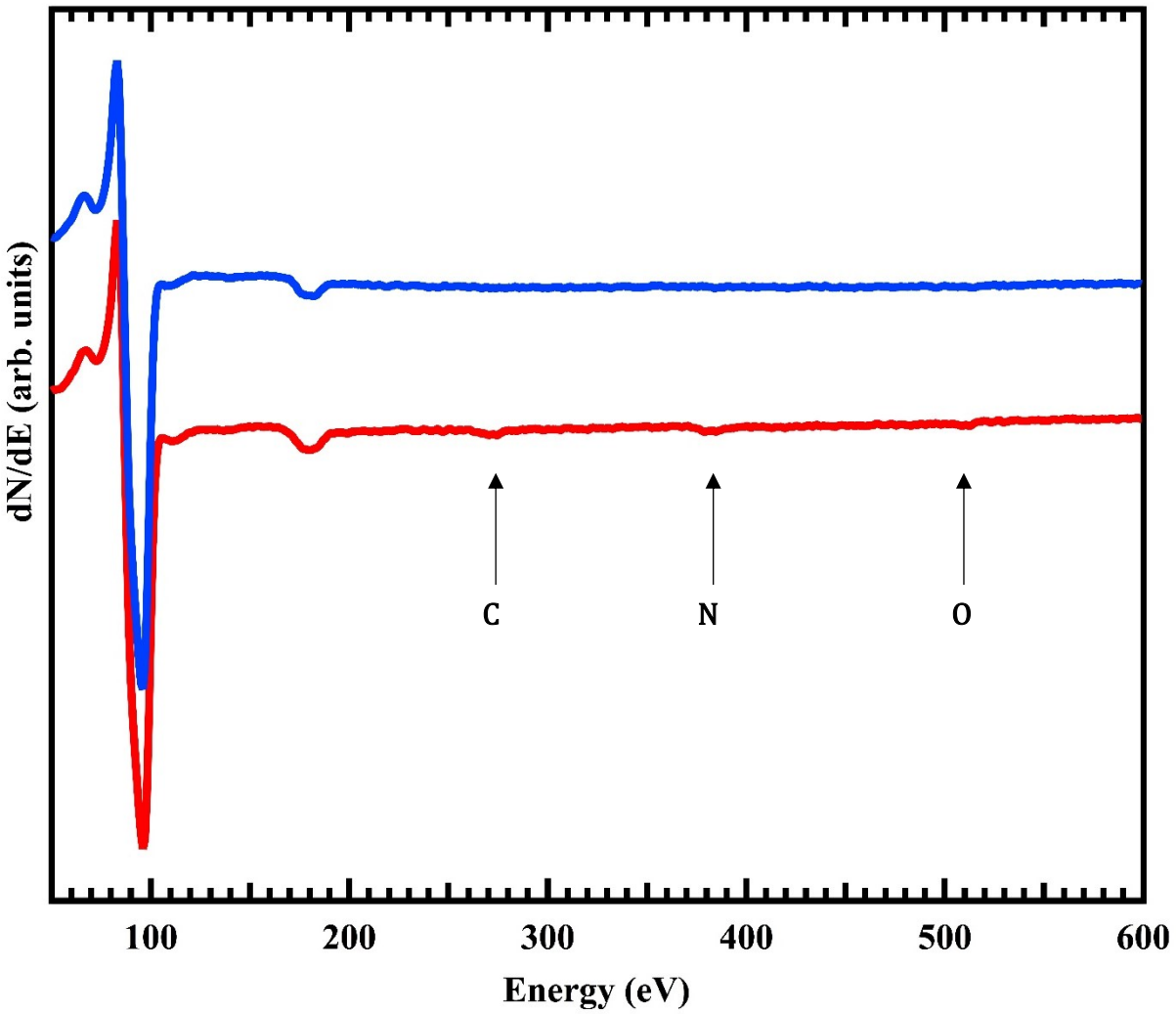

Fig. 5.7: AES spectra of a highly doped wafer after annealing at 950°C for 30 minutes and 1000°C for 40 minutes. Top: AES indicates the sample surface is atomically clean. Bottom: While there is a noticeable gain in the near surface boron, carbon (KLL) and oxygen (KVV) transitions appear in the AES spectrograph at 270eV and 520eV. The silicon signals for both curves are normalized.

The LEED, AES and STM data for the best-case wafer procedure is shown in the figures below. The procedure used in this best case was flashing the wafer to temperatures >1200°C and then holding it at 930°C for 100 minutes.

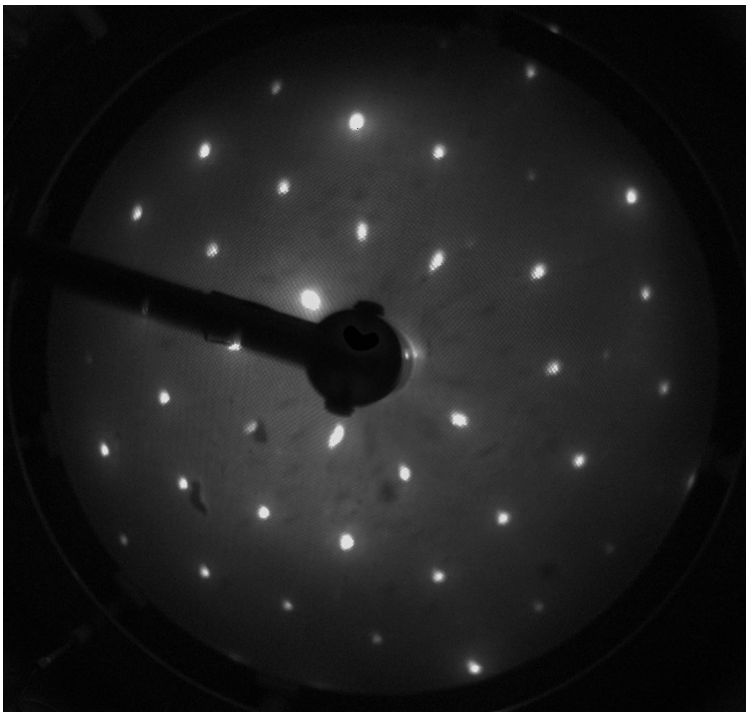

Fig. 5.8: The $\sqrt{3}x\sqrt{3}$ diffraction pattern observed with LEED of the best-case Si-B recipe. LEED Beam Energy = 70eV

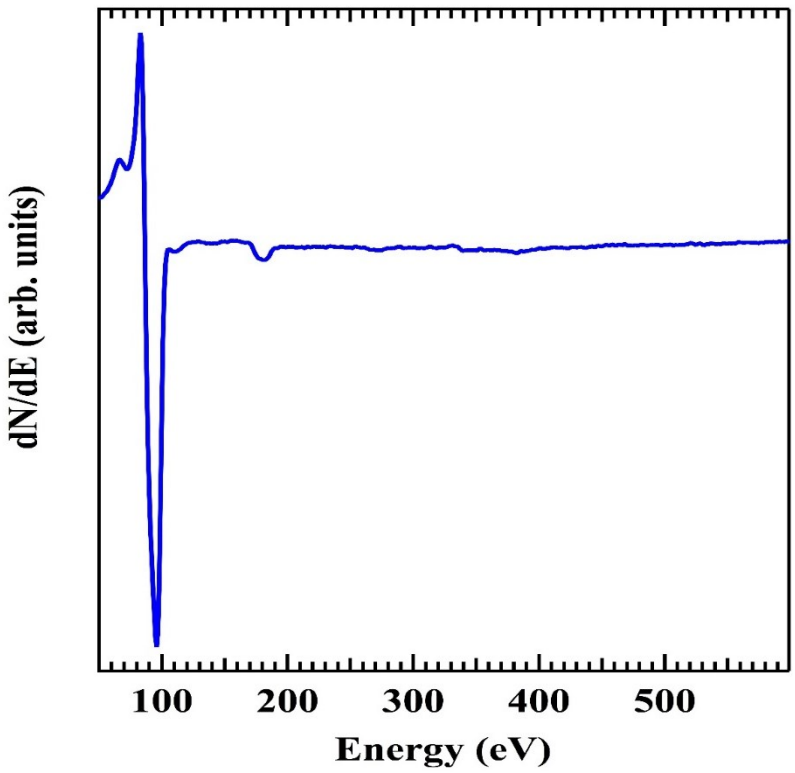

Fig. 5.9: Auger electron spectroscopy of the best-case Si-B recipe. The spectra shows a relatively strong boron signal (180eV) with some carbon (270eV). The change in signal at 340eV and 380eV are merely artifacts.

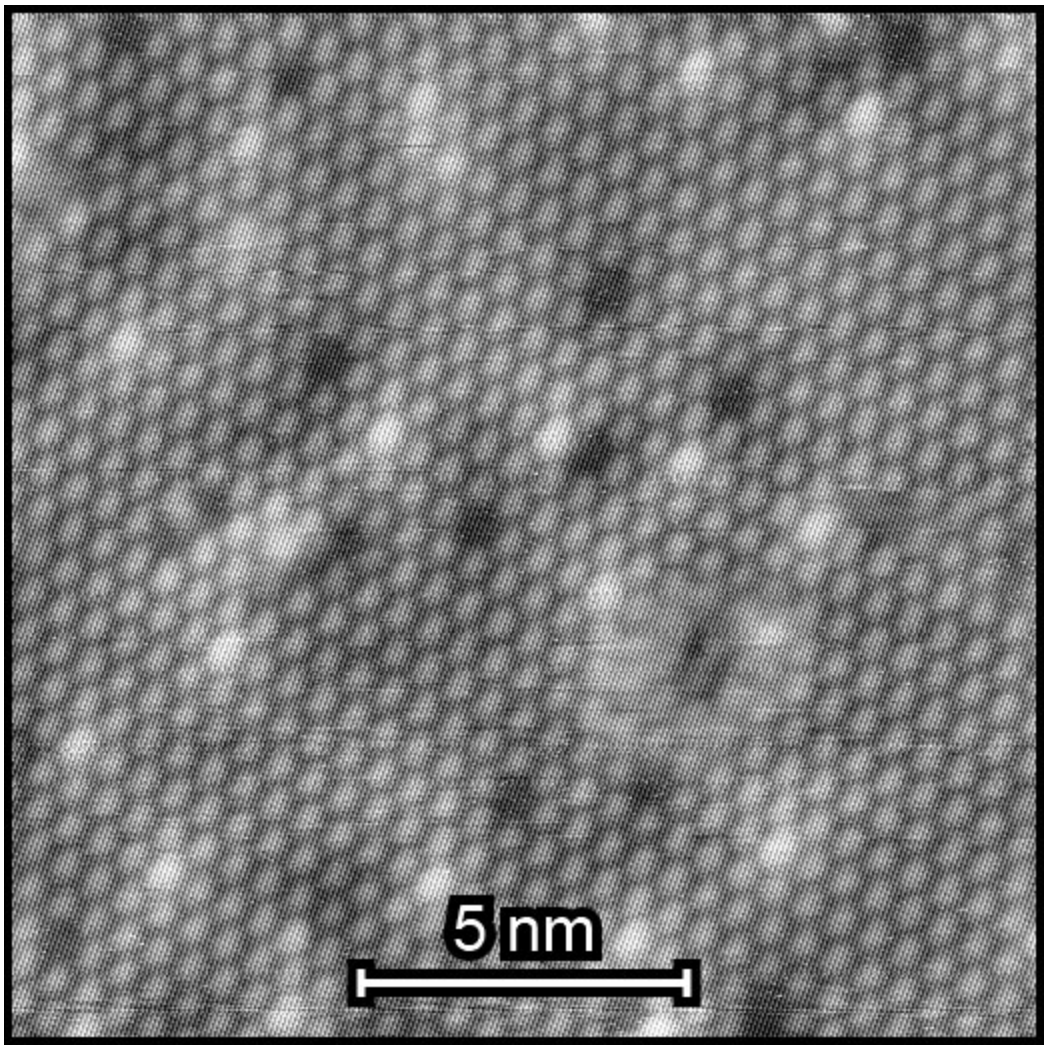

Fig. 5.10: A STM image of the best-case Si-B recipe. Bright spots are unsaturated dangling bonds due to a lack of S5 position boron. Dark spots represent defects. ($U_{bias} = +1.44$ V; $I_{tunnelling} = 0.51$nA; 156 Å x 156 Å)

5.1.3 B_2O_3

We also attempted to prepare a Si(111)-$\sqrt{3}$x$\sqrt{3}$-R30°-B surface following an approach outlined by Nogami et al. (1994). First a phosphorus-doped Sil'tronix[42] (111) silicon wafer miscut by 1° towards $(\overline{11}2)$ was used to prepare a 7x7 reconstruction. Then, boron trioxide

[42] https://www.sil-tronix-st.com/en/home

was deposited to the surface and annealed. Upon heating, surface boron diffuses to the T4 position and the surface oxide desorbs.

To create the 7x7 reconstruction, samples were flashed near 1200^{o}C to remove surface carbon (Lin et al., 1998). Samples were then held near 1060^{o}C for up to a minute so as to avoid atomic step bunching. This action is required because of the miscut to our silicon wafers. The samples were then slowly cooled to ~850^{o}C where they were held for up to 1 minute. Holding ~850^{o}C and slowly cooling to ambient temperature, encourages the growth of extended 7x7 domains.

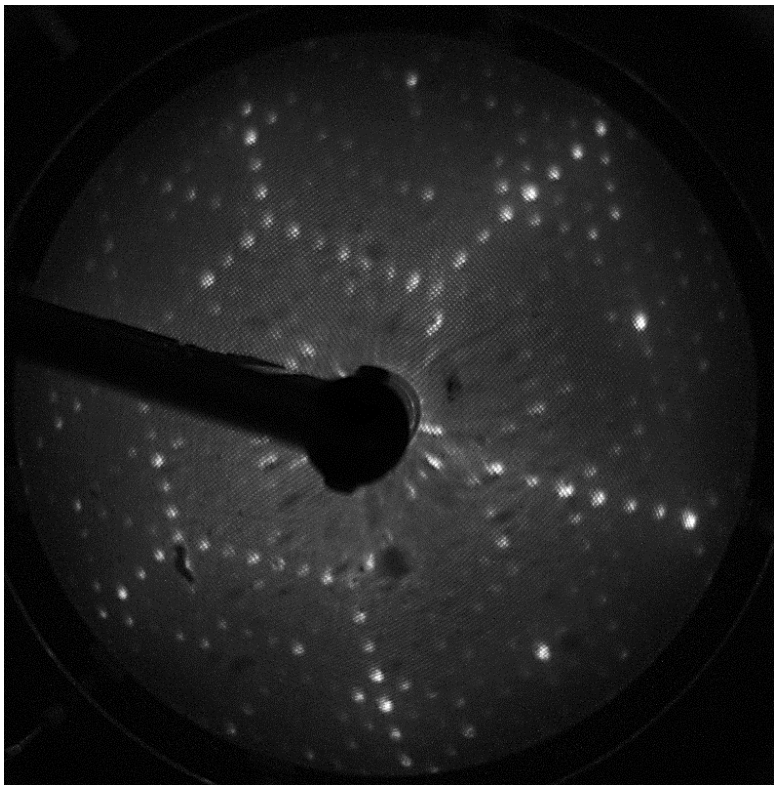

Fig. 5.11: The 7x7 diffraction pattern observed with LEED before deposition of boron trioxide to form the Si-$\sqrt{3}$x$\sqrt{3}$-B reconstruction. Beam energy = 68eV

Boron-trioxide was deposited by first preheating B_2O_3 in a tungsten basket at 7.3 A for 5 minutes and depositing for 30 minutes. The mixture was then annealed twice: twenty minutes at 600^{o}C to permit the surface boron to diffuse into the bulk, forming the reconstruction and an

additional 15 minutes around 780°C to remove the surface oxide. This approach did not produce a √3 surface of the same quality as annealing the low resistivity boron doped wafers. We can see by the LEED diffraction pattern in figure 5.13 that the spots are dimmer and less sharp when compared to figure 5.8. This indicates that the B_2O_3 prepared surface is not as uniform and periodic as when prepared via the doped wafers.

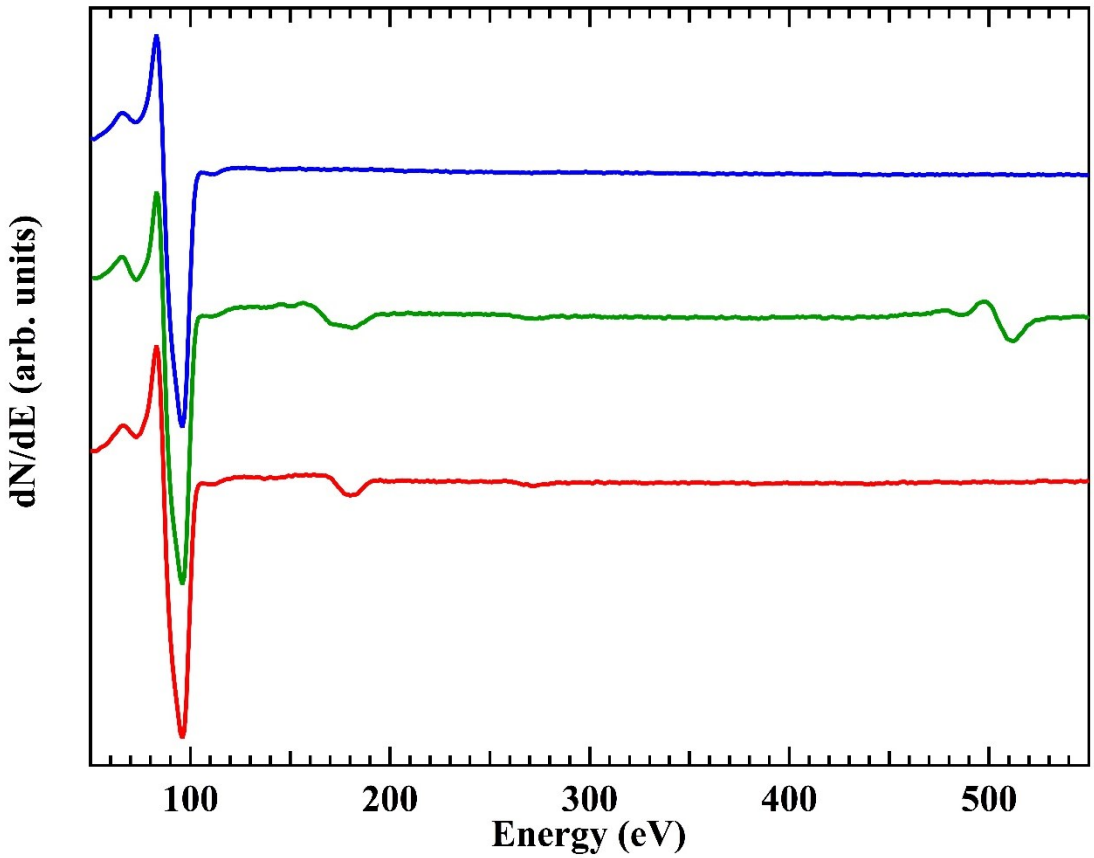

Fig. 5.12: Auger electron spectroscopy of the silicon surface at all stages of boron trioxide deposition. Top curve: After initial cleaning and before deposition of B_2O_3. The spectra shows only a silicon signal. Middle curve: After deposition of B_2O_3. The surface shows elemental boron and oxygen signals. Bottom curve: After annealing the silicon, boron, oxygen mixture at ~800°C. There is a reduction of boron signal while the oxygen signal is eliminated. The silicon signals for all curves are normalized.

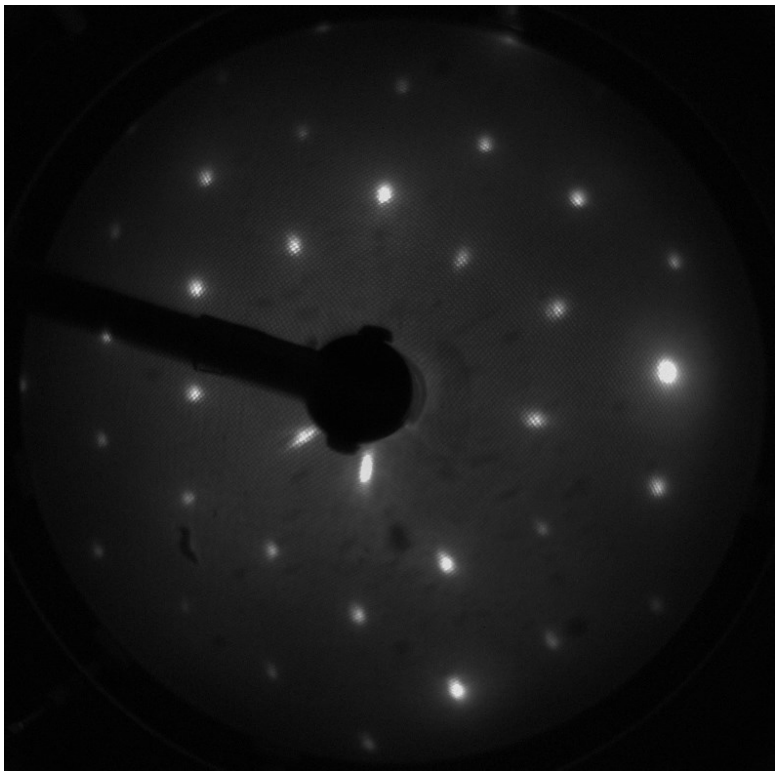

Fig. 5.13: The √3 diffraction pattern observed with LEED after deposition and annealing of boron trioxide. LEED Beam Energy = 68eV

5.1.4 Molecular Deposition

We were not able to achieve self-assembly on the Si-√3x√3-B surface due to difficulty preparing said surface as outlined previously. The difficulty lies in the apparent trade off between inducing sufficient boron concentration to passivate dangling bonds and the level of surface contamination. The annealing process to bring boron to the subsurface S5 position could not be sustained for as long, or at as high of a temperature necessary to form the reconstruction without contaminating the surface. Although some preparation procedures produced LEED and Auger spectra which suggested the surface had a strong boron reconstruction and was free from contamination, the surface was still insufficiently passive to support SA.

When depositing TBTANGO on the best-case silicon-boron surfaces, TBTANGO

molecules appeared to “hit-and-stick”, presumably to unsaturated dangling bonds, as described in Chapter 2.4. STM images (figure 5.15) clearly reveal no evidence of self-assembly, but rather randomly dispersed features which are ascribed to individual molecular fragments.

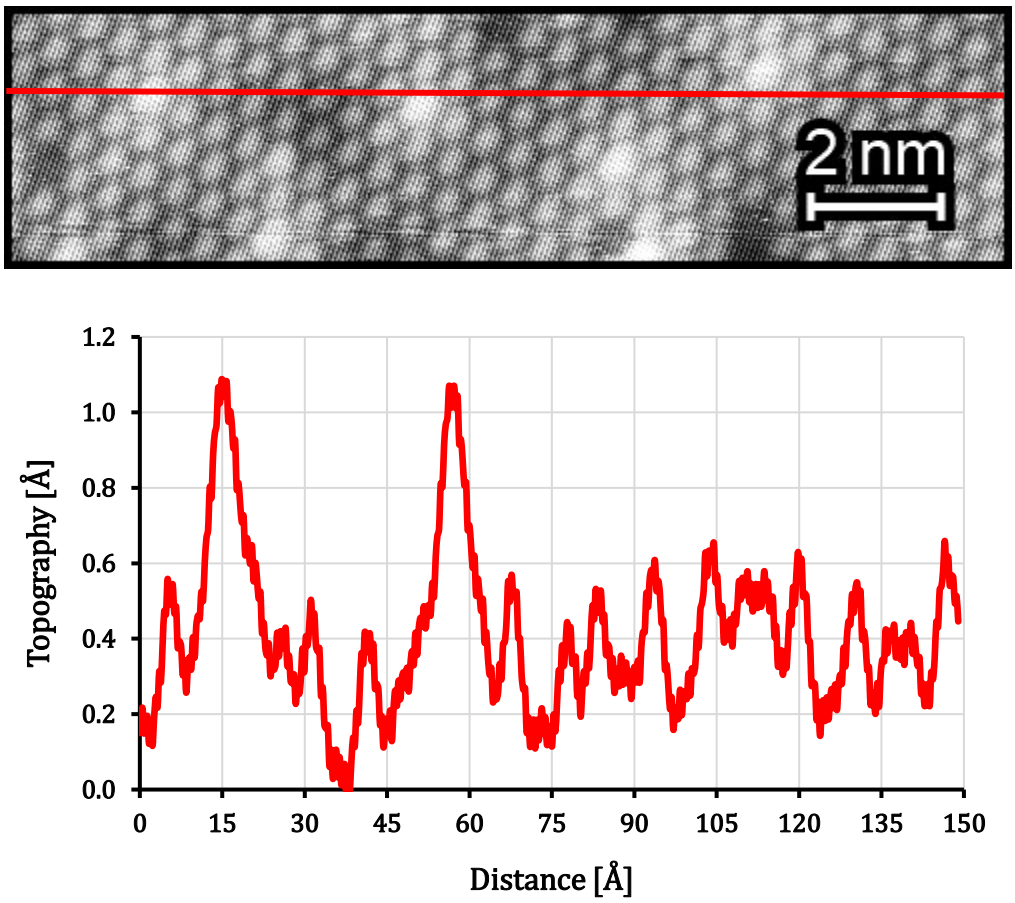

Fig. 5.14: A height profile extracted from a clean Si-B surface before deposition of TBTANGO. Note the difference in scale between the height profile below. Dangling bonds are resolved as one Ångström, ($U_{Sample} = +1.44$ V; $I_{tunnelling} = 510$pA; 156 Å x 63 Å)

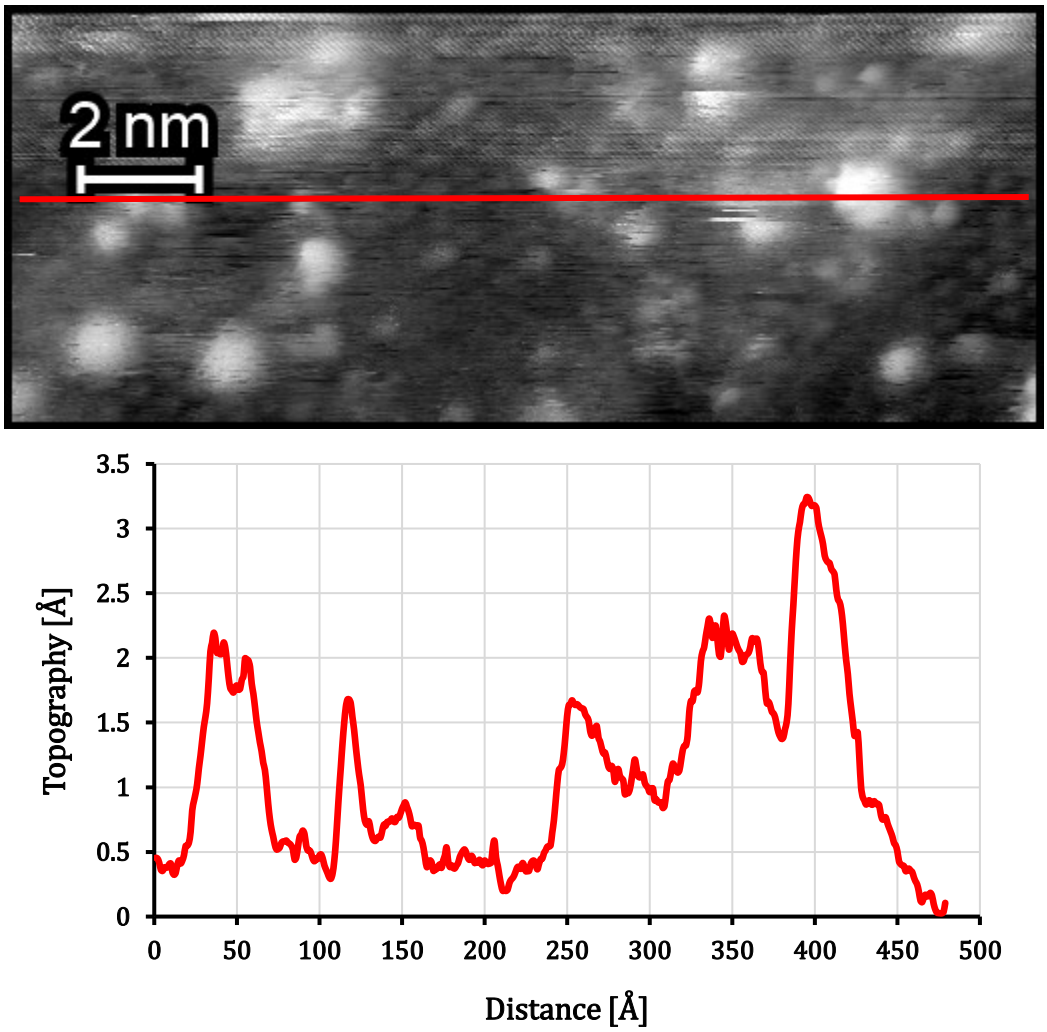

Fig. 5.15: A STM image of TBTANGO deposited on a Si-B surface with large protrusions believed to be molecular fragments bonded to unsaturated silicon atoms. A height profile was extracted along the red line. These protrusions are much larger than the ones measured in figure 5.14 suggesting the surface protrusions after deposition are fragments of or complete molecules. ($U_{Sample} = 1.53$ V; $I_{tunnelling} = 0.51$nA; 173 Å x 69 Å)

5.2 Ag(111)

5.2.1 Substrate Preparation

Our silver surface is a purchased single crystal[43] with an exposed (111) plane. To clean the surface, the crystal is subject to repeated sputter-anneal cycles. Usually, two cycles are

[43] www.spl.eu

sufficient to clean the crystal provided it has not been exposed to atmosphere. When sputtering, the chamber is backfilled to $5x10^{-6}$ Torr with argon. A filament is used to create Ar^+ ions which are accelerated to 1000eV. The crystal is sputtered under these conditions for 30 minutes per cycle.

The anneal cycle is also 30 minutes in duration. The crystal is heated indirectly by a hot filament. The temperature of the sample is monitored with an internal thermocouple placed close to the sample. The temperature following the 30 minute anneal can exceed 240°C. Clean Ag(111) surface data is shown below. In the STM topograph, fuzzy step edges indicate the surface is clean. In fact, if the steps do not appear fuzzy, the surface is not clean. Fuzzy step edges are a consequence of extra silver adatoms which constantly attach and detach from step edges at room temperature (Mugele et al., 1998).

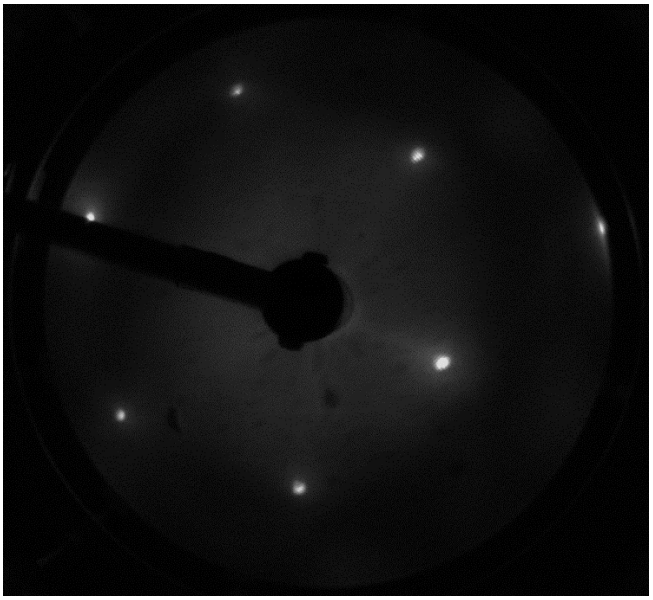

Fig. 5.16: The 3-fold symmetric LEED pattern resulting from the Ag(111) plane. Beam energy = 68eV

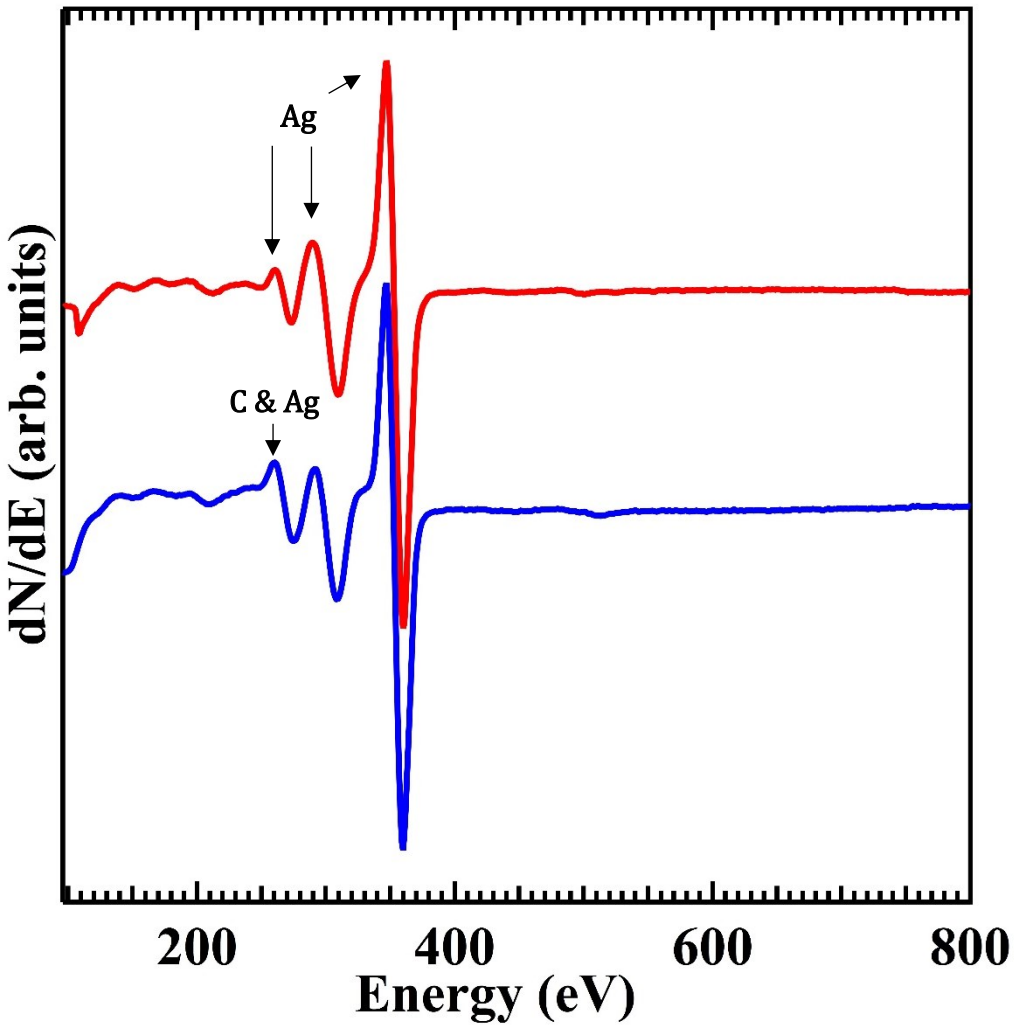

Fig. 5.17: Two Auger spectroscopy comparing the clean Ag(111) surface after sputter-anneal cycles (top) to one with 1 monolayer of TBTANGO (bottom). There is increased intensity of the carbon signal (270eV) and a slight increase of the oxygen signal (~510eV). The silver signal is normalized between both curves.

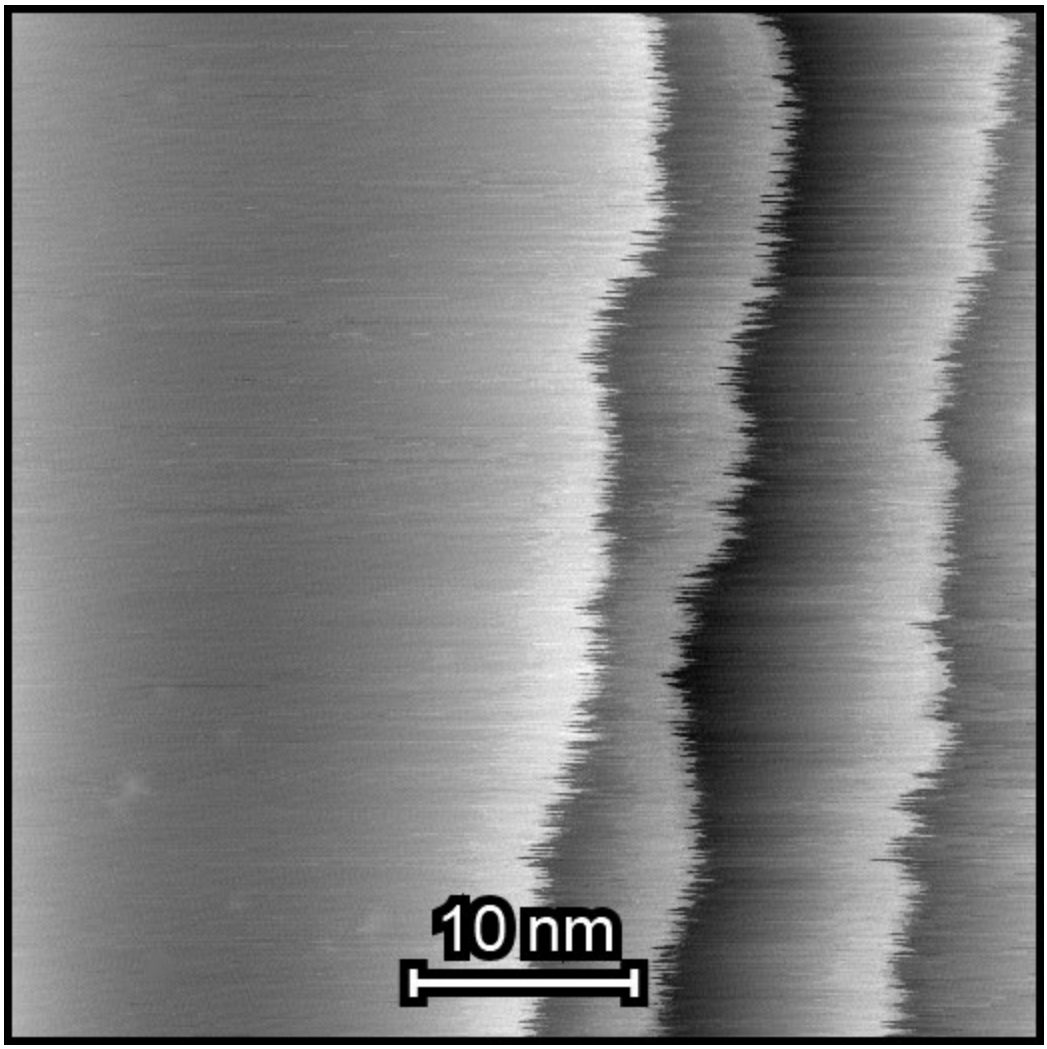

Fig. 5.18: A STM image of the clean Ag(111) crystal. (U_{bias} = -0.34 V; $I_{tunnelling}$ = 0.83nA; 464 Å x 464 Å) The step edges appear "fuzzy" because the silver has an abundance of adatoms which are constantly attaching and detaching from the step edge.

5.2.2 Room Temperature Deposition on Ag(111)

The room temperature deposition of TBTANGO onto the silver single crystal was performed with the molecular evaporator preheated to sublime the TBTANGO before opening a shutter to the sample. The temperature was crudely monitored by a thermocouple close to the crucible. Throughout the process, the evaporator unit was cooled with water. The silver sample was exposed to TBTANGO molecules for 7 minutes.

Below are several figures showing the room temperature phase at low coverage.

Monomer, dimer and trimer organometallic structures which have metal-organic linkages are observed in STM. The mix of surface oligomers is disorganized. Organometallic dimers seem to be the most common of the three structures. Dimers, with monomer and trimer components, can be seen in figures 5.19 and 5.20. The mixture of monomers, dimers and oligomers is indicative of partial dehalogenation of the TBTANGO units. Incomplete dehalogenation is not a surprise as past works on Ag(111) have demonstrated that the dehalogenation of brominated tetrathienoanthracene molecules occurs around 50°C (Eichhorn et al., 2014b; Gutzler et al., 2014) and that about 38% of bromine atoms on the molecule 1,3-bis(p-bromophenyl)-5-(p-iodophenyl)benzene dissociate at room temperature (Eichhorn et al., 2014b).

The mix of monomers, dimers and shorts chains is consistent with the findings of Lafferentz et al., (2012) (Chapter 2.3) who found that molecular dimers are formed from molecules with one dehalogenated binding site when studying molecules with both iodine and bromine atoms in a *trans*- configuration on Au(111) and Au(110). Small chains are formed if multiple halogen sites dissociate. Groups of dimers and oligomers are identified in figure 5.19. It was observed that oligmer structures often pack together as shown in figure 5.20, where two oligomers are flanked by a monomer and dimer. This phase does not have a systematic packing motif.

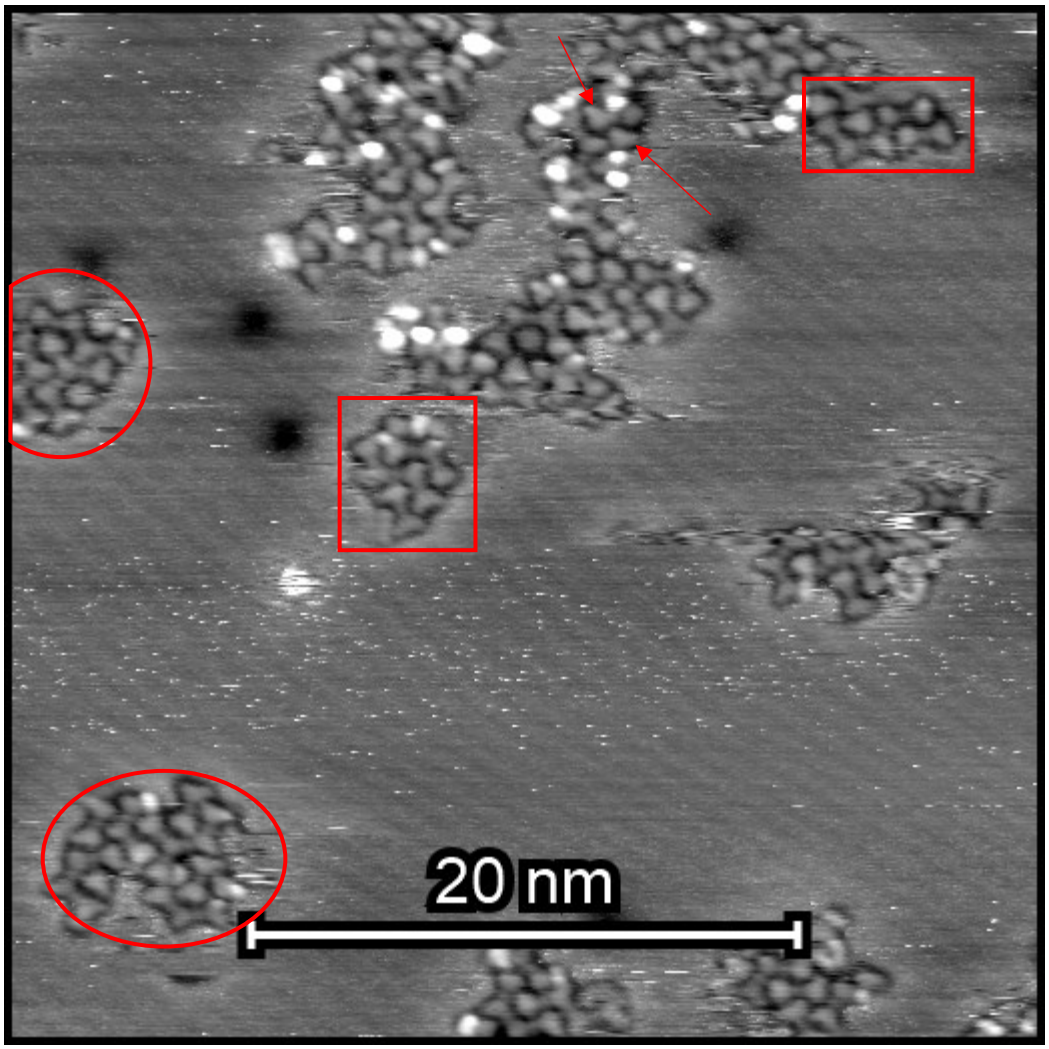

Fig. 5.19: A STM image of the low coverage room temperature phase of TBTANGO on Ag(111). The structures are a mix of silver-carbon linked complexes containing two or more TBTANGO molecules. The single monomers (highlighted with arrows) in close proximity give evidence that some TBTANGO units remain halogenated after deposition. Dimers are enclosed in boxes and oligomers are circled. (U_{Sample} = -1.46V; $I_{tunnelling}$ = 144pA; 375 Å x 375 Å)

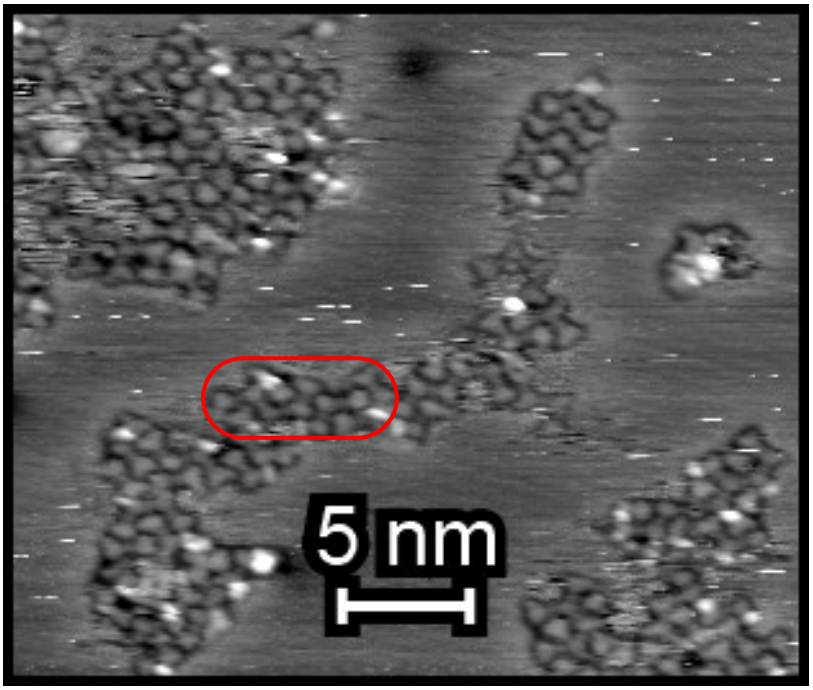

Fig. 5.20: A second STM image of the low coverage room temperature phase of TBTANGO on Ag(111) illustrating the disordered packing of a monomer, dimer and two oligomers in close proximity. Unlike in figure Y1, the three motifs are intermixed (U_{Sample} = -1.46V; $I_{tunnelling}$ = 141pA; 517 Å x 517 Å)

The reaction mechanism which forms organometallic structures in the Ullmann reaction is believed to be the mechanism behind the SA of TBTANGO on Ag(111). Figure 5.21 illustrates C-Ag bonds as identified in STM. The links we observe for TBTANGO on Ag(111) are visually very similar to those observed by Gutzler et al., (2009). This indicates the bonds between TBTANGO molecules are carbon-metal based linkages of the type discussed in Chapter 3.8. Figures 5.22 and 5.23 were chosen to highlight the silver-organic linkages which are characteristic of halogenated molecules on silver.

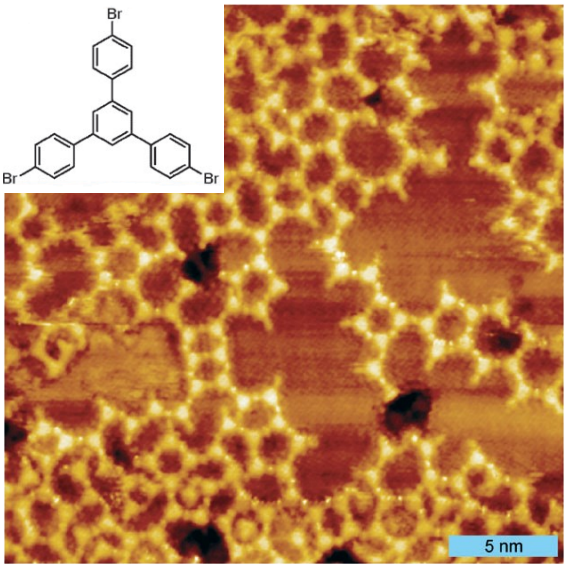

Fig. 5.21: A STM topograph showing a dehalogenated organic molecule after deposition on Cu(111) at room temperature. The molecule is shown in the inset. Spherical protrusions associated with surface copper atoms between radicals are clearly visible (Gutzler et al., 2009)[44]. (U_{Sample} =-1.85 V, $I_{tunnelling}$ = 248 pA)

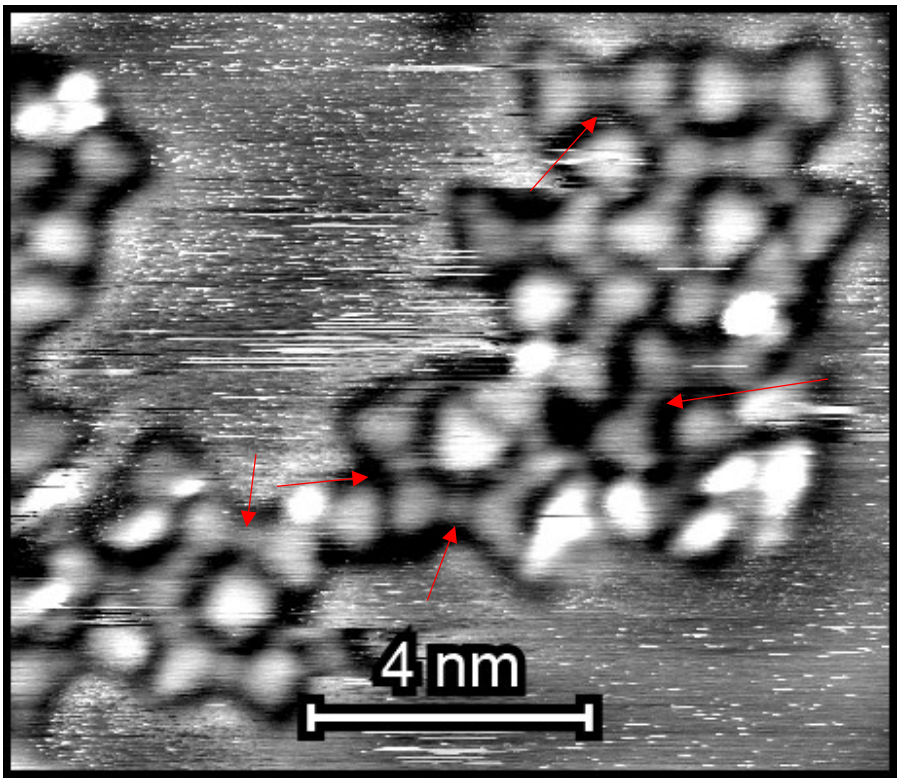

Fig. 5.22: A small scale STM image of the room temperature phase of TBTANGO on Ag(111). Small spots (red arrows) can be identified on each side of the structures. These spots are

[44] Reproduced from Ref. (Gutzler et al., 2009) with permission from The Royal Society of Chemistry.

associated with the silver surface atom which link TBTANGO units provided the terminal bromine atoms have dissociated. (U_{Sample} = -1.46V; $I_{tunnelling}$ = 142pA; 140 Å x 110 Å)

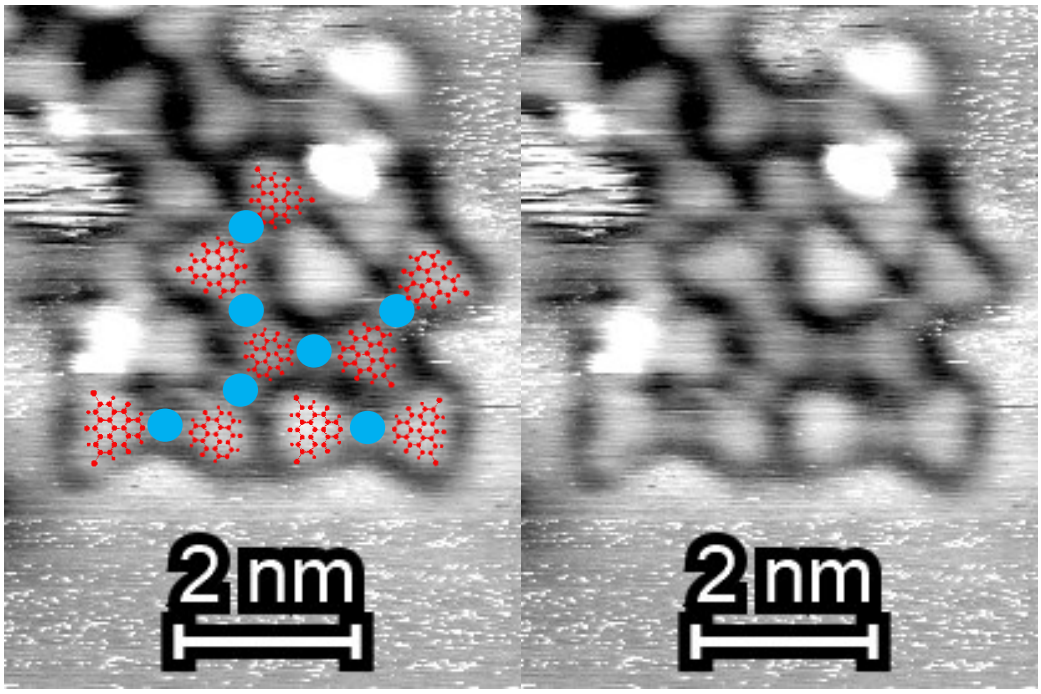

Fig. 5.23: A side-by-side illustration of a small scale STM image of the room temperature phase of TBTANGO on Ag(111) with and without a proposed silver-carbon linkage system. Blue circles cover the silver surface atoms while TBTANGO derivatives are marked in red. (U_{Sample} = -1.46V; $I_{tunnelling}$ = 138pA; 71 Å x 66 Å)

5.2.3 Elevated Temperature Deposition on Ag(111)

The deposition of TBTANGO on silver at elevated temperatures leads to a more ordered and extended organometallic SAMN consisting of a porous honeycomb network with 6 TBTANGO molecules per pore. As in the room-temperature deposition, it was found that the surface silver atoms insert themselves between TBTANGO units. The protrusions associated with silver atom linkages can be seen in figure 5.24 below. The same deposition parameters were used as for the room temperature phase except the TBTANGO was deposited for 14 minutes and the substrate was heated to approximately 240°C.

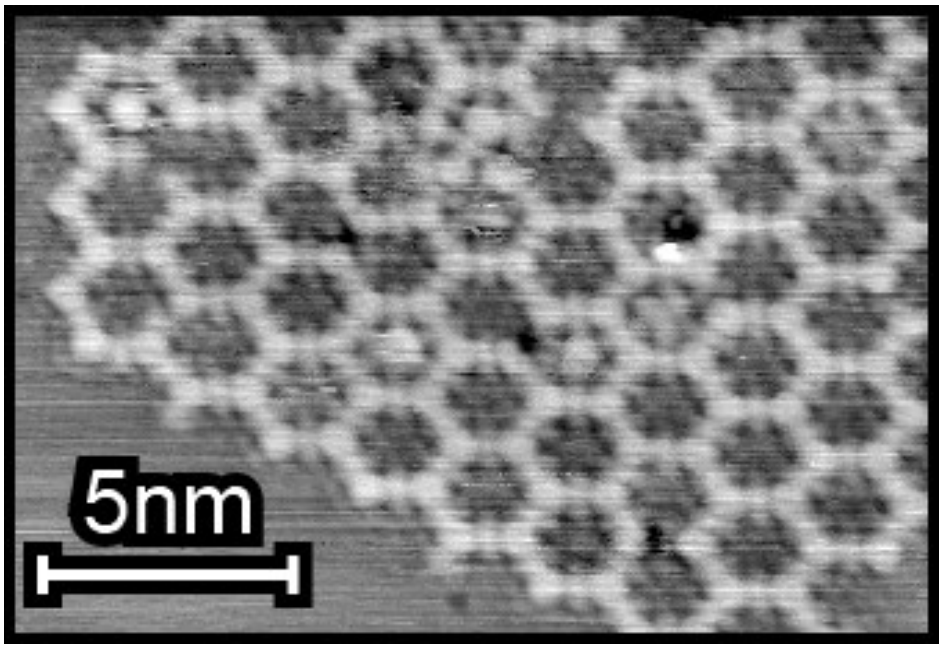

Fig. 5.24: A small scale STM image illustrating the honeycomb network with what appears to be 6 dehalogenated TBTANGO molecules per pore. To an extent, the image also shows silver atoms between monomers and the dissociated bromine atoms within pores. (U_{Sample} = -1.31 V; $I_{tunnelling}$ = 0.52nA; 181 Å x 123 Å)

The pores are often filled with what is believed to be the detached bromine atoms trapped inside. The hexagonal, or pore structure, in the STM images appears to have a large round structure within, see figure 5.25 or 5.28. In higher resolution images, such as figure 5.24 above, these round structures are resolved as 6 smaller protrusions. This observation is consistent with Beiri et al. (2011) who found an organometallic surface structure with filled pores when depositing dimethylmethylene-bridged triphenylamine precursors (DTPA) at 200^{o}C on Ag(111). The DTPA molecule is identical to TBTANGO but with the carbonyl bridges replaced by dimethylmethylenes. The consensus is that bromine atoms which have dissociated on coinage metal substrates are stabilized within the pore or by pore edges (Beiri et al., 2011). Moreover, bromine atoms are known to remain on the Ag(111) surface after dehalogenation (Cardenas et al., 2013). Di Giovannantonio et al., (2013) found bromine atoms actually play a part in stabilizing a particular organometallic SAMN on Cu(110) after dehalogenation from the

molecular units.

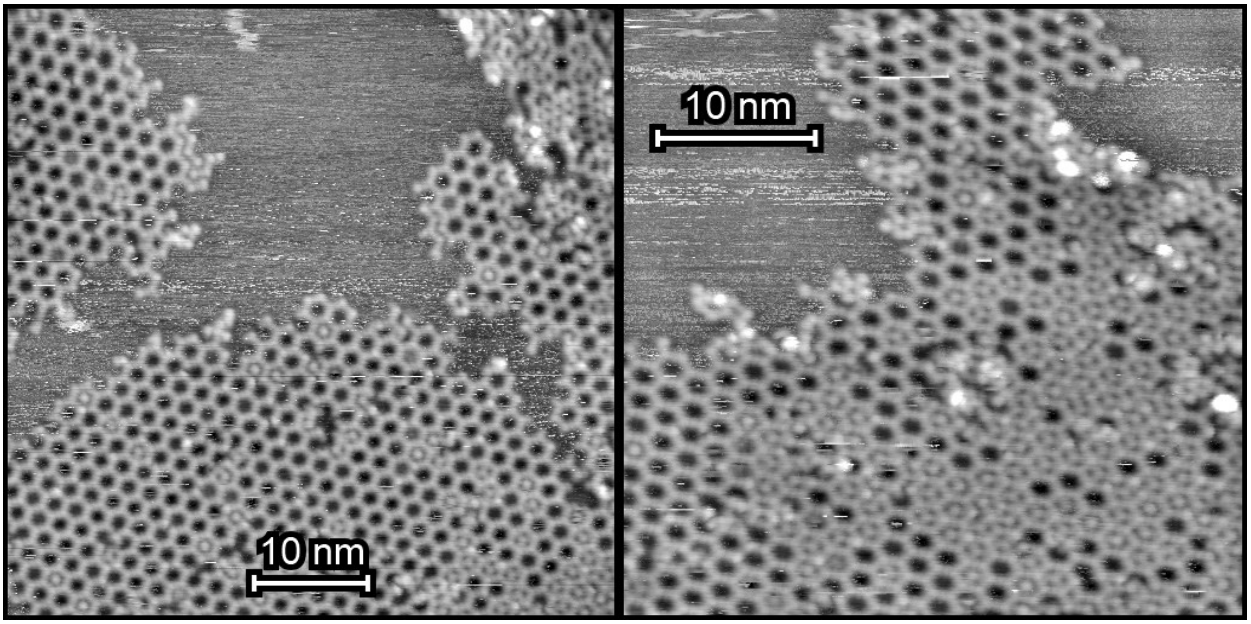

Fig. 5.25: STM images of the honeycomb network taken at sub-monolayer coverage. Empty and filled pores are visible in both images. Left: $U_{Sample} = -0.99V$; $I_{tunnelling} = 186pA$; 534 Å x 534 Å Right: $U_{Sample} = -0.91V$; $I_{tunnelling} = 179pA$; 391 Å x 384 Å

According to our measurements, the unit cell for the pore structure is (19.8 ± 0.5) Å x (19.8 ± 0.5) Å–R $(60.3 \pm 6)^{o}$. Within error, the cell spacing is commensurate with the substrate surface as the surface vectors are 7 times larger. The underlying substrate spacing is 2.89 Å. The various surface aggregates are all aligned with one another, suggesting the overlayer has only one domain and thus a definite epitaxial relationship with the Ag(111) face.

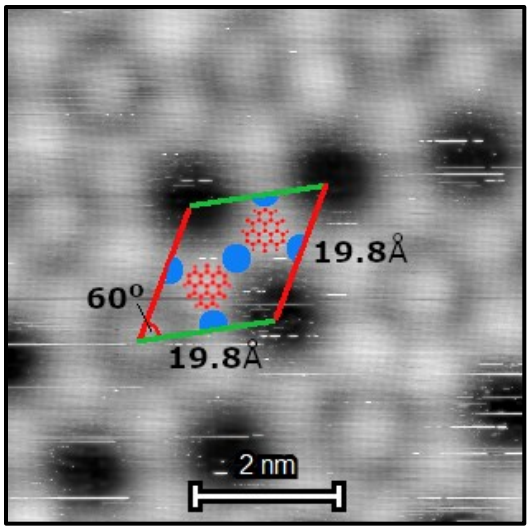

Fig. 5.26: The measured unit cell showing the dehalogenated TBTANGO molecules in red, and the silver atoms as blue circles. The separation angle was measured to be ~60.3° and the length of both surface vectors is 19.8 Å. ($U_{Sample} = +0.92V$; $I_{tunnelling} = 170pA$; 72 Å x 72 Å)

When compared with DFT calculations of the pore-to-pore distance of silver atom linked dehalogenated TBTANGO molecules, the measured cell is plausible. A two pore structure consisting of 10 dehalogenated TBTANGO monomers was calculated according to density functional theory. Monomers were linked using silver atoms. Terminal halogen atoms were replaced by hydrogen atoms. The metal coordinated complex of dehalogenated TBTANGO molecules was modelled using mixed basis sets as described in Chapter 4.4. The resultant two pore structure had a pore-to-pore length of ~22.1 Å and the surface vector separation angle was exactly 60°.

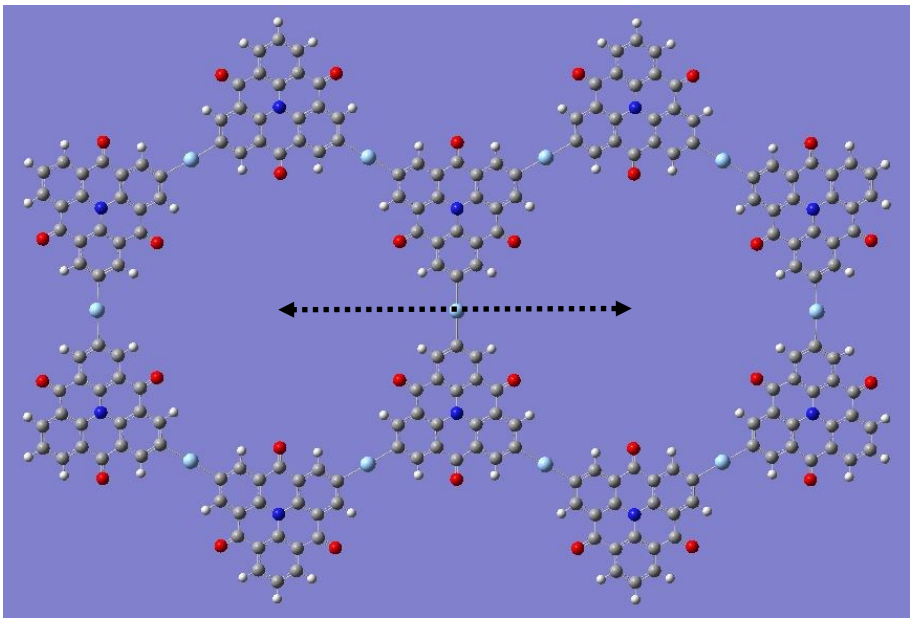

Fig. 5.27: The DFT calculated two pore silver atom coordinated complex. TBTANGO molecules are dehalogenated. Terminal bromine atoms were replaced by hydrogen atoms for this calculation. The pore-to-pore distance was calculated as ~22.1 Å.

In some cases, ordered and disordered closely-packed phases were also observed. The encircled regions in figure 5.28 show the ordered closely packed phase. Figure 5.28, like all data of the close packed phase, shows the phase along the break of an atomic step. This phase may be a self-assembled phase of silver atoms bonded to three dehalogenated TBTANGO molecules. Preliminary results of the ordered close packed phase suggest the repeated units are spaced every 9.1 Å in comparison to the 19.8 Å spacing of the honeycomb hexagonal structure. Even at 9.1 Å, the spacing would be too large to correspond to an ordered arrangement of bromine atoms. Figure 5.29 shows silver atoms covalently linked to three organic molecules per atom. There is a striking similarity between this close packed phase and a similar structure observed for 2,4,6-tris(4-iodophenyl)-1,3,5-triazine monomers deposited on Ag(111) (Liu, 2019). Triply bonded metal-linked organic SAMNs are not frequently reported in the literature (Liu, 2019).

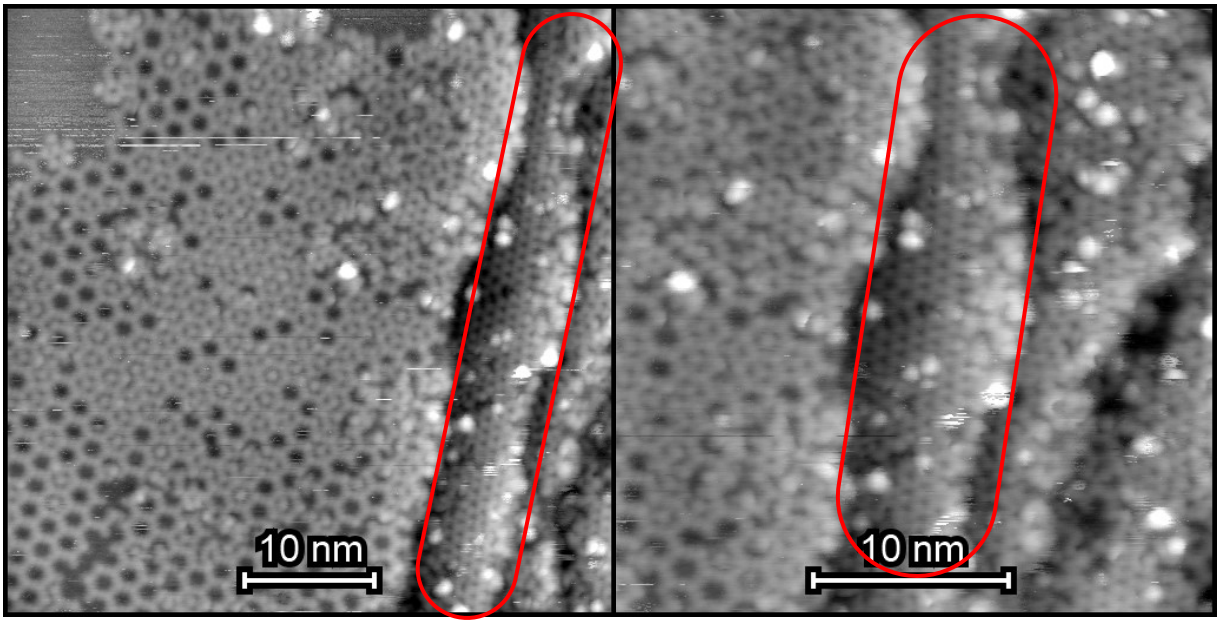

Fig. 5.28: Progressive STM scans of decreasing size on a series of terraces with alternating pore and close packed phases. The terraces are separated by single height atomic steps. The close packed phase is circled in red. On the left terrace, TBTANGO arranges molecules primarily in a hexagonal structure. On the narrow adjacent terrace, TBTANGO is arranged in the ordered close packed phase. (Both scans: U_{Sample} = -0.92V; $I_{tunnelling}$ = 184pA; Left: 465 Å x 465 Å; Right: 309 Å x 309 Å)

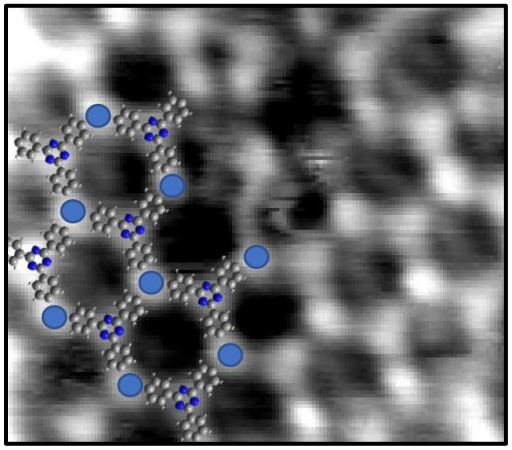

Fig. 5.29: A triply bonded silver atom organometallic structure observed by Liu (2019, p. 76). The organic molecule, triiodophenyltriazine, is overlaid and silver atoms are represented by blue circles. No scale or tunnelling parameters are given.

Analysis of the data reveals the honeycomb hexagonal structure dominates the distribution of the hexagonal, close packed and disordered phases. The distribution of the

three phases is approximately ~80% hexagonal, ~5% close packed and ~15% the disordered phase. The disordered phase is shown in figure 5.30.

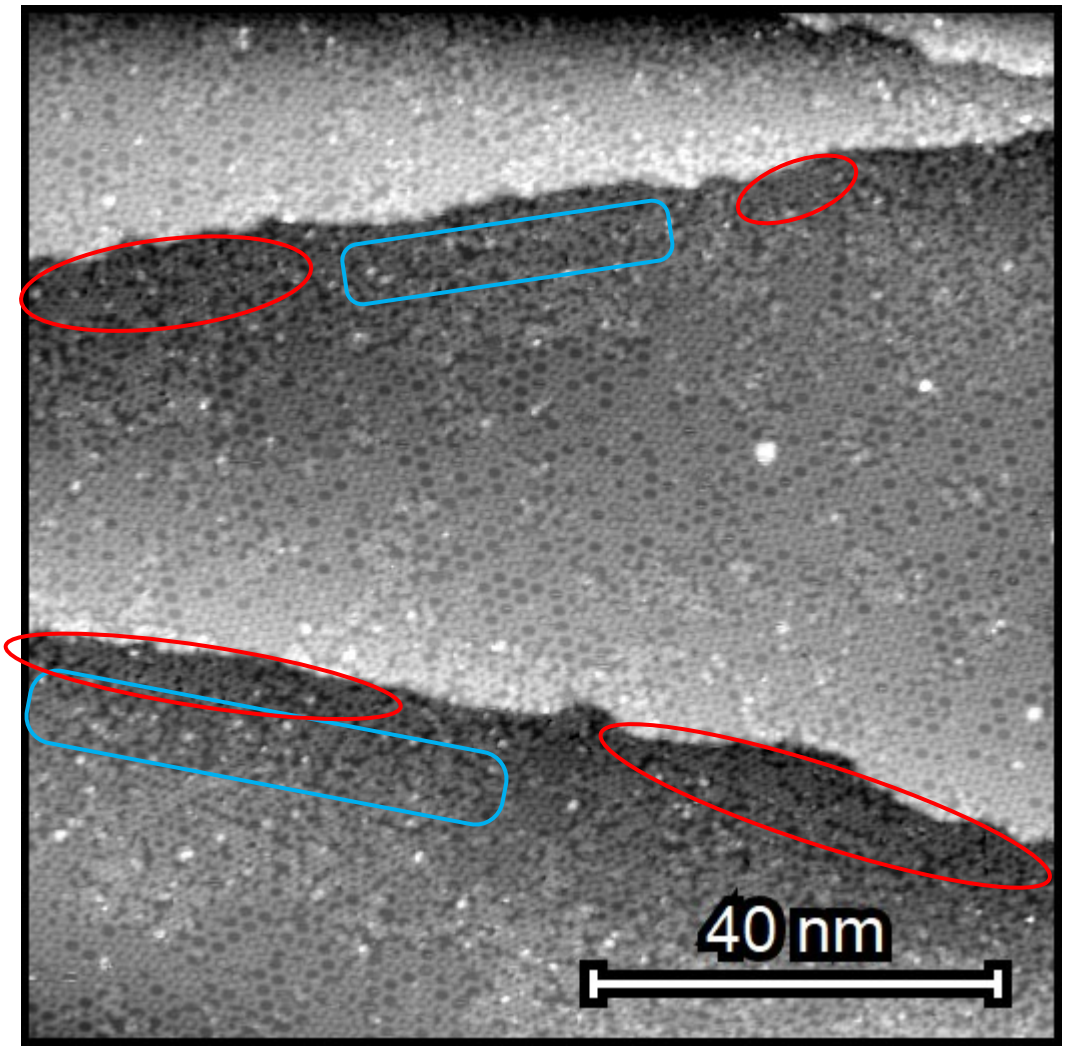

Fig. 5.30: A large scale STM image showing monolayer coverage. Near the step edges, the close packed phase is observed. A disordered transition region exists which bridges the hexagonal phase. The close packed phase is circled in red. The disordered phase is boxed in blue. Bromine atoms can be seen occupying pores (U_{Sample} = -0.93V; $I_{tunnelling}$ = 297A; 1014 Å x 1014 Å)

In summary, TBTANGO forms an ordered organometallic pore structure on silver at elevated temperatures. Pores appear to be constructed of 6 fully dehalogenated molecules linked by surface silver atoms. Dissociated bromine atoms appear to remain on the surface, trapped within the pore structures. This phase dominates, accounting for 4/5 of all deposited

regions of deposition. The remaining 1/5 of surface coverage was split between ordered and disordered close packed regions. The measured unit cell for the pore structure is 19.8 Å x 19.8 Å < 60.3°.

5.3 Au on Mica

5.3.1 Substrate Preparation

The gold films on mica are prepared in a separate high vacuum system (HVS). The HVS utilizes a mechanical roughing and diffusion pump combination. The cold trap of the diffusion pump is cooled by liquid nitrogen. The mica substrate is preheated to ~100°C for extended periods with 2A of current to desorb water which may have intercalated between the mica layers. An internal thermocouple monitors the temperature. Gold is deposited at 14 A for 2.5 minutes. The gold on mica samples are allowed to cool under a rough vacuum to ambient before being cut to size and flame annealed *ex-situ*.

After the gold layer is deposited, it is flame annealed in atmosphere to form large flat (111) terraces. Two approaches were used to flame anneal the sample. One of which was to use a torch with the flame above the surface, the other was to pass the sample through the flame of a Bunsen burner. There was not a standard speed or flame-sample separation distance when flame annealing gold samples. The author aimed for the tip of the flame – usually orange or red – to just breeze the sample. Without a standardized and measurable approach, the results were inconsistent.

For example, in the figure below two large area scans of bare gold on mica are shown. Although both of these surfaces were deemed of sufficient quality to deposit molecules, we can see a significant difference in the size of the resultant (111) terraces. Figure 5.31 a) has a small flat terrace at the peak of an annealed crystallite. To the left of the crystallite is a highly

stepped region. Although it is not easily visible, the right of the crystallite is a region which also contains several steps. In figure 5.31 b), we see multiple flat terraces which are 4 to 5 times as large as the leftward surface. The sample to the right is more ideal than the left.

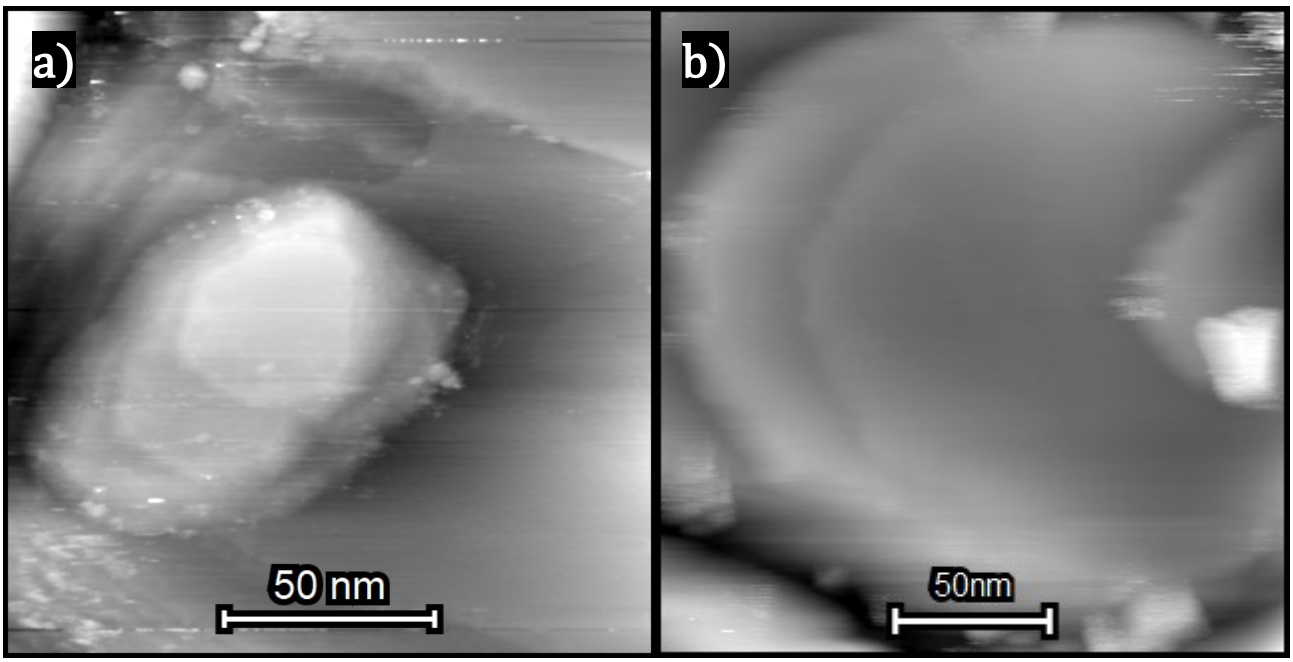

Fig. 5.31: A side by side of two Au(111) on mica surfaces imaged by STM. a) A sample which was flame annealed marginally. ($U_{bias} = +1.28$ V; $I_{tunnelling} = 486$ pA; 1529 Å x 1529 Å) b) A highly successful flame anneal. ($U_{bias} =$ V; $I_{tunnelling} =$ nA; 2010 Å x 2070 Å)

5.3.2 Elevated Temperature Deposition onto Au thin films

TBTANGO was deposited onto the flame-annealed gold surface after verification of a suitable surface with STM. The deposition was conducted with the gold film preheated to 180°C. The temperature was monitored by an internal thermocouple.

The deposition of TBTANGO onto the gold on mica samples revealed that TBTANGO self-assembles on Au(111). TBTANGO monomers arrange such that 3 bromine atoms (each from a different molecule) converge at a point. The SAMN is characterized by a one-molecule cell as shown in figure 5.32, the measurements of the cell are 10.5 Å x 10.5 Å $< 59.2°$. We observed multiple domains of the same phase oriented in various directions on the surface.

Within each domain, adjacent molecules have no relative rotation – that is they are all oriented in the same direction.

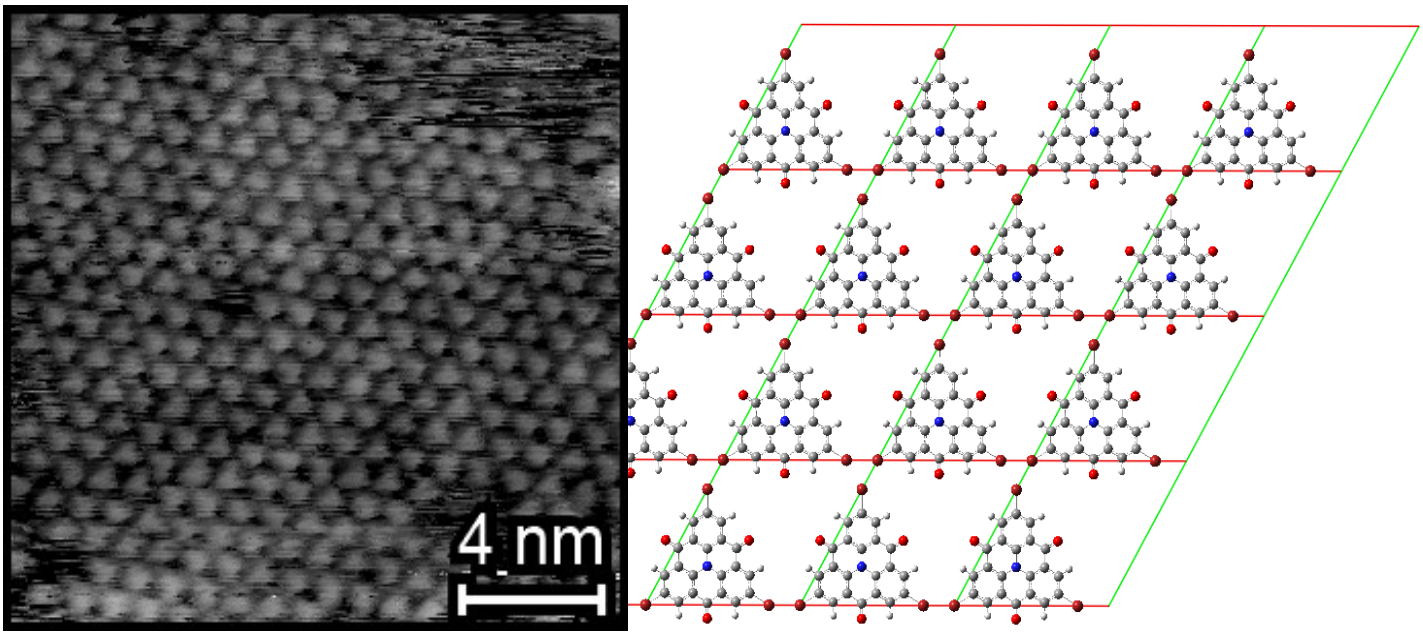

Fig. 5.32: Left: Self-assembled TBTANGO on the hot Au(111) surface whereby the monomers orient themselves in one direction (U_{Sample} = -1.02V V; $I_{tunnelling}$ = 347pA; 174 Å x 160 Å) Right: The proposed unit cell structure of the SA TBTANGO for a single domain: 10.5 Å x 10.5 Å < 59.2°

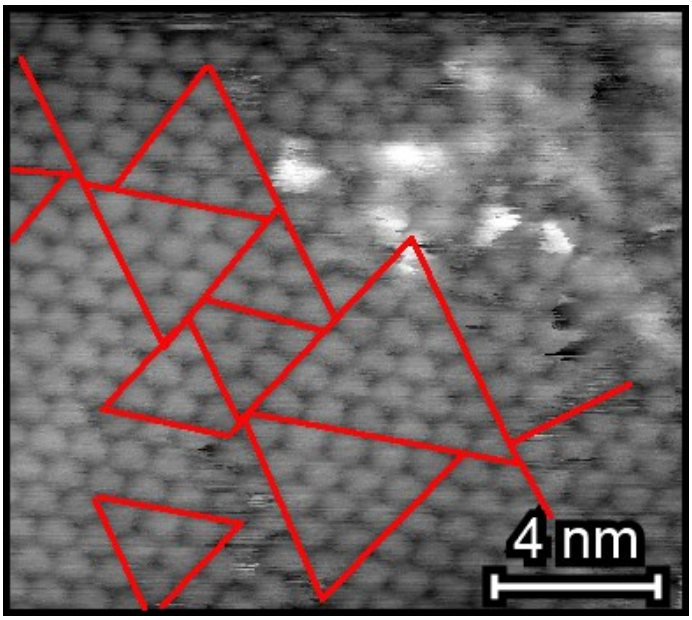

Fig. 5.33: An STM image of the SA TBTANGO layer which highlights the existence of multiple domains. Adjacent molecules within a domain do not have a relative rotation but the adjacent domains do have a relative rotation. (U_{Sample} = -1.01V; $I_{tunnelling}$ = 348pA; 164 Å x 145 Å)

The surface vectors for the self-assembled TBTANGO phase are of equal length and are separated by an angle of 59.2°. Measurements identify the length of the surface vectors as 10.5 Å, however STM drift could not be completely ruled out for these measurements. STM drift refers to real time thermal movement of the surface features as well as to hysteresis in the piezoelectric actuators of the scanning tunnelling microscope. The TBTANGO molecules appear to be intact after deposition because the herringbone reconstruction of gold persists after molecular deposition. Adsorbed surface bromine atoms are known to break the Au(111) reconstruction (Saywell et al., 2014; Pham et al., 2016). The existence of the herringbone reconstruction after deposition implies weak interactions between TBTANGO and the gold substrate (Pham et al., 2016; Galeotti et al., 2019).

The SA of TBTANGO on Au(111)/mica described above is unlike SA phases previously reported in the literature for a very similar tribromotrioxaazatriangulene molecule known as TBTANG. It was reported that TBTANG self-assembles in an alternating phase, whereby adjacent molecules possess a 180° relative rotation, when deposited on Au(111) at room temperature (De Marchi et al., 2019). The SAMN of intact TBTANG was determined with DFT calculations by De Marchi et al., (2019) to be stabilized by halogen-halogen interactions. Adjacent TBTANG molecules form clusters of 6 bromine atoms. Beyond the structure of the cell it was observed that the Au(111) herringbone reconstruction induced domain boundaries which resulted in a 60° rotation between TBTANG domains (figure 5.35). We believe the herringbone has a similar effect on the SA of TBTANGO. The many small domain boundaries observed in figure 5.33 may be induced by the herringbone reconstruction.

In this work, TBTANGO was dosed at a substrate temperature of ~180°C. Galeotti et al., (2020) report that substrate temperature is a pivotal parameter when dosing TBTANGO on

gold, as even a 30°C difference (between 180°C and 210°C) can give a significant difference in the quality of the ensuing overlayer. The 30°C temperature range is enough to distinguish between a highly organized polymer and a defective polymer containing halogenated TBTANGO molecules among the covalently linked molecules. The high Au(111) temperature dependence of TBTANGO may explain our unexpected result. A systematic study of the substrate temperature is required to further investigate the influence of substrate temperature and the resultant phase of TBTANGO.

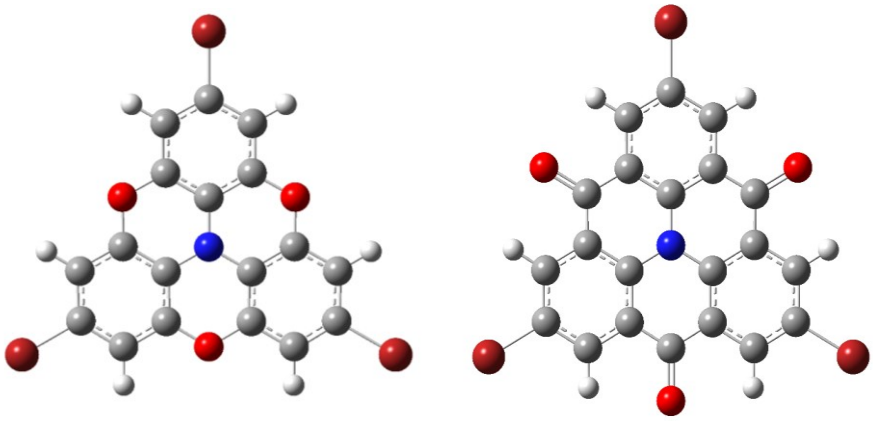

Fig. 5.34: Schematic images of TBTANG and TBTANGO. The only difference between TBTANGO and TBTANG is the substitution of carbonyl groups for oxygen bridges. Colour scheme: Grey - carbon, light grey – hydrogen, red – oxygen, maroon – bromine, blue – nitrogen.

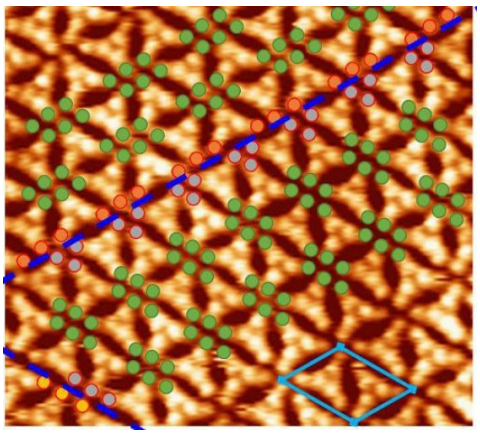

Fig. 5.35: The room temperature phase of TBTANG on Au(111) showing the domain boundaries due to the substrate herringbone reconstruction. Blue lines indicate domain boundaries. Green, red and yellow circles represent bromine atoms. The unit cell is highlighted in turquoise. ($U_{bias} = 0.39V$; $I_{tunnelling} = 160pA$; 100 Å x 100Å)

The SA of TBTANGO was further investigated through the use of density-functional theory (DFT) calculations. The Vienna Ab intio Simulation Package (VASP) was used by Dr. Ebrahimi in the Department of Chemistry, to calculate a relaxed one molecule unit cell with periodic boundary conditions (Kresse, & Hafner, 1993; Kresse, & Furthmüller, 1996a; 1996b). Figure 5.36 below shows the result yielding an optimized TBTANGO cell with dimensions: $s_1 =$ 13.3 Å, $s_2 =$ 13.3 Å, $\theta = 60^o$. The experimental cell was $s_1 =$ 10.5 Å, $s_2 =$ 10.5 Å, $\theta = 59.2^o$. The discrepancy is attributed to STM drift which could not be compensated for in the measurements of the unit cell.

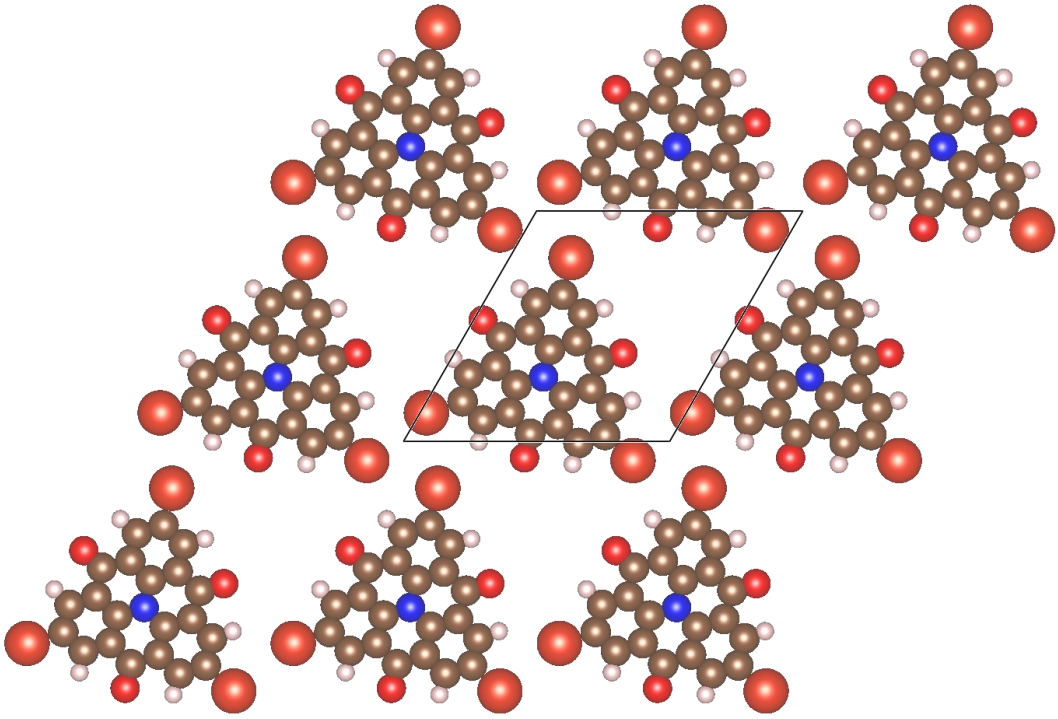

Fig. 5.36: VASP calculations reveal a stable self-assembled phase of TBTANGO in agreement with the experimentally observed structure. $s_1 =$ 13.3 Å, $s_2 =$ 13.3 Å, $\theta = 60^o$

Other DFT calculations were also performed to give insight into the periodic boundary condition calculations (VASP) and the observed structure. A single TBTANGO molecule was

optimized along with a pair of molecules and a three-molecule configuration using the usual functional and basis described in Chapter 4.4. The three-molecule configuration (figure 5.37 below) converged to a configuration similar to what is observed experimentally. This suggests Br-Br interactions are the stabilizing force when considering physical space limitations on the gold surface of the three-molecule configuration.

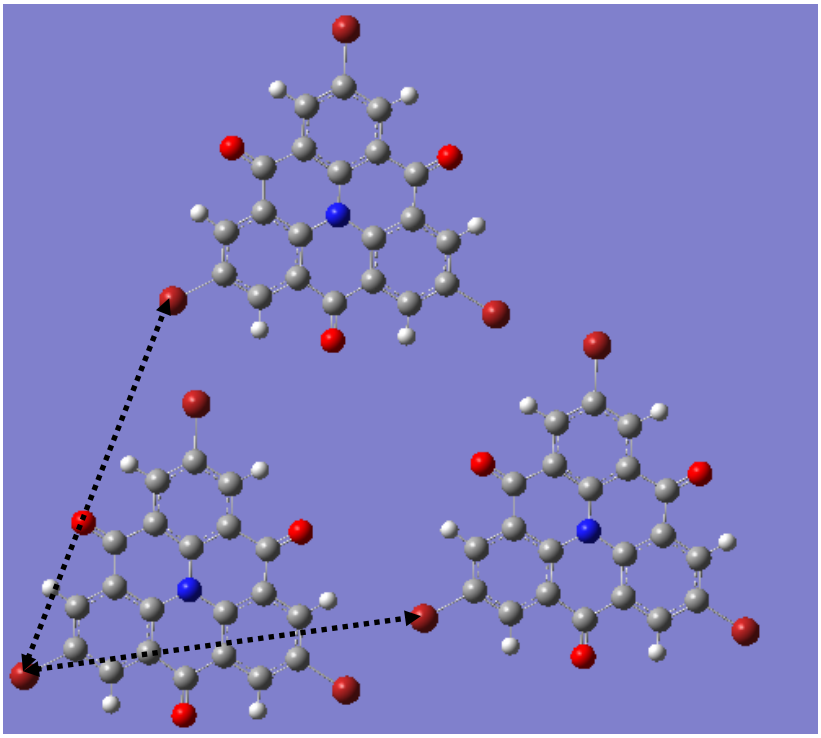

Fig. 5.37: The three TBTANGO molecules in free space optimized to a structure stabilized by halogen interactions which reflects the structure of the experimentally observed SAMN. The configuration minimized to an interaction energy of -3.47 kcal/mol per molecule. The bromine-bromine distances shown are both 13.3 Å in agreement with the VASP calculation.

Further DFT calculations were performed to understand the phase observed on Au(111). In these calculations, dimers were restricted to maintain the initial input configuration. Using the same functional and basis, the separation distance between molecules was adjusted and the minimum energy separation for a TBTANGO dimer was identified. The configuration minimized the distance between a bromine atom of each molecule. Molecules

were aligned diagonally; this alignment was motivated by the experimentally observed unit cell.

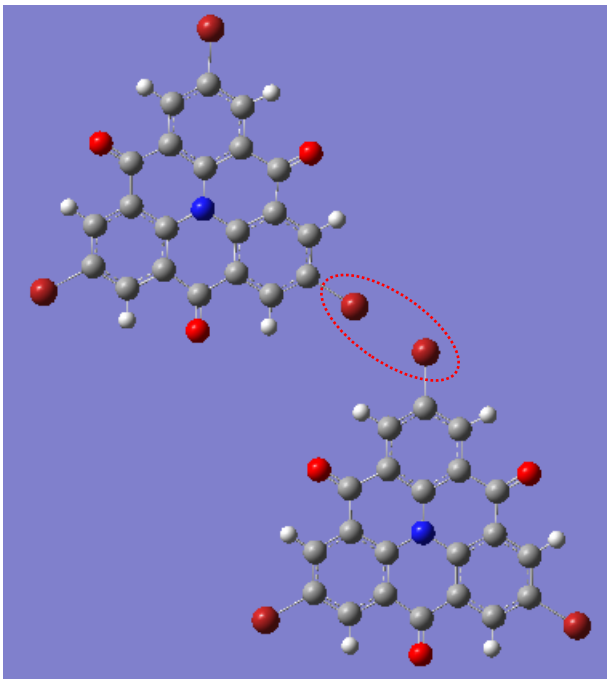

Fig. 5.38: Shown is a constrained dimer where only the distance shown in red was a free parameter. The configuration minimized to a separation distance of 3.5 Å with an interaction energy of -1.3 kcal/mol per molecule.

It is within reason to postulate that the increased opportunity for bromine-bromine interactions of a TBTANGO molecule within the 2-D network leads to a stable energy configuration on Au(111). Each TBTANGO molecule has the opportunity for 2 halogen-halogen interactions per bromine atom for a total of 6 halogen-halogen interactions. In the VASP calculated configuration, one molecule could thus have an interaction energy of -7.8 kcal/mol. The DFT VASP calculation on the unit cell of TBTANGO provides additional evidence for this conclusion.

In this subsection, it was established that the thin films of Au(111) terminated facets supported the SA of TBTANGO at elevated temperature (180°C). The phase observed was novel compared to similar work in the literature (De Marchi et al., 2019; Galeotti et al., 2020).

A unit cell was defined from ab initio calculations for the experimentally observed phase. The cell is delimited by $s_1 = 13.3$ Å, $s_2 = 13.3$ Å, $\theta = 60^o$. The discrepancy between the measured cell ($s_1 = 10.5$ Å, $s_2 = 10.5$ Å, $\theta = 59.2^o$) is attributed to STM drift.

6. Summary

Many studies have been conducted in which organic molecules are deposited on metal or semiconducting substrates in ultrahigh vacuum. The goal of this work was to study the self-assembly of the molecule, tribromotrioxoazatriangulene, (TBTANGO) on three surfaces – silicon doped boron, silver, and gold. The influence of the different substrates on the overlayer structure of TBTANGO was the focal point. We were motivated by the vast opportunity of self-assembled nanostructured materials to reduce costs and manufacturing time in both established and emerging industries.

Each of the substrates were investigated primarily with scanning tunnelling microscopy. Low-energy electron diffraction, Auger electron spectroscopy and density functional theory supplemented the scanning tunnelling microscopy. In brief, room-temperature STM experiments were conducted for the heterotriangulene derivative, TBTANGO, on three surfaces: Si(111)-$\sqrt{3}$x$\sqrt{3}$-R30°-B, Ag(111), and Au(111) on mica.

The silicon boron surface was not prepared to a suitable quality to support self-assembly. Preparation of the surface was met with a conundrum between the passivation of reactive dangling bonds necessary for self-assembly, and surface contamination. Many procedures were attempted which can be broadly categorized as annealing of purchased boron doped silicon wafers and the intercalation of boron via the deposition of boron trioxide. It was decided that flashing the purchased wafers near 1200^{o}C, followed by annealing for 100 minutes at 930^{o}C gave the best result. TBTANGO monomers deposited onto the Si(111)-$\sqrt{3}$x$\sqrt{3}$-R30^{o}-B surface were not mobile. STM imaging show molecules were decomposed by surface dangling bonds.

The investigation of TBTANGO on a Ag(111) surface gave interesting results. At room

temperature, short chains, dimer and monomer structures attributed to partial dehalogenation were observed. With the silver substrate heated to 240°C, three distinct phases occurred. Of these three phases, an organometallic honeycomb hexagonal structure was the most common. The honeycomb hexagonal structure was measured to have a unit cell of 19.8 Å × 19.8 Å < 60.3°. This cell is nearly commensurate with the substrate layer in a 7×7 reconstruction. It is in reasonable agreement with gas phase density functional calculations for the interatomic pore spacing (23 Å). Given the threefold symmetry of the overlayer, independent aggregates were not observed with relative rotations, indicative of only one unique TBTANGO domain and a definite epitaxial relationship to the threefold symmetry of the underlying (111) plane.

In total, the remaining two phases, disordered and organized close packed, were only observed for ~20% of the surface coverage. The organized close packed phase was often observed near atomic steps and appears to have surface vectors 9.1 Å long. Previous studies of halogenated organic molecules on coinage metals ascribe the smaller phase to an organometallic with three metal-carbon bonds per metal atom (Gutzler et al., 2009; Liu, 2019). Further study is required to uncover the essence of the organized close packed phase.

The deposition of TBTANGO on gold thin films results in a self-assembled structure. The self-assembled structure can be described by a one molecule unit cell delimited with $s_1 = 10.5$ Å, $s_2 = 10.5$ Å, $\theta = 59.2°$. In this phase, each molecule has the same orientation. This was in contrast to the self-assembled phase of the oxygen-bridged variant of TBTANGO on Au(111) (De Marchi et al., 2019). The variant showed a self-assembled structure where adjacent molecules had a “one-up, one-down” organization. The experimentally measured cell deviated from the theoretically calculated cell: $s_1 = 13.3$ Å, $s_2 = 13.3$ Å, $\theta = 60°$ which is ascribed to uncorrected STM drift. Insight gained from density functional theory calculations corroborated

experimental observations that halogen-halogen interactions were the stabilizing mechanism for the self-assembled phase.

In conclusion, the molecular deposition of TBTANGO resulted in an organometallic structure on silver, a self-assembled phase on gold and did not form a self-assembled phase on Si-$\sqrt{3}\times\sqrt{3}$-R30^{o}-B due to difficulty passivating the surface. Further work is required to answer remaining questions. For example, under what conditions can a high-quality silicon-boron surface be prepared? With further revisions, can the intercalation of B_2O_3, be an equally or more viable approach than heating the highly doped silicon wafers? Will the organometallic phase of TBTANGO on silver or gold transition to a 2-D polymer with additional annealing? At what substrate temperature does TBTANGO transition between SA phases on silver?

7. References

Adjizian, J. J., Briddon, P., Humbert, B., Duvail, J. L., Wagner, P., Adda, C., & Ewels, C. (2014). Dirac Cones in two-dimensional conjugated polymer networks. *Nature communications*, *5*, 5842.

Agarwala, P., & Kabra, D. (2017). A review on triphenylamine (TPA) based organic hole transport materials (HTMs) for dye sensitized solar cells (DSSCs) and perovskite solar cells (PSCs): evolution and molecular engineering. *Journal of Materials Chemistry A*, *5*(4), 1348-1373.

Andrade, D. P., Miwa, R. H., Drevniok, B., Drage, P., & McLean, A. B. (2015). Surface and near surface defects in δ-doped Si (1 1 1). *Journal of Physics: Condensed Matter*, *27*(12), 125001.

Avouris, P., Lyo, I. W., Bozso, F., & Kaxiras, E. (1990). Adsorption of boron on Si (111): Physics, chemistry, and atomic-scale electronic devices. *Journal of Vacuum Science & Technology A: Vacuum, Surfaces, and Films*, *8*(4), 3405-3411.

Ayrault, G., & Ehrlich, G. (1974). Surface self-diffusion on an fcc crystal: An atomic view. *The Journal of Chemical Physics*, *60*(1), 281-294.

Bardeen, J. (1961). Tunnelling from a many-particle point of view. *Physical Review Letters*, *6*(2), 57.

Baris, B., Jeannoutot, J., Luzet, V., Palmino, F., Rochefort, A., & Cherioux, F. (2012). Noncovalent bicomponent self-assemblies on a silicon surface. *ACS Nano*, *6*(8), 6905-6911.

Bartels, L. (2010). Tailoring molecular layers at metal surfaces. *Nature chemistry*, *2*(2), 87- 95.

Barth, J. V. (2007). Molecular architectonic on metal surfaces. *Annu. Rev. Phys. Chem.*, *58*,

375-407.

Barth, J. V., Costantini, G., & Kern, K. (2010). Engineering atomic and molecular nanostructures at surfaces. In *Nanoscience and technology: a collection of reviews from Nature journals* (pp. 67-75).

Baruah, S., & Dutta, J. (2009). Nanotechnology applications in pollution sensing and degradation in agriculture: a review. *Environmental Chemistry Letters*, *7*(3), 191-204.

Basagni, A., Sedona, F., Pignedoli, C. A., Cattelan, M., Nicolas, L., Casarin, M., & Sambi, M. (2015). Molecules–oligomers–nanowires–graphene nanoribbons: a bottom-up stepwise on-surface covalent synthesis preserving long-range order. *Journal of the American Chemical Society*, *137*(5), 1802-1808.

Baumgärtel, P., Paggel, J. J., Hasselblatt, M., Horn, K., Fernandez, V., Schaff, O., ... & Denlinger, J. (1999). Structure determination of the (3× 3) R 30° boron phase on the Si (111) surface using photoelectron diffraction. *Physical Review B*, *59*(20), 13014.

Becke, A. D. (1988). Density-functional exchange-energy approximation with correct asymptotic behavior. *Physical review A*, *38*(6), 3098.

Becke, A. D. (1993). A new mixing of Hartree–Fock and local density-functional theories. *The Journal of chemical physics*, *98*(2), 1372-1377.

Bedrossian, P., Meade, R. D., Mortensen, K., Chen, D. M., Golovchenko, J. A., & Vanderbilt, D. (1989). Surface doping and stabilization of Si (111) with boron. *Physical review letters*, *63*(12), 1257.

Bieri, M., Blankenburg, S., Kivala, M., Pignedoli, C. A., Ruffieux, P., Müllen, K., & Fasel, R. (2011). Surface-supported 2D heterotriangulene polymers. *Chemical communications*,

47(37), 10239-10241.

Björk, J. (2016). Reaction mechanisms for on-surface synthesis of covalent nanostructures. *Journal of Physics: Condensed Matter*, *28*(8), 083002.

Bonilla, R. S., Hoex, B., Hamer, P., & Wilshaw, P. R. (2017). Dielectric surface passivation for silicon solar cells: A review. *physica status solidi (a)*, *214*(7), 1700293.

Briggs, D., & Seah, M. P. (1983). *Practical surface analysis: by Auger and X-ray photoelectron spectroscopy*. Wiley.

Cai, L., Tsao, H. N., Zhang, W., Wang, L., Xue, Z., Grätzel, M., & Liu, B. (2013). Organic Sensitizers with Bridged Triphenylamine Donor Units for Efficient Dye-Sensitized Solar Cells. *Advanced Energy Materials*, *3*(2), 200-205.

Cao, R., Yang, X., & Pianetta, P. (1993). Characterization of the B/Si surface electronic structures. *Journal of Vacuum Science & Technology A: Vacuum, Surfaces, and Films*, *11*(4), 1817-1822.

Cardenas, L., Gutzler, R., Lipton-Duffin, J., Fu, C., Brusso, J. L., Dinca, L. E., ... & Perepichka, D. F. (2013). Synthesis and electronic structure of a two dimensional π-conjugated polythiophene. *Chemical Science*, *4*(8), 3263-3268.

Chambliss, D. D., & Wilson, R. J. (1991). Relaxed diffusion limited aggregation of Ag on Au (111) observed by scanning tunneling microscopy. *Journal of Vacuum Science & Technology B: Microelectronics and Nanometer Structures Processing, Measurement, and Phenomena*, *9*(2), 928-932.

Chambliss, D. D., Wilson, R. J., & Chiang, S. (1991). Ordered nucleation of Ni and Au islands on Au (111) studied by scanning tunneling microscopy. *Journal of Vacuum Science & Technology B: Microelectronics and Nanometer Structures Processing, Measurement,*

and Phenomena, *9*(2), 933-937.

Chen, C. J. (1990a). Origin of atomic resolution on metal surfaces in scanning tunneling microscopy. *Physical review letters*, *65*(4), 448.

Chen, C. J. (1990b). Tunneling matrix elements in three-dimensional space: The derivative rule and the sum rule. *Physical Review B*, *42*(14), 8841.

Chen, C. J. (1993). *Introduction to scanning tunneling microscopy* (Vol. 4). Oxford University Press on Demand.

Chung, K. H., Park, J., Kim, K. Y., Yoon, J. K., Kim, H., Han, S., & Kahng, S. J. (2011). Polymorphic porous supramolecular networks mediated by halogen bonds on Ag (111). *Chemical Communications*, *47*(41), 11492-11494.

Colson, J. W., & Dichtel, W. R. (2013). Rationally synthesized two-dimensional polymers. *Nature chemistry*, *5*(6), 453-465.

Copie, G., Makoudi, Y., Krzeminski, C., Cherioux, F., Palmino, F., Lamare, S., ... & Cleri, F. (2014). Atomic scale modeling of two-dimensional molecular self-assembly on a passivated Si surface. *The Journal of Physical Chemistry C*, *118*(24), 12817-12825.

Crabtree, R. H. (2009). *The organometallic chemistry of the transition metals*. John Wiley & Sons.

De Feyter, S., Miura, A., Yao, S., Chen, Z., Würthner, F., Jonkheijm, P., ... & De Schryver, F. C. (2005). Two-dimensional self-assembly into multicomponent hydrogen-bonded nanostructures. *Nano letters*, *5*(1), 77-81.

De Marchi, F., Galeotti, G., Simenas, M., Gallagher, M. C., Hamzehpoor, E., MacLean, O., ... & Tornau, E. E. (2019). Temperature-induced molecular reorganization on Au (111) driven by oligomeric defects. *Nanoscale*, *11*(41), 19468-19476.

Di Giovannantonio, M., El Garah, M., Lipton-Duffin, J., Meunier, V., Cardenas, L., Fagot Revurat, Y., ... & Contini, G. (2013). Insight into organometallic intermediate and its evolution to covalent bonding in surface-confined Ullmann polymerization. *ACS Nano*, *7*(9), 8190-8198.

Di Giovannantonio, M., Tomellini, M., Lipton-Duffin, J., Galeotti, G., Ebrahimi, M., Cossaro, A., ... & Fagot-Revurat, Y. (2016). Mechanistic picture and kinetic analysis of surface-confined Ullmann polymerization. *Journal of the American Chemical Society*, *138*(51), 16696-16702.

Di Giovannantonio, M., & Contini, G. (2018). Reversibility and intermediate steps as key tools for the growth of extended ordered polymers via on-surface synthesis. *Journal of Physics: Condensed Matter*, *30*(9), 093001.

Dishner, M. H., Hemminger, J. C., & Feher, F. J. (1997). Direct observation of substrate influence on chemisorption of methanethiol adsorbed from the gas phase onto the reconstructed Au (111) surface. *Langmuir*, *13*(8), 2318-2322.

Ditchfield, R. H. W. J., Hehre, W. J., & Pople, J. A. (1971). Self-consistent molecular-orbital methods. IX. An extended Gaussian-type basis for molecular-orbital studies of organic molecules. *The Journal of Chemical Physics*, *54*(2), 724-728.

Djurišić, A. B., Ng, A. M. C., & Chen, X. Y. (2010). ZnO nanostructures for optoelectronics: material properties and device applications. *Progress in quantum electronics*, *34*(4), 191-259.

Dmitriev, A., Spillmann, H., Lin, N., Barth, J. V., & Kern, K. (2003). Modular Assembly of Two-Dimensional Metal–Organic Coordination Networks at a Metal Surface. *Angewandte Chemie*, *115*(23), 2774-2777.,

Dong, L., Liu, P. N., & Lin, N. (2015). Surface-activated coupling reactions confined on a surface. *Accounts of chemical research*, *48*(10), 2765-2774.

Dong, L., Gao, Z. A., & Lin, N. (2016). Self-assembly of metal–organic coordination structures on surfaces. *Progress in Surface Science*, *91*(3), 101-135.

Eichhorn, J., Nieckarz, D., Ochs, O., Samanta, D., Schmittel, M., Szabelski, P. J., & Lackinger, M. (2014). On-surface Ullmann coupling: the influence of kinetic reaction parameters on the morphology and quality of covalent networks. *ACS Nano*, *8*(8), 7880-7889.

Eichhorn, J., Strunskus, T., Rastgoo-Lahrood, A., Samanta, D., Schmittel, M., & Lackinger, M. (2014). On-surface Ullmann polymerization via intermediate organometallic networks on Ag (111). *Chemical Communications*, *50*(57), 7680-7682.

El Garah, M., Lipton-Duffin, J., MacLeod, J. M., Gutzler, R., Palmino, F., Luzet, V., ... & Rosei, F. (2013). Self-Assembly of a Halogenated Molecule on Oxide-Passivated Cu (110). *Chemistry–An Asian Journal*, *8*(8), 1813-1817.

Eom, D., Moon, C. Y., & Koo, J. Y. (2015). Switching the charge state of individual surface atoms at Si (111)-$\sqrt{3}\times\sqrt{3}$: B surfaces. *Nano letters*, *15*(1), 398-402.

Fan, Q., Gottfried, J. M., & Zhu, J. (2015). Surface-catalyzed C–C covalent coupling strategies toward the synthesis of low-dimensional carbon-based nanostructures. *Accounts of chemical research*, *48*(8), 2484-2494.

Fan, Q., Zhu, J., & Gottfried, J. M. (2018). On-Surface Ullmann Reaction for the Synthesis of Polymers and Macrocycles. In *On-Surface Synthesis II* (pp. 83-112). Springer, Cham.

Fang, Z., Teo, T. L., Cai, L., Lai, Y. H., Samoc, A., & Samoc, M. (2009). Bridged triphenylamine-based dendrimers: tuning enhanced two-photon absorption performance with locked molecular planarity. *Organic letters*, *11*(1), 1-4.

Frisch, M. J., Trucks, G. W., Schlegel, H. B., Scuseria, G. E., Robb, M. A., Cheeseman, J. R., ... & Li, X. (2016). Gaussian 16. Revision B.01 [computer program]. *Gaussian, Inc.*,

Galeotti, G., Di Giovannantonio, M., Lipton-Duffin, J., Ebrahimi, M., Tebi, S., Verdini, A., ... & Contini, G. (2017). The role of halogens in on-surface Ullmann polymerization. *Faraday Discussions*, *204*, 453-469.

Galeotti, G., De Marchi, F., Taerum, T., Besteiro, L. V., El Garah, M., Lipton-Duffin, J., ... & Rosei, F. (2019). Surface-mediated assembly, polymerization and degradation of thiophene-based monomers. *Chemical science*, *10*(19), 5167-5175.

Galeotti, G., De Marchi, F., Hamzehpoor, E., MacLean, O., Rao, M. R., Chen, Y., ... & Sheverdyaeva, P. M. (2020). Synthesis of mesoscale ordered two-dimensional π-conjugated polymers with semiconducting properties. *Nature Materials*, 1-7.

Gao, H. Y., Wagner, H., Held, P. A., Du, S., Gao, H. J., Studer, A., & Fuchs, H. (2015). In-plane Van der Waals interactions of molecular self-assembly monolayer. *Applied Physics Letters*, *106*(8), 081606.

Gatti, R., MacLeod, J. M., Lipton-Duffin, J. A., Moiseev, A. G., Perepichka, D. F., & Rosei, F. (2014). Substrate, molecular structure, and solvent effects in 2D self-assembly via hydrogen and halogen bonding. *The Journal of Physical Chemistry C*, *118*(44), 25505-25516.

Green, J. E., Choi, J. W., Boukai, A., Bunimovich, Y., Johnston-Halperin, E., DeIonno, E., ... & Tseng, H. R. (2007). A 160-kilobit molecular electronic memory patterned at 10 11 bits per square centimetre. *Nature*, *445*(7126), 414-417.

Grill, L., Dyer, M., Lafferentz, L., Persson, M., Peters, M. V., & Hecht, S. (2007). Nano-architectures by covalent assembly of molecular building blocks. *Nature nanotechnology*, *2*(11), 687-691.

Gupta, A. K., & Leck, J. H. (1975). An evaluation of the titanium sublimation pump. *Vacuum*, *25*(8), 362-372.

Gutzler, R., Walch, H., Eder, G., Kloft, S., Heckl, W. M., & Lackinger, M. (2009). Surface mediated synthesis of 2D covalent organic frameworks: 1, 3, 5-tris (4-bromophenyl) benzene on graphite (001), Cu (111), and Ag (110). *Chemical communications*, (29), 4456-4458.

Gutzler, R., Ivasenko, O., Fu, C., Brusso, J. L., Rosei, F., & Perepichka, D. F. (2011). Halogen bonds as stabilizing interactions in a chiral self-assembled molecular monolayer. *Chemical Communications*, *47*(33), 9453-9455.

Gutzler, R., Cardenas, L., & Rosei, F. (2011). Kinetics and thermodynamics in surface-confined molecular self-assembly. *Chemical Science*, *2*(12), 2290-2300.

Gutzler, R., Fu, C., Dadvand, A., Hua, Y., MacLeod, J. M., Rosei, F., & Perepichka, D. F. (2012). Halogen bonds in 2D supramolecular self-assembly of organic semiconductors. *Nanoscale*, *4*(19), 5965-5971.

Gutzler, R., Cardenas, L., Lipton-Duffin, J., El Garah, M., Dinca, L. E., Szakacs, C. E., ... & Perepichka, D. F. (2014). Ullmann-type coupling of brominated tetrathienoanthracene on copper and silver. *Nanoscale*, *6*(5), 2660-2668.

Hariharan, P. C., & Pople, J. A. (1973). The influence of polarization functions on molecular orbital hydrogenation energies. *Theoretica chimica acta*, *28*(3), 213-222.

Hay, P. J., & Wadt, W. R. (1985). Ab initio effective core potentials for molecular calculations. Potentials for the transition metal atoms Sc to Hg. *The Journal of chemical physics*, *82*(1), 270-283.

Headrick, R. L., Robinson, I. K., Vlieg, E., & Feldman, L. C. (1989). Structure determination of the Si (111): B ($\sqrt{3}\times\sqrt{3}$) R30° surface: Subsurface substitutional doping. *Physical review*

letters, *63*(12), 1253.

Hedberg, C. L. (1995). Handbook of Auger Electron Spectroscopy, *Physical Electronics, Inc.,* Eden Prairie MN.

Hehre, W. J., Ditchfield, R., & Pople, J. A. (1972). Self—consistent molecular orbital methods. XII. Further extensions of Gaussian—type basis sets for use in molecular orbital studies of organic molecules. *The Journal of Chemical Physics*, *56*(5), 2257-2261.

Hughes, R. A., Menumerov, E., & Neretina, S. (2017). When lithography meets self-assembly: a review of recent advances in the directed assembly of complex metal nanostructures on planar and textured surfaces. *Nanotechnology*, *28*(28), 282002.

Hölzl, J., & Schulte, F. K. (1979). Work function of metals. In *Solid surface physics.* Springer, Berlin, Heidelberg.

Ibe, J. P., Bey Jr, P. P., Brandow, S. L., Brizzolara, R. A., Burnham, N. A., DiLella, D. P., ... & Colton, R. J. (1990). On the electrochemical etching of tips for scanning tunneling microscopy. *Journal of Vacuum Science & Technology A: Vacuum, Surfaces, and Films*, *8*(4), 3570-3575.

Ishihara, S., Labuta, J., Van Rossom, W., Ishikawa, D., Minami, K., Hill, J. P., & Ariga, K. (2014). Porphyrin-based sensor nanoarchitectonics in diverse physical detection modes. *Physical Chemistry Chemical Physics*, *16*(21), 9713-9746.

Jing, Y., & Heine, T. (2018). Two-dimensional kagome lattices made of hetero triangulenes are Dirac semimetals or single-band semiconductors. *Journal of the American Chemical Society*, *141*(2), 743-747.

Kamanina, N. V., Vasilyev, P. Y., Serov, S. V., Savinov, V. P., Bogdanov, K. Y., & Uskoković, D. (2010). Nanostructured materials for optoelectronic applications. *Acta Physica*

Polonica A, *117*(5), 786-790.

Kern, W. (1990). The evolution of silicon wafer cleaning technology. *Journal of the Electrochemical Society*, *137*(6), 1887.

Kittel, C., McEuen, P., & McEuen, P. (1996). *Introduction to Solid State Physics.* New York: Wiley.

Kittel, C. (2004). *Introduction to Solid State Physics*. Wiley.

Kresse, G., & Hafner, J. (1993). Ab initio molecular dynamics for liquid metals. *Physical Review B*, *47*(1), 558.

Kresse, G., & Furthmüller, J. (1996a). Efficient iterative schemes for ab initio total-energy calculations using a plane-wave basis set. *Physical review B*, *54*(16), 11169.

Kresse, G., & Furthmüller, J. (1996b). Efficiency of ab-initio total energy calculations for metals and semiconductors using a plane-wave basis set. *Computational materials science*, *6*(1), 15-50.

Kühnle, A. (2009). Self-assembly of organic molecules at metal surfaces. *Current Opinion in Colloid & Interface Science*, *14*(2), 157-168.

Lafferentz, L., Eberhardt, V., Dri, C., Africh, C., Comelli, G., Esch, F., ... & Grill, L. (2012). Controlling on-surface polymerization by hierarchical and substrate-directed growth. *Nature chemistry*, *4*(3), 215-220.

Lee, C., Yang, W., & Parr, R. G. (1988). Development of the Colle-Salvetti correlation-energy formula into a functional of the electron density. *Physical review B*, *37*(2), 785.

Li, H., Zhang, K., Pi, F., Guo, S., Shlyakhtenko, L., Chiu, W., ... & Guo, P. (2016). Controllable self-assembly of RNA tetrahedrons with precise shape and size for cancer targeting. *Advanced materials*, *28*(34), 7501-7507

Liao, L. Y., Zhang, X. M., Hu, F. Y., Wang, S., Xu, S. D., Zeng, Q. D., & Wang, C. (2014). Two-Dimensional Supramolecular Self-Assembly of Stilbene Derivatives with Ester Groups: Molecular Symmetry and Alkoxy Substitution Effect. *The Journal of Physical Chemistry C*, *118*(15), 7989-7995.

Lin, J. L., Petrovykh, D. Y., Viernow, J., Men, F. K., Seo, D. J., & Himpsel, F. J. (1998). Formation of regular step arrays on Si (111) 7× 7. *Journal of Applied Physics*, *84*(1), 255-260.

Lindner, S., Franz, M., Kubicki, M., Appelfeller, S., Dähne, M., & Eisele, H. (2019). Arrangement and electronic properties of cobalt phthalocyanine molecules on B-Si (111)-√3×√3 R30°. *Physical Review B*, *100*(24), 245301.

Liu, R. (2019). *Constructing two-dimensional molecular networks on metal and semiconducting surfaces: a scanning tunneling microscopy study*. [Doctoral Dissertation, Lakehead University] https://knowledgecommons.lakeheadu.ca/handle/2453/4473

Liu, R., Fu, C., Perepichka, D. F., & Gallagher, M. C. (2016). Supramolecular structures of halogenated oligothiophenes on the Si (111)-√ 3×√ 3-Ag surface. *Surface Science*, *647*, 51-54.

Lyo, I. W., Kaxiras, E., & Avouris, P. (1989). Adsorption of boron on Si (111): Its effect on surface electronic states and reconstruction. *Physical review letters*, *63*(12), 1261.

MacLeod, J. M., Ivasenko, O., Fu, C., Taerum, T., Rosei, F., & Perepichka, D. F. (2009). Supramolecular ordering in oligothiophene− fullerene monolayers. *Journal of the American Chemical Society*, *131*(46), 16844-16850.

Major, F. G., Gheorghe, V. N., Werth, G., & Werth, G. (2005). *Charged particle traps: physics and techniques of charged particle field confinement* (Vol. 37). Springer Science &

Business Media. pg. 17 - 21, 299-308

Makoudi, Y., Beyer, M., Jeannoutot, J., Picaud, F., Palmino, F., & Chérioux, F. (2014). Supramolecular self-assembly of brominated molecules on a silicon surface. *Chemical Communications*, *50*(43), 5714-5716.

Marie, C., Silly, F., Tortech, L., Mullen, K., & Fichou, D. (2010). Tuning the packing density of 2D supramolecular self-assemblies at the solid−liquid interface using variable temperature. *ACS Nano*, *4*(3), 1288-1292.

Mayne, A. J., Riedel, D., Comtet, G., & Dujardin, G. (2006). Atomic-scale studies of hydrogenated semiconductor surfaces. *Progress in surface science*, *81*(1), 1-51.

McCarty, G. S., & Weiss, P. S. (2004). Formation and manipulation of protopolymer chains. *Journal of the American Chemical Society*, *126*(51), 16772-16776.

Menzli, S., Hamada, B. B., Arbi, I., Souissi, A., Laribi, A., Akremi, A., & Chefi, C. (2016). Adsorption study of copper phthalocyanine on Si (111)($\sqrt{3}\times\sqrt{3}$) R30 Ag surface. *Applied Surface Science*, *369*, 43-49.

Metrangolo, P., Murray, J. S., Pilati, T., Politzer, P., Resnati, G., & Terraneo, G. (2011). The fluorine atom as a halogen bond donor, viz. a positive site. *CrystEngComm*, *13*(22), 6593-6596.

Mishra, P. K., & Ekielski, A. (2019). The self-assembly of lignin and its application in nanoparticle synthesis: A short review. *Nanomaterials*, *9*(2), 243.

Mondal, S. (2016). Recent advancement of Ullmann-type coupling reactions in the formation of C–C bond. *ChemTexts*, *2*(4), 17.

Mugele, F., Rettenberger, A., Boneberg, J., & Leiderer, P. (1998). The influence of tip–sample interaction on step fluctuations on Ag (111). *Surface science*, *400*(1-3), 80-86.

Naseri, N., Valizadeh, H., & Zakeri-Milani, P. (2015). Solid lipid nanoparticles and nanostructured lipid carriers: structure, preparation and application. *Advanced pharmaceutical bulletin*, *5*(3), 305.

Nie, S., Xing, Y., Kim, G. J., & Simons, J. W. (2007). Nanotechnology applications in cancer. *Annu. Rev. Biomed. Eng.*, *9*, 257-288. Nie, S., Xing, Y., Kim, G. J., & Simons, J. W. (2007). Nanotechnology applications in cancer. *Annu. Rev. Biomed. Eng.*, *9*, 257-288.

Nogami, J., Yoshikawa, S., Glueckstein, J. C., & Pianetta, P. (1994). Boron Reconstructed Si (111) Surfaces Produced by B2O3 Decomposition. *Scanning Microscopy*, *8*(4), 835-840.

Northrup, J. E. (1984). Si (111) 3× 3-Al: An Adatom-Induced Reconstruction. *Physical review letters*, *53*(7), 683.

O'Hanlon, J. F. (2005). *A user's guide to vacuum technology*. John Wiley & Sons.

Ohring, M. (2001). *Materials science of thin films*. Elsevier. Pg. 146

Ondrechen, M. J., Berkovitch-Yellin, Z., & Jortner, J. (1981). Model calculations of potential surfaces of van der Waals complexes containing large aromatic molecules. *Journal of the American Chemical Society*, *103*(22), 6586-6592.

Oura, K., Lifshits, V. G., Saranin, A. A., Zotov, A. V., & Katayama, M. (2003). *Surface science: an introduction*. Springer Science & Business Media.

Parthasarathi, R., & Subramanian, V. (2006). Characterization of hydrogen bonding: From van der Waals interactions to covalency. In *Hydrogen Bonding—New Insights* (pp. 1-50). Springer, Dordrecht.

Philp, D., & Stoddart, J. F. (1996). Self-assembly in natural and unnatural systems. *Angewandte Chemie International Edition in English*, *35*(11), 1154-1196.

Politzer, P., Murray, J. S., & Clark, T. (2010). Halogen bonding: an electrostatically-driven highly directional noncovalent interaction. *Physical Chemistry Chemical Physics*, *12*(28), 7748-7757.

Priimagi, A., Cavallo, G., Metrangolo, P., & Resnati, G. (2013). The halogen bond in the design of functional supramolecular materials: recent advances. *Accounts of chemical research*, *46*(11), 2686-2695.

Rajendran, R., Shrestha, L. K., Kumar, R. M., Jayavel, R., Hill, J. P., & Ariga, K. (2015). Composite nanoarchitectonics for ternary systems of reduced graphene oxide/carbon nanotubes/nickel oxide with enhanced electrochemical capacitor performance. *Journal of Inorganic and Organometallic Polymers and Materials*, *25*(2), 267-274.

Rassolov, V. A., Pople, J. A., Ratner, M. A., & Windus, T. L. (1998). 6-31G* basis set for atoms K through Zn. *The Journal of chemical physics*, *109*(4), 1223-1229.

Reithmaier, J., Petkov, P., Kulisch, W., & Popov, C. (Eds.). (2009). *Nanostructured materials for advanced technological applications*. Springer Science & Business Media.

Röder, H., Hahn, E., Brune, H., Bucher, J. P. & Kern, K. Building one-dimensional and two dimensional nanostructures by diffusion-controlled aggregation at surfaces. Nature 366, 141–143 (1993).

Saywell, A., Greń, W., Franc, G., Gourdon, A., Bouju, X., & Grill, L. (2014). Manipulating the conformation of single organometallic chains on Au (111). *The Journal of Physical Chemistry C*, *118*(3), 1719-1728.

Shi, K. J., Yuan, D. W., Wang, C. X., Shu, C. H., Li, D. Y., Shi, Z. L., ... & Liu, P. N. (2016). Ullmann reaction of aryl chlorides on various surfaces and the application in stepwise growth of

2D covalent organic frameworks. *Organic letters*, *18*(6), 1282-1285.

Spadafora, E. J., Berger, J., Mutombo, P., Telychko, M., Svec, M., Majzik, Z., ... & Jelínek, P. (2014). Identification of Surface Defects and Subsurface Dopants in a Delta-Doped System Using Simultaneous nc-AFM/STM and DFT. *The Journal of Physical Chemistry C*, *118*(29), 15744-15753.

Stanford Research Systems. Select the Best Bayard-Alpert Ionization Gauge for Your Application. Accessed 2020-08-1, Retrieved from: https://www.thinksrs.com/downloads/pdfs/applicationnotes/IG1selectapp.pdf

Steiner, C., Gebhardt, J., Ammon, M., Yang, Z., Heidenreich, A., Hammer, N., ... & Maier, S. (2017). Hierarchical on-surface synthesis and electronic structure of carbonyl-functionalized one-and two-dimensional covalent nanoarchitectures. *Nature communications*, *8*(1), 1-11.

Stroscio, J. A., & Kaiser, W. J. (1993). *Scanning tunneling microscopy* (Vol. 27). Academic press

Sundaravel, B., Das, A. K., Ghose, S. K., Sekar, K., & Dev, B. N. (1999). Epitaxial growth of silver on Br-passivated Si (111) substrates under high vacuum. *Applied surface science*, *137*(1-4), 11-19.

Suzuki, T., Lutz, T., Payer, D., Lin, N., Tait, S. L., Costantini, G., & Kern, K. (2009). Substrate effect on supramolecular self-assembly: from semiconductors to metals. *Physical Chemistry Chemical Physics*, *11*(30), 6498-6504.

Tan, A., & Zhang, P. (2019). Tailoring the growth and electronic structures of organic molecular thin films. *Journal of Physics: Condensed Matter*, *31*(50), 503001.

Tersoff, J., & Hamann, D. R. (1985). Theory of the scanning tunneling microscope. *Physical*

Review B, *31*(2), 805.

Theobald, J. A., Oxtoby, N. S., Phillips, M. A., Champness, N. R., & Beton, P. H. (2003). Controlling molecular deposition and layer structure with supramolecular surface assemblies. *Nature*, *424*(6952), 1029-1031.

Thomas, S., Li, H., Zhong, C., Matsumoto, M., Dichtel, W. R., & Bredas, J. L. (2019). Electronic structure of two-dimensional π-conjugated covalent organic frameworks. *Chemistry of Materials*, *31*(9), 3051-3065.

Van Hove, M. A., Weinberg, W. H., & Chan, C. M. (2012). *Low-energy electron diffraction: experiment, theory and surface structure determination* (Vol. 6). Springer Science & Business Media.

Voigtländer, B. (2015). *Scanning probe microscopy: Atomic force microscopy and scanning tunneling microscopy*. Springer.

Wagner, S. R., & Zhang, P. (2014). Nucleation and evolution of zinc phthalocyanine thin films on the deactivated Si (111)-B 3× 3 R30° surface. *Surface science*, *630*, 22-27.

Walch, H., Gutzler, R., Sirtl, T., Eder, G., & Lackinger, M. (2010). Material-and orientation-dependent reactivity for heterogeneously catalyzed carbon—bromine bond homolysis. *The Journal of Physical Chemistry C*, *114*(29), 12604-12609.

Wang, W.H., Shi, X.Q., Wang, S.Y., Van Hove, M.A., Lin, N.: Single-molecule resolution of an organometallic intermediate in a surface-supported Ullmann coupling reaction. J. Am. Chem. Soc. 133, 13264–13267 (2011)

Weckesser, J., Barth, J. V., & Kern, K. (1999). Direct observation of surface diffusion of large organic molecules at metal surfaces: PVBA on Pd (110). *The Journal of chemical physics*, *110*(11), 5351-5354.

Whitesides, G. M., Mathias, J. P., & Seto, C. T. (1991). Molecular self-assembly and nanochemistry: a chemical strategy for the synthesis of nanostructures. *Science*, *254*(5036), 1312-1319.

Woodruff, D. P. & Delchar, T. A., (1994). *Modern Techniques of Surface Science*. (Cambridge Solid State Science Series). Cambridge: Cambridge University Press.

Xi, M., & Bent, B. E. (1993). Mechanisms of the Ullmann coupling reaction in adsorbed monolayers. *Journal of the American Chemical Society*, *115*(16), 7426-7433.

Yang, Y., Weaver, M. N., & Merz Jr, K. M. (2009). Assessment of the "6-31+ G**+ LANL2DZ" mixed basis set coupled with density functional theory methods and the effective core potential: prediction of heats of formation and ionization potentials for first-row-transition-metal complexes. *The Journal of Physical Chemistry A*, *113*(36), 9843-9851.

Yates, J. T. Jr (1991). Surface chemistry of silicon-the behaviour of dangling bonds. *Journal of Physics: Condensed Matter*, *3*(S), S143.

Yokoyama, T., Yokoyama, S., Kamikado, T., & Mashiko, S. (2001a). Nonplanar adsorption and orientational ordering of porphyrin molecules on Au (111). *The Journal of Chemical Physics*, *115*(8), 3814-3818.

Yokoyama, T., Yokoyama, S., Kamikado, T., Okuno, Y., & Mashiko, S. (2001b). Selective assembly on a surface of supramolecular aggregates with controlled size and shape. *Nature*, *413*(6856), 619-621.

Zangwill, A. (1988). *Physics at surfaces*. Cambridge: Cambridge University Press.

Zhang, W., Wang, T., Han, D., Huang, J., Feng, L., Ding, H., ... & Zhu, J. (2020). Stepwise Synthesis of N-Ag-N and C-Ag-C Organometallic Structures on a Ag (111) Surface.

The Journal of Physical Chemistry C.

Zhong, G., & Li, J. (2019). Muscovite mica as a universal platform for flexible electronics. *Journal of Materiomics*.

Zhong, L. S., Hu, J. S., Liang, H. P., Cao, A. M., Song, W. G., & Wan, L. J. (2006). Self-Assembled 3D flowerlike iron oxide nanostructures and their application in water treatment. *Advanced Materials*, *18*(18), 2426-2431.